

AD-751 548

EFFECT OF SPECIMEN SIZE ON CONFINED  
COMPRESSION TESTING OF ROCK CORES

Peter Jay Huck

IIT Research Institute

Prepared for:

Advanced Research Projects Agency

August 1972

DISTRIBUTED BY:

**NTIS**

National Technical Information Service  
U. S. DEPARTMENT OF COMMERCE  
5285 Port Royal Road, Springfield Va. 22151

AD751548

IIT RESEARCH INSTITUTE  
Technology Center  
Chicago, Illinois 60616

IITRI Project No. D6059  
Final Technical Report

EFFECT OF SPECIMEN SIZE ON CONFINED  
COMPRESSION TESTING OF ROCK CORES

by

Peter Jay Huck

Monitored by

Bureau of Mines  
U. S. Department of the Interior  
Twin Cities, Minnesota

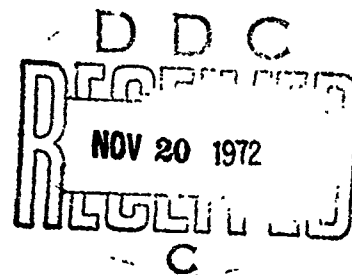
Sponsored by

Advanced Research Projects Agency  
Washington, D. C.

August, 1972

The views and conclusions contained in this document are those of the author and should not be interpreted as necessarily representing the official policies, either expressed or implied of the Advanced Research Projects Agency, Bureau of Mines, or the U. S. Government.

NATIONAL TECHNICAL  
INFORMATION SERVICE



Unclassified

3200.6 (Att 1 to Encl 1)

Mar 7, 66

Security Classification		
DOCUMENT CONTROL DATA - R & D		
(Security classification of title, body of abstract and indexing annotation must be entered when the overall report is classified)		
1. ORIGINATING ACTIVITY (Corporate author)		2a. REPORT SECURITY CLASSIFICATION
IIT Research Institute, Chicago, Ill.		Unclassified
		2b. GROUP
3. REPORT TITLE		
Effect of Specimen Size on Confined Compression Testing of Rock Cores		
4. DESCRIPTIVE NOTES (Type of report and inclusive dates)		
Final Technical Report		
5. AUTHOR(S) (First name, middle initial, last name)		
Peter J. Huck		
6. REPORT DATE	7a. TOTAL NO. OF PAGES	7b. NO. OF REFS
April 1972	175 177	33
8a. CONTRACT OR GRANT NO	9a. ORIGINATOR'S REPORT NUMBER(S)	
H0210009		
b. PROJECT NO		
ARPA Order No. 1579		
c. Amendment 2	9b. OTHER REPORT NO(S) (Any other numbers that may be assigned this report)	
d. Program Code 1F10		
10. DISTRIBUTION STATEMENT		
Approved for public release, distribution unlimited		
11. SUPPLEMENTAL NOTES		12. SPONSORING MILITARY ACTIVITY
		Director, Advanced Research Projects Agency
13. ABSTRACT		
<p>An experimental study was conducted to determine the influence of specimen size on the mechanical response of rock. Specimens of Charcoal Black granite (Cold Spring, Minnesota) and Indiana Limestone (Bedford, Indiana) ranging in size from 2-in. dia. to 36-in. dia. (32-in. dia. for the granite) were tested in triaxial compression. Test data included axial and circumferential strain at up to 30 locations on the largest specimens, and axial and radial stresses. Data for loading, unloading and reloading conditions were collected. The loading data were fit to models describing bulk modulus and shear modulus, from which other moduli were determined. The reduction in strength over the size range and confining pressures employed ranged from 20 to 50 percent.</p>		

DD FORM 1 NOV 65 1473

Unclassified

Security Classification

(6)

Unclassified

Security Classification

3200.8 (Att 1 to Encl 1)  
Mar 7, 66

14	KEY WORDS	LINK A		LINK B		LINK C	
		ROLE	WT	ROLE	WT	ROLE	WT
	Large Triaxial Tests Scale Effect Charcoal Black Granite Indiana Limestone						

Unclassified

Security Classification

(B)

EFFECT OF SPECIMEN SIZE ON CONFINED  
COMPRESSION TESTING OF LARGE ROCK CORES

by

Peter Jay Huck

IIT Research Institute  
Technology Center  
Chicago, Illinois 60616

ARPA Order Number	1579
Program Code Number	1F10
Name of Contractor	IIT Research Institute
Effective Date of Contract	29 Dec 1970
Contract Expiration Date	29 Jan 1972
Amount of Contract	\$75,791
Contract Number	H0210009
Principal Investigator and Phone Number	Madan M. Singh 312/225-9630 Ext. 4784
Project Engineer and Phone Number	Peter J. Huck 312/225-9630 Ext. 4735
Short Title of Work	Triaxial Tests on Large Rock Cores

Sponsored by  
Advanced Research Projects Agency  
ARPA Order No. 1579

The views and conclusions contained in this document are those of the author and should not be interpreted as necessarily representing the official policies, either expressed or implied, of the Advanced Research Projects Agency or the U. S. Government.

"Approved for public release; distribution unlimited"

IIT RESEARCH INSTITUTE  
(c)

## FOREWARD

This is the final report on IIT Research Institute (IITRI) Project No. D6059, entitled, "Effect of Specimen size on Confined Compression Testing of Rock Cores" covering the work period 29 December 1970 to 29 December 1971. This program was performed under Contract No. H0210009 with the Bureau of Mines of the U. S. Department of the Interior, with Mr. Egons R. Podnieks and later Dr. Syd Peng of the Twin Cities Mining Research Center acting as technical monitors. The program was sponsored by the Advanced Research Projects Agency of the U. S. Department of Defense under ARPA order no. 1579, Amendment 2.


The project was conducted under the direct supervision of Dr. Madan M. Singh, who served as program manager. Mr. Peter J. Huck was project engineer. Other IITRI staff members contributing to the overall research effort included Drs. R. H. Cornish and A. Semmelink, and Messrs. L. A. Finlayson, P. A. Hettich, E. J. Smith, J. Vosatka and A. Wawryszyn.

Respectfully submitted,

IIT RESEARCH INSTITUTE

  
Madan M. Singh, Manager  
Soil and Rock Mechanics

APPROVED:

  
R. H. Cornish  
Director of Research  
Mechanics of Materials Division

MMS/ps

IIT RESEARCH INSTITUTE

## TABLE OF CONTENTS

<u>Section</u>		<u>Page</u>
1	INTRODUCTION	2
2	PREVIOUS STUDIES	3
	2.1 Effect of Size	3
	2.2 Effect of Confinement	6
3	EXPERIMENTAL APPARATUS	7
	3.1 Small Test Cells	9
	3.2 48-Inch Test Cell	9
	3.3 Specimen Preparation	13
	3.4 Instrumentation and Data Reduction	14
4	EXPERIMENTAL PROGRAM	17
	4.1 Non-Destructive Tests	17
	4.1.1 Results of Non-Destructive Tests Charcoal Black Granite	20
	4.1.2 Results of Non-Destructive Tests Indiana Limestone	27
	4.2 Classification Tests	32
	4.2.1 Petrographic Analyses	35
	4.2.2 Tensile and Compressive Tests	37
	4.3 Description of Constitutive Equations	37
	4.4 Triaxial Compression	40
	4.5 Poisson's Ratio and Young's Modulus	43
	4.6 Charcoal Black Granite	44
	4.6.1 Hydrostatic Behavior	44
	4.6.2 Triaxial Behavior	47
	4.6.3 Young's Modulus and Poisson's Ratio	55
	4.7 Indiana Limestone	58
	4.7.1 Hydrostatic Behavior	58
	4.7.2 Triaxial Behavior	58
	4.7.3 Young's Modulus and Poisson's Ratio	60

## TABLE OF CONTENTS (Cont'd.)

<u>Section</u>	<u>Page</u>
4.8 Strength Properties	64
4.8.1 Charcoal Black Granite	64
4.8.2 Indiana Limestone	72
5 CONCLUSIONS	74
5.1 Hydrostatic Behavior	74
5.2 Triaxial Behavior	74
5.3 Effect of Specimen Size on Strength	75
5.4 Effect of Scale on Type of Failure	77
5.5 Recommendations	77
REFERENCES	78



## ILLUSTRATIONS

<u>Figure</u>		<u>Page</u>
1	Typical Triaxial Cell Schematic	8
2	Schematic of System for 2 in., 4in., and 12 in. Triaxial Specimens	10
3	Schematic of 48 in. I. D. Triaxial Cell Layout	11
4A	32 in. Granite Specimen Being Loaded into Large Triaxial Chamber	12
4B	32 in. Granite Specimen after Testing at Confining Pressure of 2000 psi	12
	Specimen Orientation and Array of Measurement Locations	15
6a	Acoustic Velocity System for Small Cores	18
6b	Acoustic Velocity System for Large Cores	18
7	Time of Arrival Measurements for a Single Specimen at Several Frequencies	20
8	Frequency of Occurrence of Shore Scleroscope Readings for Charcoal Black Granite	22
9	Frequency of Occurrence of Schmidt Hammer Readings for Charcoal Black Granite	23
10	Frequency of Occurrence of Sonic Velocity Determinations in Charcoal Black Granite	25
11	Shore Scleroscope Readings for Indiana Limestone	29
12	Frequency of Occurrence of Schmidt Hammer Readings for Indiana Limestone	30
13	Sonic Velocities for Indiana Limestone	31
14	Acoustic Velocities in 36 in. Dia Indiana Limestone	33
15	Idealized Hydrostatic Behavior of Granular Materials	39
16	Variation of Shear Modulus with Mean Stress	42
17	Mean Stress vs. Volumetric Strain (2" Granite)	45
18	Mean Stress vs. Volumetric Strain (4" Granite)	45
19	Mean Stress vs. Volumetric Strain (12" Granite)	46
20	Mean Stress vs. Volumetric Strain (32" Granite)	46
21	Bulk Modulus for 2" Granite	48
22	Bulk Modulus for 4" Granite	48

# ILLUSTRATIONS (Cont'd)

<u>Figure</u>		<u>Page</u>
23	Bulk Modulus for 12" Granite	49
24	Bulk Modulus for 32" Granite	49
25	Mean Stress vs. Volumetric Strain - Granite Models	50
26	Bulk Modulus vs. Mean Stress - Granite Models	50
27	Shear Modulus vs. Mean Stress - 2 in. Granite	51
28	Shear Modulus vs. Mean Stress - 4 in. Granite	51
29	Shear Modulus vs. Mean Stress - 12 in. Granite	52
30	Shear Modulus vs. Mean Stress - 32 in. Granite	52
31	Elastic Modulus for 2" Granite	54
32	Elastic Modulus for 4" Granite	54
33	Elastic Modulus vs. Mean Stress - 12" Granite	55
34	Elastic Modulus vs. Mean Stress - 32" Granite	55
35	Poisson's Ratio for 2 in. Granite	56
36	Poisson's Ratio for 4 in. Granite	56
37	Poisson's Ratio for 12" $\phi$ Granite	57
38	Poisson's Ratio for 32" $\phi$ Granite	57
39	Mean Stress vs. Volumetric Strain for all Limestone	59
40	Bulk Modulus for All Limestone	59
41	Shear Stress vs. Shear Strain for Limestone	61
42	Shear Modulus vs. Shear Strain for All Limestone	62
43	Shear Modulus vs. Shear Stress for All Limestone	63
44	Elastic Modulus Models for Indiana Limestone	65
45	Elastic Modulus for Indiana Limestone ( $\sigma_3 = 2$ ksi)	65
46	Elastic Modulus for Indiana Limestone ( $\sigma_3 = 4$ ksi)	66
47	Elastic Modulus for Indiana Limestone ( $\sigma_3 = 6$ ksi)	66
48	Elastic Modulus for Limestone ( $\sigma_3 = 8$ ksi)	67
49	Elastic Modulus for Limestone ( $\sigma_3 = 10$ ksi)	67

## ILLUSTRATIONS (Cont'd)

<u>Figure</u>		<u>Page</u>
50	Poisson's Ratio Models for Indiana Limestone	68
51	Poisson's Ratio for Indiana Limestone ( $\sigma_3 = 2$ ksi)	68
52	Poisson's Ratio for Indiana Limestone ( $\sigma_3 = 4$ ksi)	68
53	Poisson's Ratio for Indiana Limestone ( $\sigma_3 = 6$ ksi)	69
54	Poisson's Ratio for Indiana Limestone ( $\sigma_3 = 8$ ksi)	69
55	Poisson's Ratio for Indiana Limestone ( $\sigma_3 = 10$ ksi)	69
56A	Failure Stresses for Charcoal Black Granite	70
56B	Failure Stress for Indiana Limestone	70

## ABSTRACT

An experimental study was conducted to determine the influence of specimen size on the mechanical response of rock. Specimens of Charcoal Black granite (Cold Spring, Minnesota) and Indiana Limestone (Bedford, Indiana) ranging in size from 2-in. dia. to 36-in. dia. (32-in. dia. for the granite) were tested in triaxial compression. Test data included axial and circumferential strain at up to 30 locations on the largest specimens, and axial and radial stresses. Data for loading, unloading and reloading conditions were collected. The loading data were fit to models describing bulk modulus and shear modulus, from which other moduli were determined. The reduction in strength over the size range and confining pressures employed ranged from 20 to 50 percent.

## 1.0 INTRODUCTION

One of the problem areas in mining and underground construction is that little is known about the mass behavior of rock. It is recognized that the rock mass behaves differently from small specimens that can be tested in the laboratory, but the effect of scale is not well understood, particularly under generalized stress conditions. Since large scale tests are difficult and expensive even when they are possible, investigation into the influence of specimen size will help to establish a relationship between the behavior of small specimens in routine laboratory tests and the mass behavior of rock in the field. This program was intended to study the scale effect in triaxial tests over a range of specimen sizes.

Two rock types, Charcoal Black Granite (Cold Spring, Minnesota) and Indiana limestone (Bedford, Indiana) were studied during this program. A previous program<sup>1\*</sup> considered the granite, as well as another rock type, so that additional data on large granite specimens was available. Four sizes of specimens, 2-in. dia, 4-in. dia, 12-in. dia, and 32-in. dia (36-in. dia. for the limestone) were tested in triaxial compression. All triaxial specimens were strain gaged to allow the determination of elastic moduli. The strain data were fit to models representing hydrostatic and triaxial behavior to identify any change in mechanical properties with size. The failure data were correlated to quantify the reduction in strength with increasing size.

---

\*Superscripts indicate references listed at the end of the report

## 2.0 PREVIOUS STUDIES

### 2.1 Effect of Size

A number of investigators have studied the strength of pillars and coal cubes as a function of size. Their results are usually expressed as a power function in one of the following or similar forms:

$$\sigma_c \propto V^a R^b \quad (1)$$

$$\sigma_c \propto a^\beta \quad (2)$$

$$\sigma_c \propto b^\alpha h^\beta \quad (3)$$

in which

$\sigma_c$  = failure stress

V = volume

R = the pillar width-height ratio

a = cube dimension

b, h = pillar width and height respectively.

Salaman and Munro<sup>2</sup> summarized reported values for the exponents a, b,  $\alpha$  and  $\beta$  in formulas of the form of eq. (1) and (3) by making use of the relationships between ( $\alpha$ ,  $\beta$ ) and (a, b) implied by the dimensional terms V, R, b and h. This summary is given as:

	$\alpha$	$\beta$	a	b
Salaman and Munro <sup>2</sup>	-0.66 $\pm 0.16$	0.46 $\pm 0.14$	-0.067 $\pm 0.048$	0.59 $\pm 0.14$
Greenwald et al <sup>3</sup>	-0.183	0.50	-0.111	0.72
Steart <sup>4</sup> Holland and Gaddy	-1.00	0.50	-0.167	0.83

Salaman and Munro<sup>1</sup> observe that the variation in the exponents may be a function of specimen size, and that there may exist a critical size above which the effect of increasing volume is negligible.

Investigators concerned with cube strength have typically found values of  $\beta$  in Eq. (2) on the order of -0.5.

For rocks, the types of relationships developed are slightly different. According to the Weibull theory<sup>5</sup>,

$$\left(\frac{\sigma}{\sigma_m}\right)^\alpha = \left(\frac{v_m}{v}\right)$$

where  $\sigma$  = tensile or compressive strength of the rock from a standard laboratory test,

$\sigma_m$  = equivalent strength of the rock mass,

$v_m$  = volume of the rock mass,

$v$  = volume of the test sample, and

$\alpha$  = constant (with values near 10 for rocks).

The relation established by Protodyakonov<sup>6</sup> was of the type

$$\frac{\sigma}{\sigma_m} = 1 + \frac{s(\gamma - 1)}{s + a}$$

where  $s$  = spacing between major discontinuities in the rock mass, e.g., joints, beds.

$a$  = dimension of the test specimen, usually diameter for compression tests, and

$\gamma$  = mass fract coefficient (in compression: 1-2 for igneous rocks, 1-3 for competent sedimentary rocks, 3-10 for weak rocks; in tension: approximately double these values).

Grobbelaar<sup>7</sup> based on the work of Epstein<sup>8</sup>, Bieniawski<sup>9</sup>, and others found that the formulae relating the modal strength of

the weakest elements and its standard deviation, based on the weakest link theory, are:

$$\sigma_N = \sigma_u - \sigma_s (21\log N)^{0.5 - 1/2} \log(\log N) + \log(4) (21\log N)^{-0.5}$$

$$\text{and } \sigma_s(N) = \sigma_s \times \pi (121\log N)^{-0.5}$$

$$\text{or } \sigma_s(N) = \sigma_s(N_0) (\log N_0 / \log N)^{0.5}$$

Where  $N$  = number of flaws in the large cubic specimen,

$N_0$  = number of flaws in the small cubic specimen or unit cube,

$\sigma_N$  = modal strength of the weakest link in a sample containing  $N$  elements,

$\sigma_u$  = average strength of a unit cube of material containing  $N_u$  elements,

$\sigma_s$  = standard deviation of the modal strength of samples containing  $N_0$  elements,

and  $\sigma_s(N)$  = standard deviation of the modal strength of the weakest element in a sample containing  $N$  elements.

These formulae are based on the "weakest link theory", which can be analyzed mathematically if it is assumed that the frequency of occurrence of events is a continuous function (e.g. Weibull<sup>5</sup> or normal distribution). The "links" in this case are the macroflaws (or cracks) in the bulk material; not the microflaws.

Glucklich and Cohen<sup>10,11</sup> have indicated that effects other than statistical exist, since the total stored elastic energy increases with specimen volume. The energy released at onset of fracture is related to initiate fracture; in other words, this reduces the rock strength. This phenomenon has been recently discussed by Baecher<sup>12</sup>.



## 2.2 Effect of Confinement

There have been numerous studies investigating the effects of various aspects of confinement on rocks. It is not intended to review all of these completely in this section. Most of the pertinent work has been briefly discussed by Swanson<sup>13</sup>. The earliest experimental work was performed by Adams<sup>14</sup> and von Karmen<sup>15</sup>. However, significant headway was not made until the initiation of work by Griggs<sup>16</sup> and his coworkers<sup>17,18</sup>. Since then, of course, a number of researchers have conducted various types of studies under pressure several of which were presented at a symposium on rock deformation<sup>19</sup>. Baidyuk<sup>20</sup> has summarized some of the Russian and American work. Research in this area is still very active<sup>13,21,22</sup>. All of this work has been performed with small rock specimens, a few inches in diameter. As a result considerable light has been shed on the behavior of the rock matrix and the criteria of failure. Refinements to the Griffith hypothesis have been proposed<sup>23,24,25</sup> and appear to explain the rock fracture process under confinement fairly well. The extrapolation of these theories to larger rock masses is of doubtful value and hence large scale field testing has to be resorted to<sup>26</sup>. The U. S. Bureau of Mines has undertaken a rather comprehensive program to collect field data with the intention of correlating it into a hypothesis<sup>27</sup>. The contributions of Hoek<sup>28</sup>, Bieniawski<sup>9</sup>, Wawersik<sup>29</sup>, Cook<sup>30</sup>, and Houpert<sup>31</sup> to the mechanism of brittle failure in rock deserve to be noted even though the studies were not conducted under a confined state of stress.

### 3.0 EXPERIMENTAL APPARATUS

In order to conduct triaxial tests for the range of specimen sizes used on this project, four triaxial cells were set up as shown below:

Chamber I. D. (in.)	Specimen Diameter (in.)	Maximum Chamber Pressure (ksi)	Maximum Axial Load lb. x10 <sup>6</sup>
4.0	1.95	30	0.375
6.5	3.65	30	0.990
14.7	12	20	3.40
48.3	32 & 36	20 axial 10 confining	36.5

In a standard triaxial cell the axial load is supplied by an external loading machine. However, in order to achieve the large end loads required for the tests in this program, these chambers were separated into two regions by sliding pistons. The general configuration is shown in Fig. 1. One region contained the specimen, and was pressurized to the desired confining pressure. Axial load was transmitted to the rock by the sliding piston. The maximum axial stress in the rock depends upon the ratio of the rock and piston areas and the difference in the confining pressure and the axial chamber pressure. The specimen stresses are given by the following equations:

$$\begin{aligned}\sigma_2 &= \sigma_3 = P_3 \\ \Delta\sigma &= (P_1 - P_3) \frac{A_p}{A_r} \\ \sigma_1 &= \sigma_3 + \Delta\sigma\end{aligned}$$

where

$A_p$  = piston area

$A_r$  = specimen area

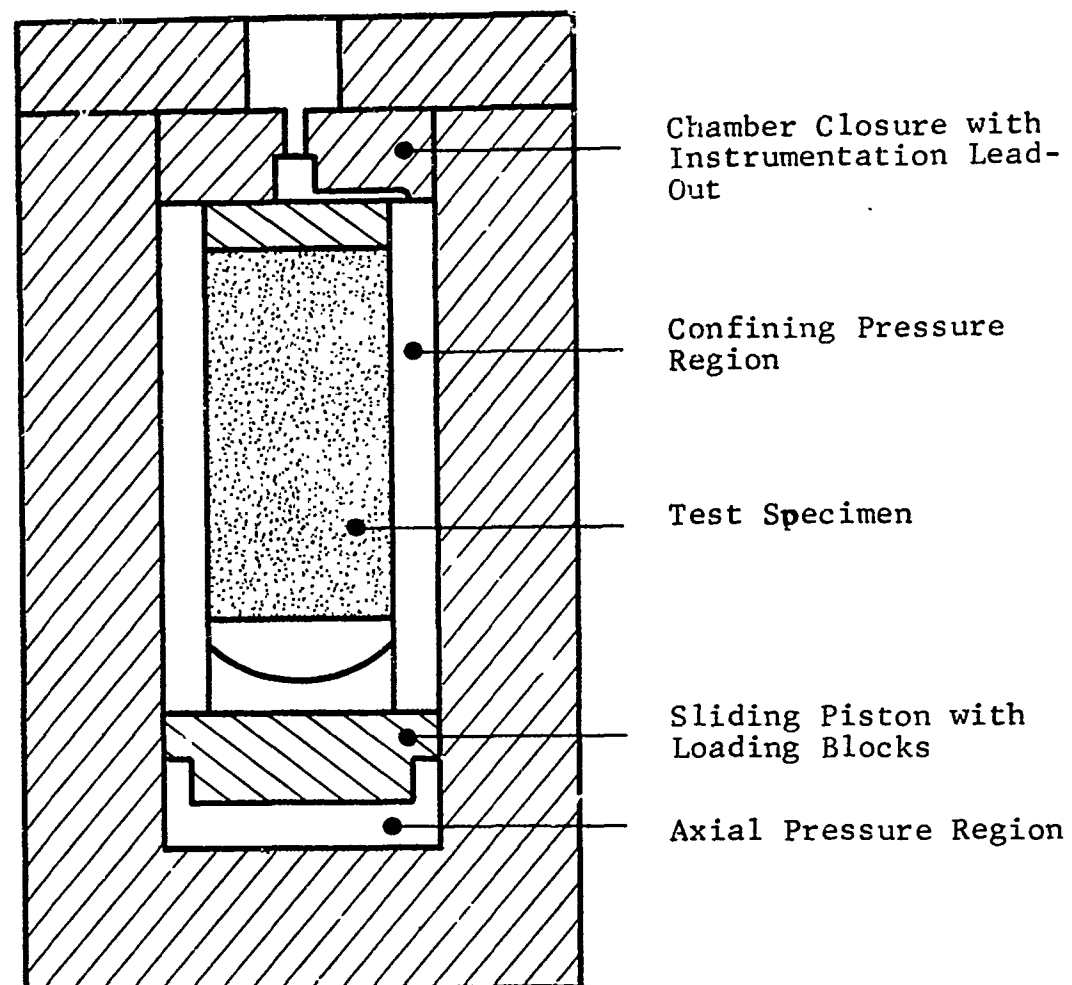


FIG. 1 TYPICAL TRIAXIAL CELL SCHEMATIC

$P_1$  = axial chamber pressure

$P_3$  = confining chamber pressure

$\Delta\sigma$  = deviator stress

$\sigma_1, \sigma_2$  and  $\sigma_3$  = principal stresses.

Reference to Figure 1 and the above equations confirms that if  $P_1 = P_3$ ,  $\Delta\sigma = 0$  and the specimen is under hydrostatic stress ( $\sigma_1 = \sigma_2 = \sigma_3$ ). For  $P_3 = 0$ , the specimen is unconfined, with  $\sigma_2 = \sigma_3 = 0$  and  $\sigma_1 = \Delta\sigma = P_1 A_p/A_r$ .

### 3.1 Small Test Cells

The three smaller test cells are incorporated into a testing system with centralized controls, instrumentation, and pumping systems. A schematic of this system is shown in Figure 2. The tests conducted in this system consisted of initial hydrostatic loading up to the desired confining pressure, followed by triaxial compression at constant  $\sigma_3$  above that pressure. At least one load-unload-reload cycle was observed for each test. Provision was made for pressure cross-connections between the confining pressure and axial pressure chamber volumes to insure hydrostatic conditions during the hydrostatic test phases.

### 3.2 48-Inch Test Cell

This test cell is shown in Figures 3 and 4. The basic unit is a 48" I.D. by 86" working length chamber having 20,000 psi design working pressure. The chamber walls are built up from rings 12" long which are held in place by a 3/4" thick liner on the inside diameter. The entire axial load is carried by a flexible reaction frame which was built up from steel strap. The 140 ton weight of chamber is substantially less than the weight that would have been required by conventional chamber design. This is the largest chamber currently available at IIT Research Institute, and is capable of applying axial loads of 36 million pounds

IIT RESEARCH INSTITUTE

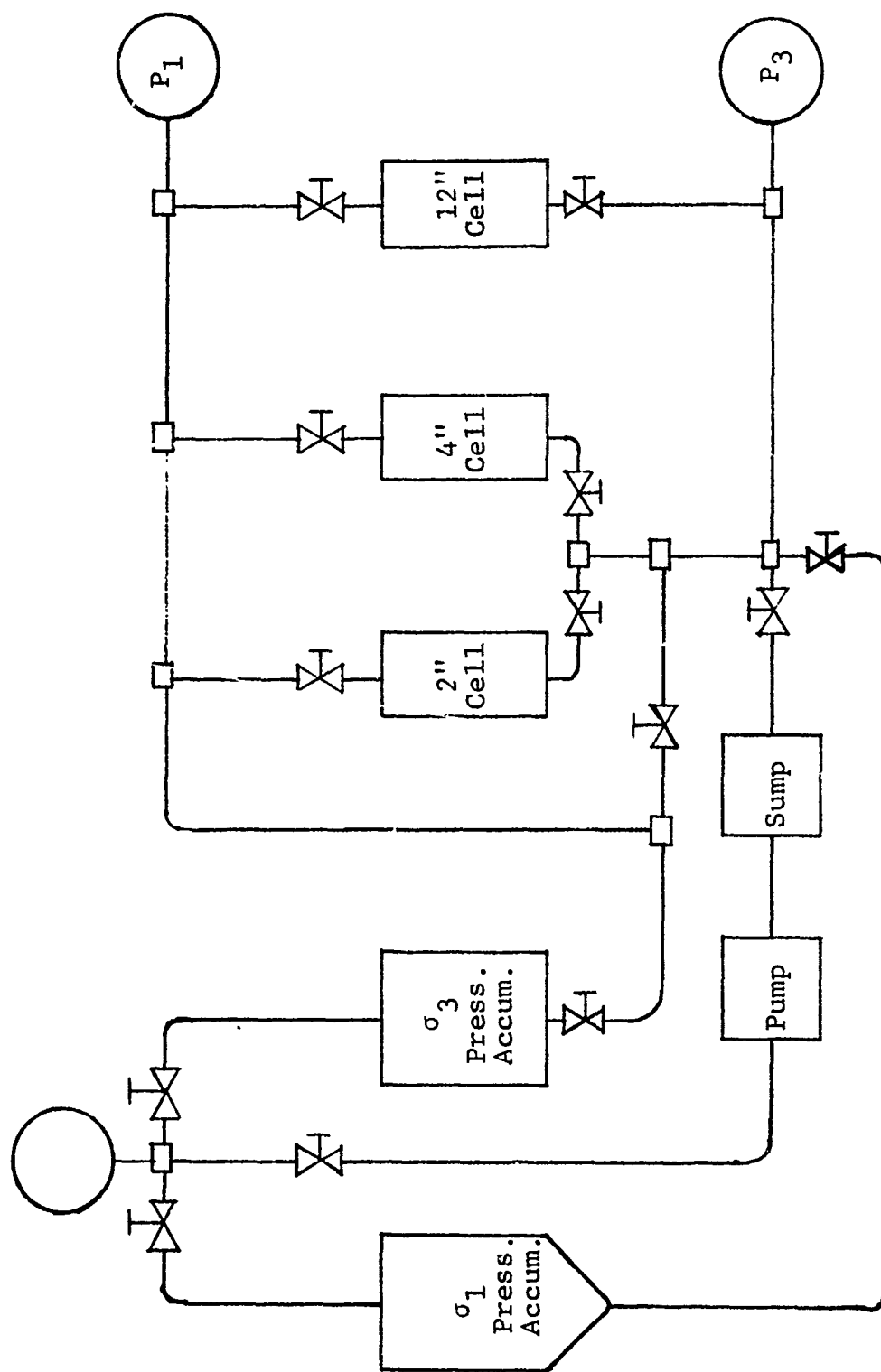


Fig. 2 SCHEMATIC OF SYSTEM FOR 2 IN., 4 IN., AND 12 IN. TRIAXIAL SPECIMENS

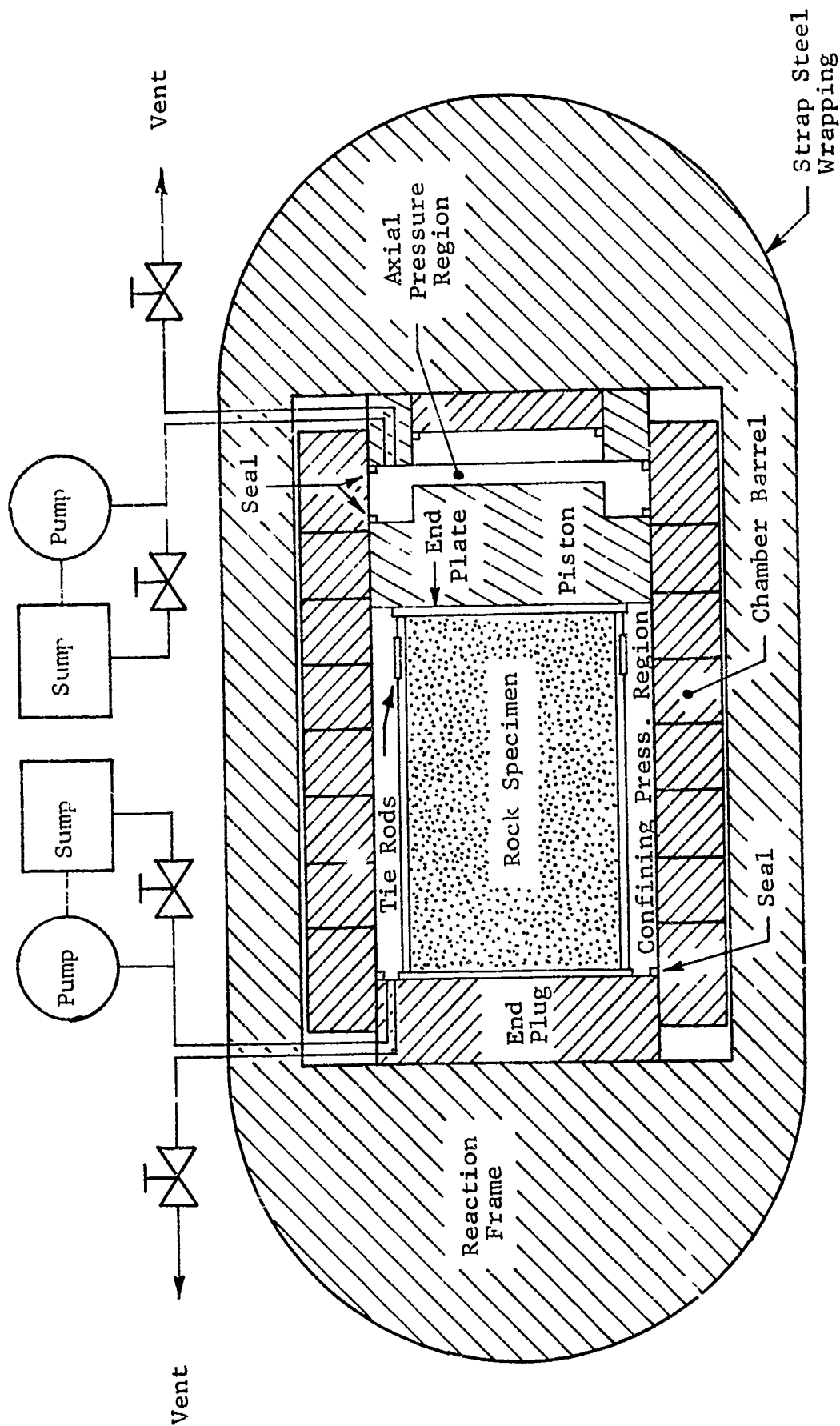


Fig. 3 SCHEMATIC OF 48 IN. I.D. TRIAXIAL CELL LAYOUT

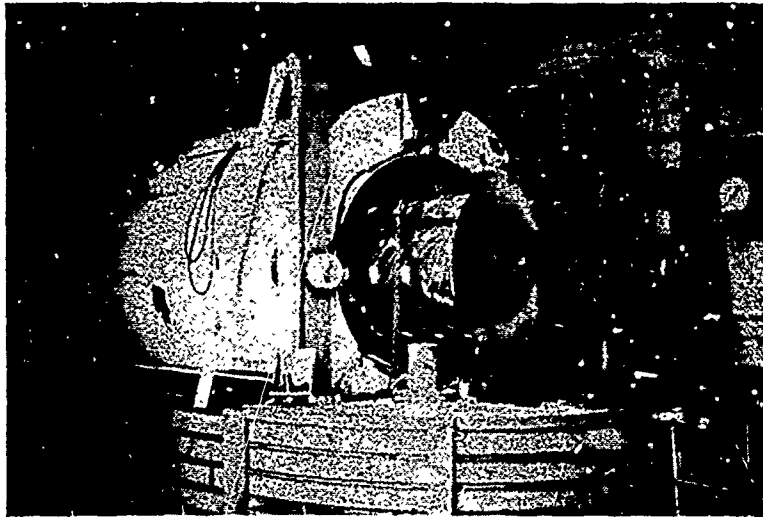


Fig. 32 IN. GRANITE SPECIMEN BEING  
LOADED INTO LARGE TRIAXIAL CHAMBER

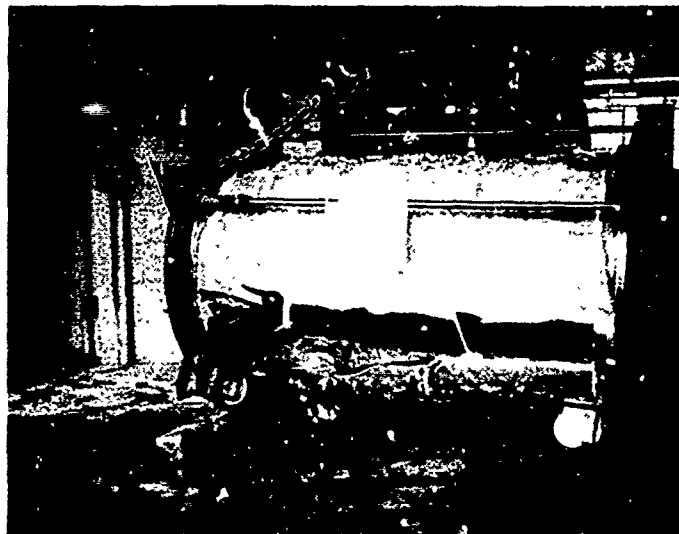


Fig 3 32 IN. GRANITE SPECIMEN AFTER  
TESTING AT CONFINING PRESSURE  
OF 2000 PSI

to rock specimens as large as 3 1/2 ft. in diameter.

As can be seen in the schematic, the pumping and control systems for this unit are simpler than for the small chambers. A separate pump was used at each end of the chamber. Accumulators were not used because the chamber volume itself is large in comparison with other available pressure chambers.

The operation of this chamber is similar to that of the smaller chambers, except that the turn-around time between tests is on the order of a week instead of an hour. The tests in this chamber differed slightly from those in the smaller test cells. In order to maintain seal integrity, a positive pressure differential of at least 200 psi was maintained across the sliding piston during the "hydrostatic" portions of the triaxial tests, and the axial pressure was not allowed to drop below 400 psi at the bottom of the load-unload-reload cycle. Had these precautions not been taken, there would have been danger of upsetting the piston seal, thus aborting the remainder of the test.

### 3.3 Specimen Preparation

Specimens of both rock types (Indiana limestone and Charcoal Black granite) were delivered to IITRI in the form of cores ranging from 12 in. to 36 in. in diameter. Extra rock was included to permit coring of the 2-in. and 4-in. dia. cores. These smaller cores were cut parallel to the axis of the larger cores so as not to introduce complications because of anisotropy. All cores were cut with a 1:2 dia to length ratio with the exception of the largest cores, which were all 60 in. long. Thus the aspect ratio of the Charcoal Black granite cores was  $32/60 = 1:1.87$  and that of the Indiana Limestone was  $36/60 = 1:1.67$ .

End preparation of the 2-in. and 4-in. dia cores consisted of facing and grinding on a lathe until the ends were plane and parallel to 0.0001 inches. The larger cores were capped in a specimen cage to permit handling. The capping material used was a steel-filled epoxy. Figure 4A and 4B each show an assembled 32-in. specimen in its cage. The cage tie rods were designed with end fittings that would accept



tensile load only. Since the maximum tensile load that could be applied to the cage by these tie rods corresponded to 30 psi compressive stress in the rock specimen, the effect of the cage on the rock was negligible.

An array of foil strain gages were mounted on each specimen as shown in Figure 5. The number used ranged from three rosettes on the 2-in. cores to thirty rosettes on the 32- and 36-in. cores. These were two-element rosettes with 1/4 in. gage length placed with the direction of rolling parallel to the specimen axis. The gage placement procedure included the following steps:

- grind the rock surface
- apply two thin coats of gage cement
- visual inspection for voids in the cement base
- affix gage and solder leads
- apply two coats of gage coat for water proofing
- check gage for continuity and response (soft eraser) and replace if necessary.

The instrumented cores were waterproofed with latex cement over the foil gages, and at least two coats of latex paint with a thickening agent over the entire rock surface. Waterproofing is very important in a triaxial test since both the loading conditions and the character of the rock can be changed by intrusion of fluid into the rock voids. In those tests where the specimens could not be loaded to failure on the second load cycle, the specimen was recovered intact and stripped of paint for visual inspection. In several cases, traces of oil were found under the paint, but typically the specimens were completely dry. In no case was there enough oil to do more than dampen a very small area on the specimen surface.

### 3.4 Instrumentation and Data Reduction

The instrumentation on this program included foil strain gages, and pressure gages. All data were recorded using an automatic digital data acquisition system. The pressures were read using Hiese bourdon gages and inserted

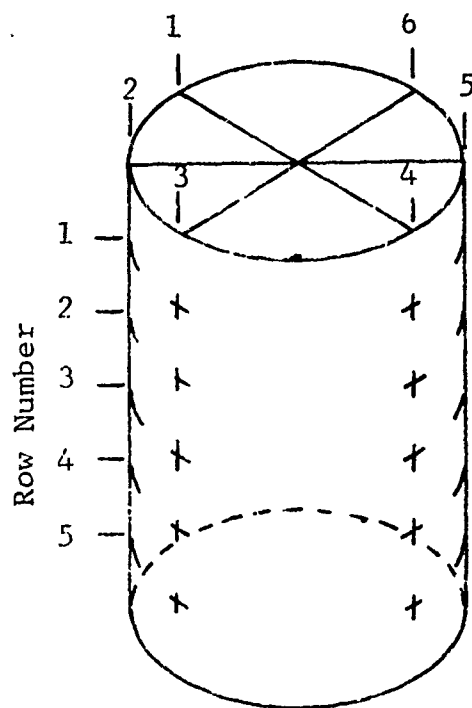


Fig. 5 SPECIMEN ORIENTATION AND ARRAY OF MEASUREMENT LOCATIONS

manually onto the data system output as they were read.

Due to the bulk of data involved, the data were reduced and plotted using an 1108 Univac computer. Two programs were employed in the reduction of each triaxial test. The first program plotted the raw strain data to show the behavior of the individual foil gages. On occasion, the response of individual strain gages differed radically from the majority of the gages. The cause of this behavior was then evaluated as either a key-punching error and corrected, or as actual failure in the operation of the gage, and the data discarded. Reasons for improper gage operation include actual gage failure, or a flaw in the specimen near the gage location. After the editing operation, the data were reduced by a program that solved the bridge equation for each gage location and printed out the individual strains and the strain averaged over the specimen. These data were evaluated for any consistent variation in strain distribution, such as might be caused by barreling of the specimen. If any variation actually occurred, its magnitude was too small to detect under the normal gage to gage variation. In addition to printed output, the following plots were produced for each test:

- Shear strain vs. deviator stress
- Volumetric strain vs. mean stress
- Circumferential and axial strain vs. axial stress
- Elastic, shear and bulk moduli vs. mean stress.

Data from each test was then assembled by hand to show trends from test to test.

#### 4.0 EXPERIMENTAL PROGRAM

The experimental work consisted of non-destructive tests and unconfined compression tests on 2-in. dia. cores, and the major series of triaxial compression tests.

##### 4.1 Non-Destructive Tests

A series of non-destructive tests were conducted on all cores. These tests provide information on the variability between specimens as well as an indication of the uniformity of individual specimens. These tests include:

- Schmidt Hammer
- Shore Sclerscope
- Dilatational Wave Velocity

In general these measurements were made on the cores at the locations of the foil strain gages. The Schmidt hammer rebound test was found to be strongly affected by the size of the small cores. The hammer is in contact with the rock for a relatively long time during impact, and the rebound height is influenced by the method being used to hold the small cores. After experimenting with several clamping and bedding arrangements, the most consistent technique found was to measure the Schmidt hammer rebound on the ends of the specimen rather than the sides. The specimen being tested was placed on a large block of the parent rock to reduce the amplitude of the reflected wave. This technique was used for all 2-in. dia. and 4-in. dia. specimens for the Schmidt hammer tests. Larger cores were tested on the cylindrical surface at gage location.

The velocity of the dilatational wave was measured at all gage locations on all cores. The system used for the small cores is shown in Figure 6A. The input signal is a single cycle square wave. This is amplified and used to drive a 1 MHz piezoelectric transmitting transducer. The signal transmitted through the rock is received by a similar transducer and displayed on a dual beam oscilloscope through an internal variable delay line. This signal is compared with the input

IIT RESEARCH INSTITUTE

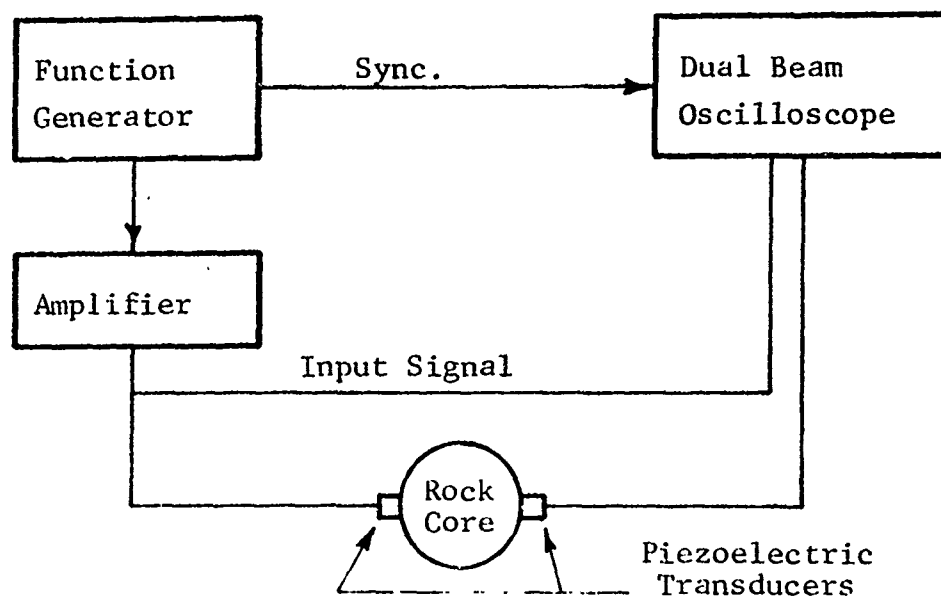


Fig. 6A ACOUSTIC VELOCITY SYSTEM FOR SMALL CORES

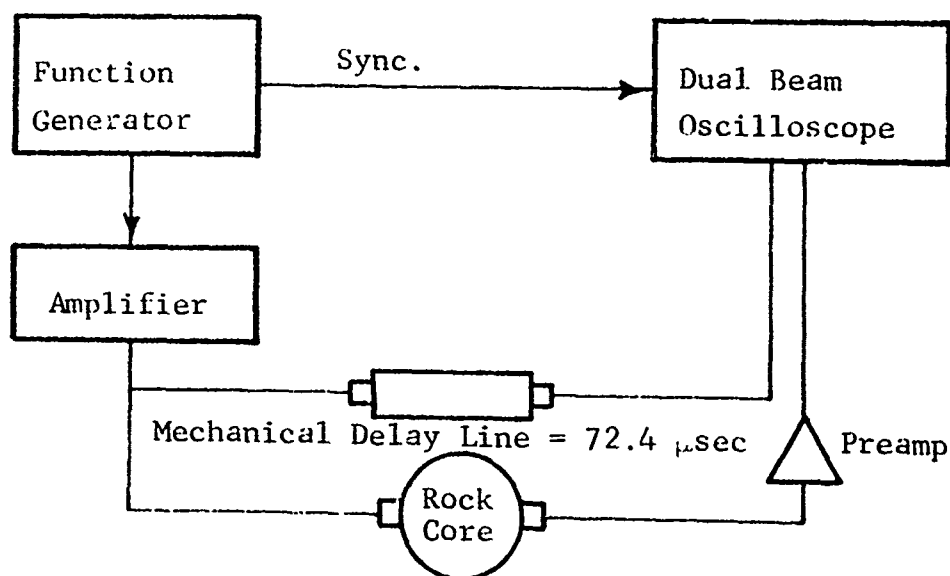


Fig. 6B ACOUSTIC VELOCITY SYSTEM FOR LARGE CORES

signal, and the variable delay line adjusted to achieve coincidence. The elapsed time is then read from the delay line. The system delay is easily measured by removing the rock specimen and placing the transducers face to face. Figure 6B shows the system used for the 32-in. and 36-in. dia cores. A mechanical delay line was introduced to allow the use of rapid sweep rates, and a preamp boosted the received signal. The operating frequency ranged from 300 kHz for the large cores to 1 MHz for the small specimens. A check was made to determine if the frequency response of the rock influenced the apparent time of arrival by making measurements on a single 2-in. dia specimen at frequencies between 10 kHz and 2 MHz. The results are plotted in Figure 7, and indicate no variation in time of arrival across the entire frequency range. The amplitude of the received signal is, of course, strongly dependent on input frequency.

#### 4.1.1 Results of Non-destructive Tests-Charcoal Black Granite

Of the three rapid non-destructive tests used to characterize the properties of the individual granite cores, the sonic velocity determinations were perhaps most useful. The Schmidt hammer test was found to be size dependent, the results of tests on the 2-in. dia cores being somewhat questionable. Various limitations of the Shore scleroscope test apparatus make this test inappropriate for determining gross properties in granite, unless test procedures are used that cannot fit into the category of "rapid non-destructive" test. For best results, the scleroscope should be firmly held vertically over the horizontal specimen surface, as conditions of plumbness and perpendicularity are critical. This test measures hardness over a very small area on the surface of the specimen, the rebound being affected by the type of individual grain that is impacted, and the proximity of the grain boundary. Recommended procedures for good results would involve cutting and polishing a small specimen that can be tested in a

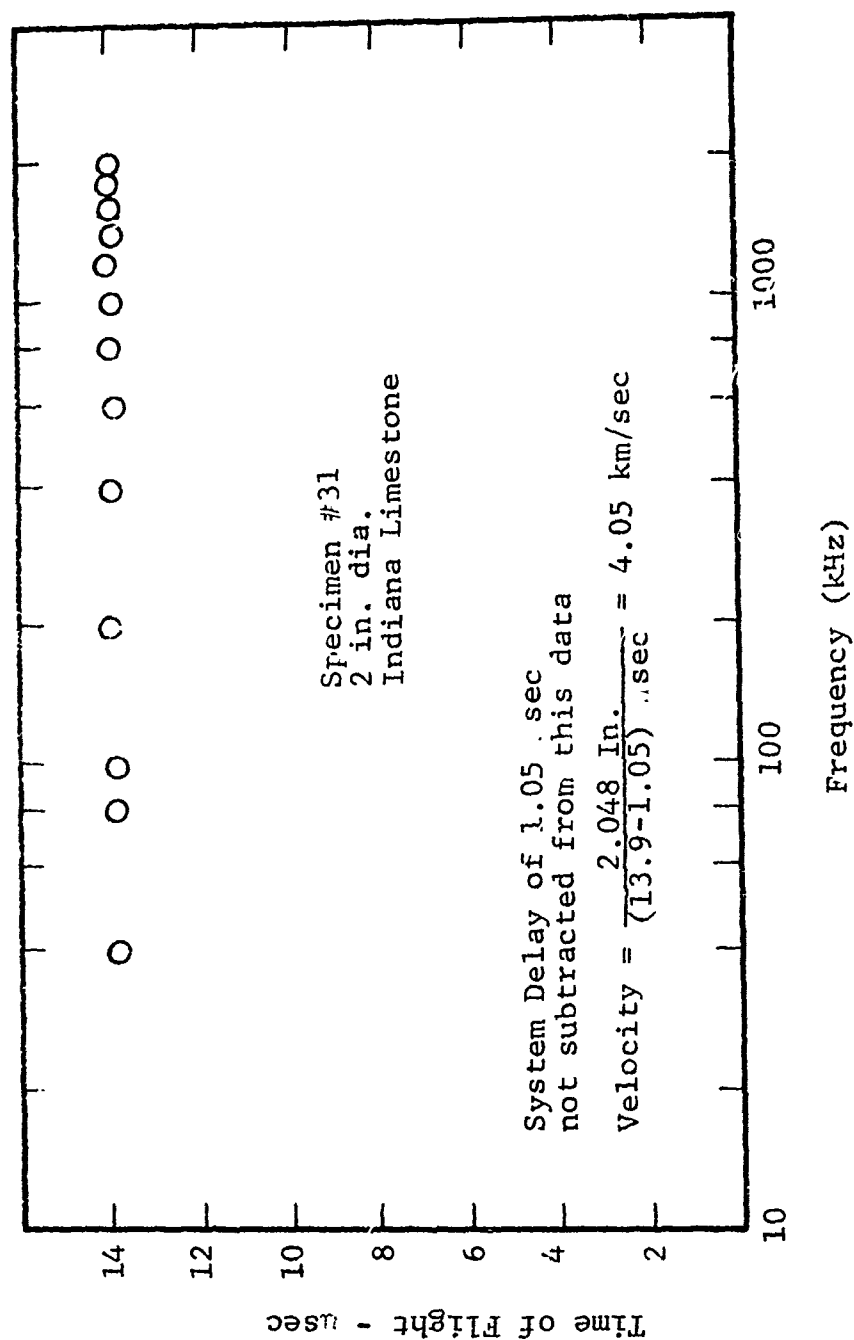


Fig. 7 TIME OF ARRIVAL MEASUREMENTS FOR A SINGLE SPECIMEN AT SEVERAL FREQUENCIES

mounted scleroscope apparatus. The striker should be targeted on individual grains, and a number of replicate tests conducted to determine the hardness of the individual constituent minerals in the rock. This procedure was not possible in this program since the individual cores could not be sectioned prior to triaxial testing. The scleroscope was hand held vertically by reference to an attached level bubble, and the test cores rolled over the floor to make the desired test point horizontal. Figure 8 is a histogram showing the scleroscope readings for the granite. The readings taken on 12 in. dia cores are shaded. This size was the only one having two distinct peaks at scleroscope readings of 50 and 95. The 2 in., 4 in. and 32 in. dia. specimens displayed only the upper peak at readings of approximately 60 to 90. Note, also that nearly all readings above 100 occurred on the 12-in. dia specimens.

The Schmidt hammer tests proved more interesting, giving the first evidence that the 12-in. dia granite had properties significantly different from the other sizes. It should be remembered that the 32-in. dia cores and the 12-in. dia cores were quarried on different occasions, although from the same quarry. The 2-in. and 4-in. dia cores were drilled from a piece of 32-in. dia stock during the conduct of this research program, and should display properties similar to the 32-in. cores. Figure 9 shows histograms of granite specimens. The distributions of results on 12-in. and 32-in. dia cores had standard deviations near  $2\frac{1}{2}$  Schmidt hammer units, but the means of the two distributions differ by approximately two standard deviations, that is, 5.1 units. The 2-in. and 4-in. cores gave readings that were influenced by their small size. Various clamping and bedding arrangements were tried in an effort to eliminate rebound of the cores and to reduce the experimental scatter within each size. The most consistent results were obtained by testing the ends of the cores, which



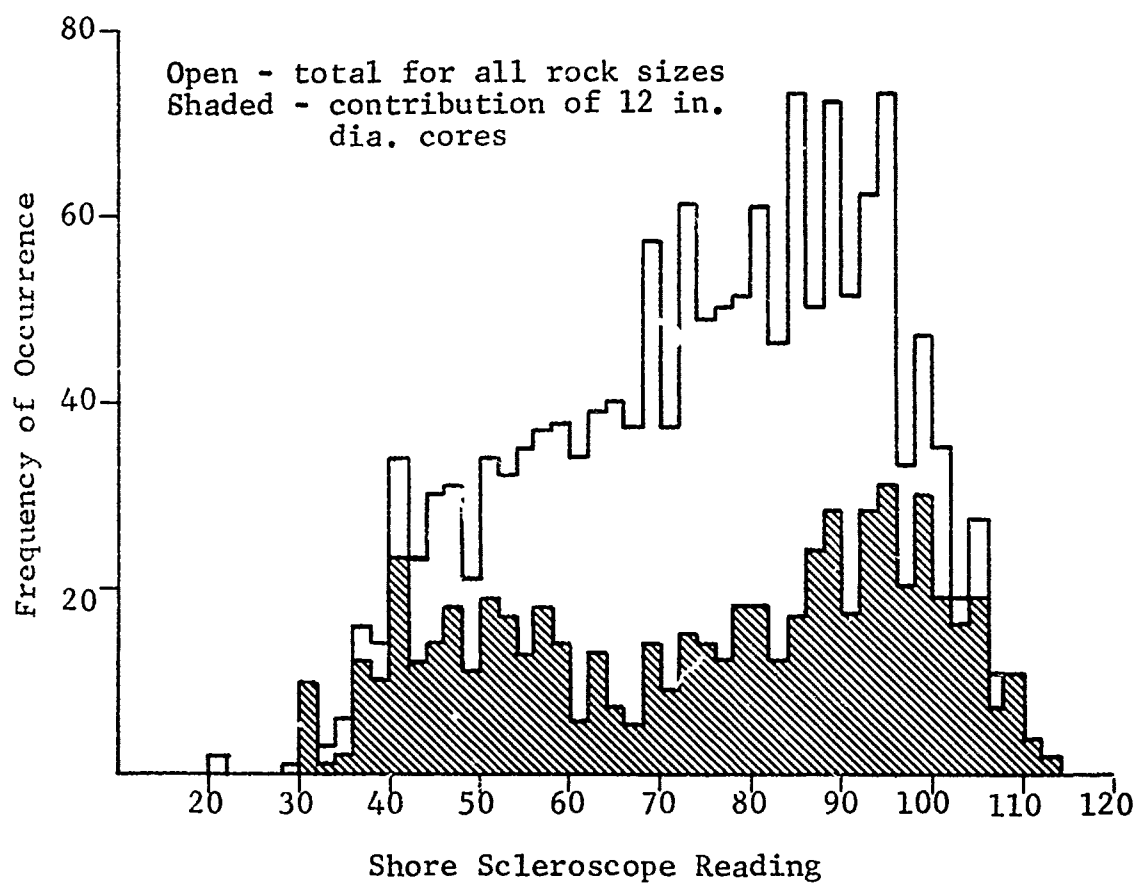


Fig. 8 FREQUENCY OF OCCURRENCE OF SHORE SCLEROSCOPE READINGS FOR CHARCOAL BLACK GRANITE

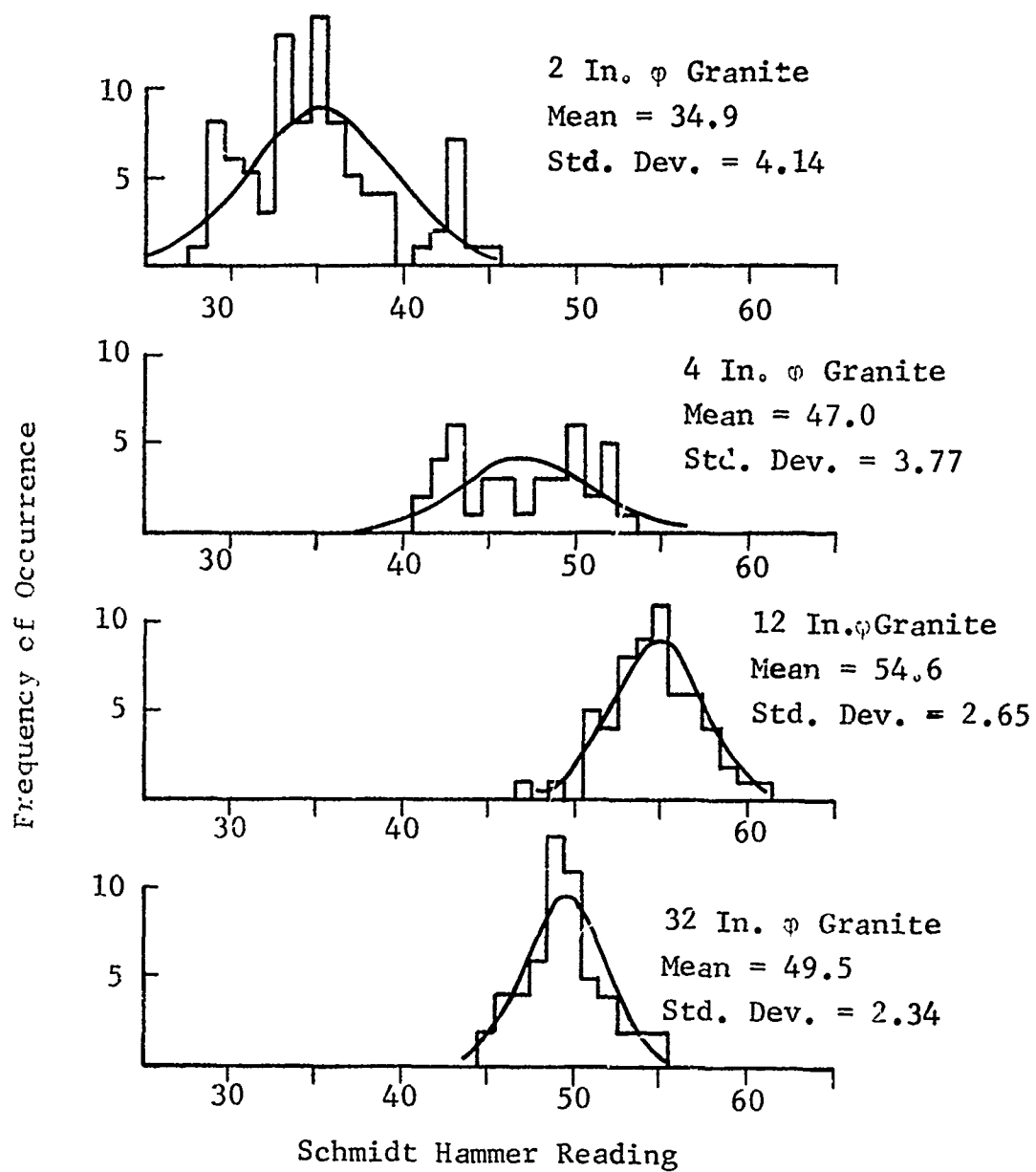


Fig. 9 FREQUENCY OF OCCURRENCE OF SCHMIDT HAMMER READINGS FOR CHARCOAL BLACK GRANITE

were placed on heavy cubes of granite. This increased the path length of the stress wave in the core, and reduced the amplitude of the reflected wave at the risk of introducing variations due to anisotropy. The problem was not completely solved, since both 2-in. and 4-in. dia cores displayed standard deviations of approximately 4 units, and depressed mean values, especially in the case of the 2-in. dia specimens.

The sonic velocity determinations confirmed both of the above tentative conclusions, that the 12-in. cores were slightly more competent, and that the variations in the 2-in., 4-in. and 32-in. dia. Schmidt hammer readings were caused by the small specimen size. The first three histograms in Figure 10 show the sonic velocities measured in 2-in., 4-in. and 32-in. dia cores. The measured velocities spread rather uniformly, across the range of 4.3 to 5.1 km/sec. The accuracy of the measuring system on replicate individual readings was found to be about 2%, so that the observed variation is inherent in the specimens. The last histogram in Figure 10 shows all the granite sonic data, with the normal distribution curve for the 12-in. cores shown separately. Again, the 12-in. dia cores are significantly more competent than the other granite cores, with sonic velocities greater by about 20%.

A detailed summary of the mean sonic velocities and standard deviations for each granite core is presented in Table 1. This shows that much of the scatter in Figure 10 results from variation from core to core. The 4-in. and 32-in. dia cores consistently have low standard deviations for individual cores, so that the normal distribution curve shown in Figure 10 with standard deviation = 0.118 provides a good visualization of the greatest possible measuring system errors.

The anisotropy of the Charcoal Black granite was evaluated by checking the variation of sonic velocity on three different diameters of the 2-in., 4-in., and 12-in. dia cores.

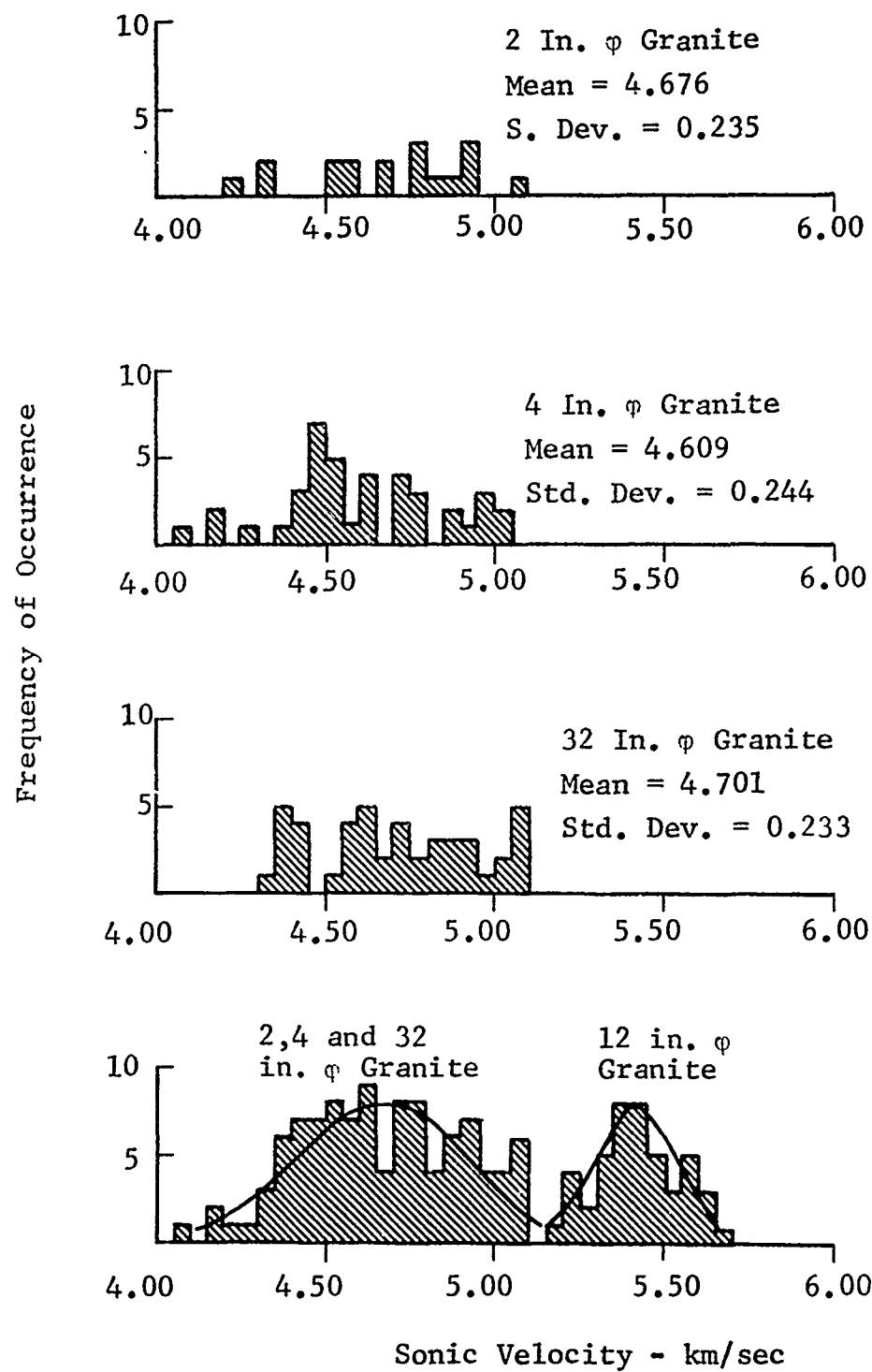


Fig. 10 FREQUENCY OF OCCURRENCE OF SONIC VELOCITY DETERMINATIONS IN CHARCOAL BLACK GRANITE

TABLE 1

SONIC VELOCITY FOR INDIVIDUAL CHARCOAL BLACK GRANITE CORES  
(km/sec)

2" dia mean std. dev	#6 4.83 -	#7 4.79 -	#8 4.53 -	#9 4.40 -	#10 4.75 -	all 2" 4.676 0.235
4" dia mean std. dev	#11 4.60 0.17	#12 4.77 0.19	#13 4.78 0.18	#18 4.37 0.18	#19 4.36 0.16	all 4" 4.609 0.244
12" dia mean std. dev	#45 5.55 0.064	#46 5.39 0.055	#47 5.48 0.095	#48 5.27 0.064	#49 5.35 0.041	all 12" 5.409 0.118
32" dia mean std. dev	#2 4.69 0.094	#3 4.97 0.085	#4 4.45 0.096			all 32" 4.701 0.233

In all cases, the variation between mean velocities on different diameters was less than the standard deviation of the individual means. This indicates that any consistent anisotropy present was smaller than the core-to-core variations. The 12-in. dia cores were also checked to determine if a consistent variation existed along the length of the cores. In this case also, the core-to-core variation was large in comparison to any consistent anisotropy. The 32-in. dia cores were not checked because the appropriate directions were not marked on the individual cores at the quarry. The data is summarized in Table 2.

#### 4.1.2 Results of Nondestructive Tests-Indiana Limestone

The comments regarding the Shore scleroscope and Schmidt hammer tests on granite apply to a lesser degree on the limestone. The limestone does not have the large grain size of the granite, so the scleroscope should show a single peak value, and the reduced sonic velocity should result in more consistent rebound hammer tests on the small cores.

The results of all Shore scleroscope readings on limestone are plotted in Figure 11. There was little variation related to core size in these tests. The tests scattered about a mean value of 13.95 with a standard deviation of 4.56 scleroscope units.

The Schmidt hammer results are plotted for the individual specimen sizes in Figure 12. The 2-in and 4-in. dia cores were tested parallel to the axis in the same manner as the small granite cores, and display little shift in the mean values.

The sonic velocity determinations are plotted for each size and for all sizes together in Figure 13. Again, there is no significant variation between the different sized specimens.

The anisotropy of the Indiana limestone was investigated by evaluating the three 36-in. dia cores. The 45 individual acoustic velocity tests on these cores had a mean

TABLE 2

ANISOTROPY OF CHARCOAL BLACK GRANITE  
(km/sec)

	Radial Variation			Axial Variation		
	col. 1	col. 2	col. 3	row 1	row 3	row 5
2" dia mean std. dev	4.70 0.327	4.69 0.203	4.64 0.194			
4" dia mean std. dev	4.61 0.379	4.59 0.139	4.63 0.155			
12" dia mean std. dev	5.42 0.135	5.42 0.113	5.40 0.110	5.39 0.110	5.44 0.145	5.42 0.086

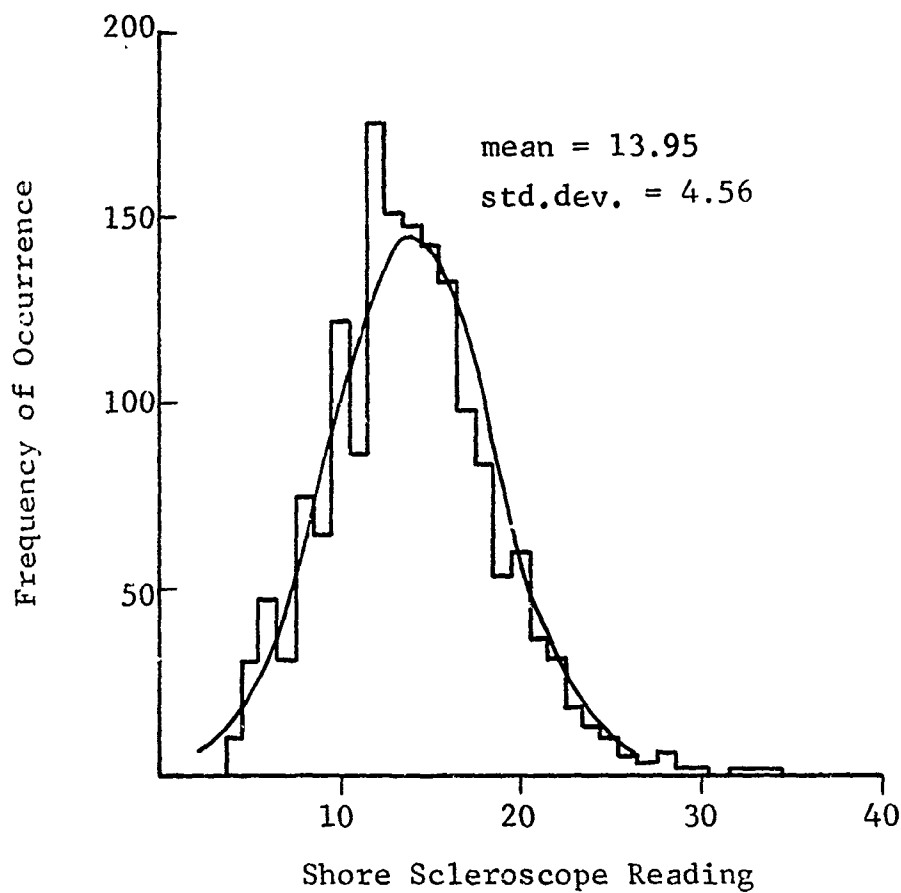


Fig.11. SHORE SCLEROSCOPE READINGS FOR INDIANA LIMESTONE



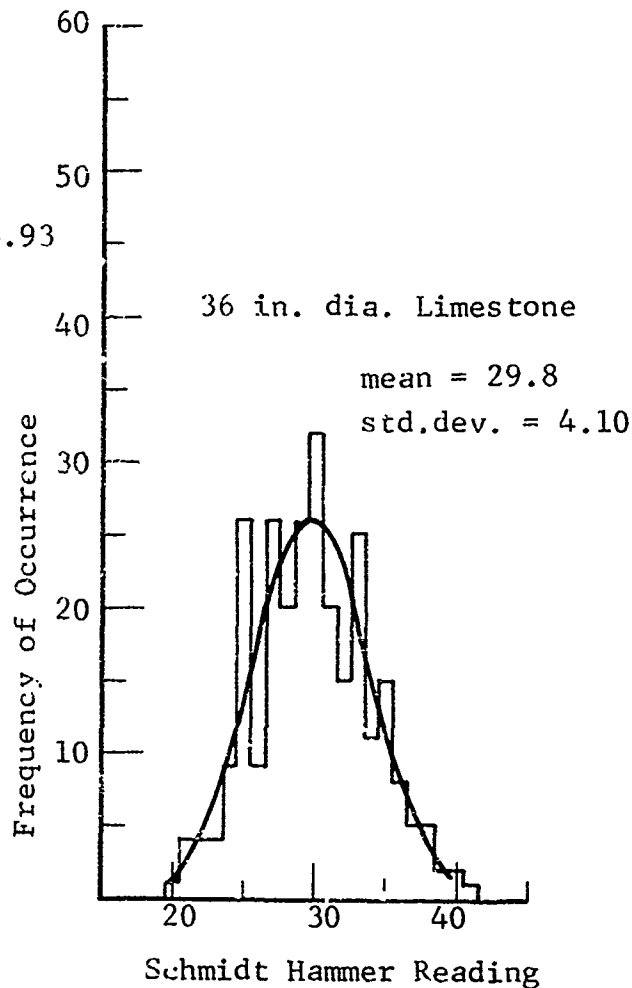
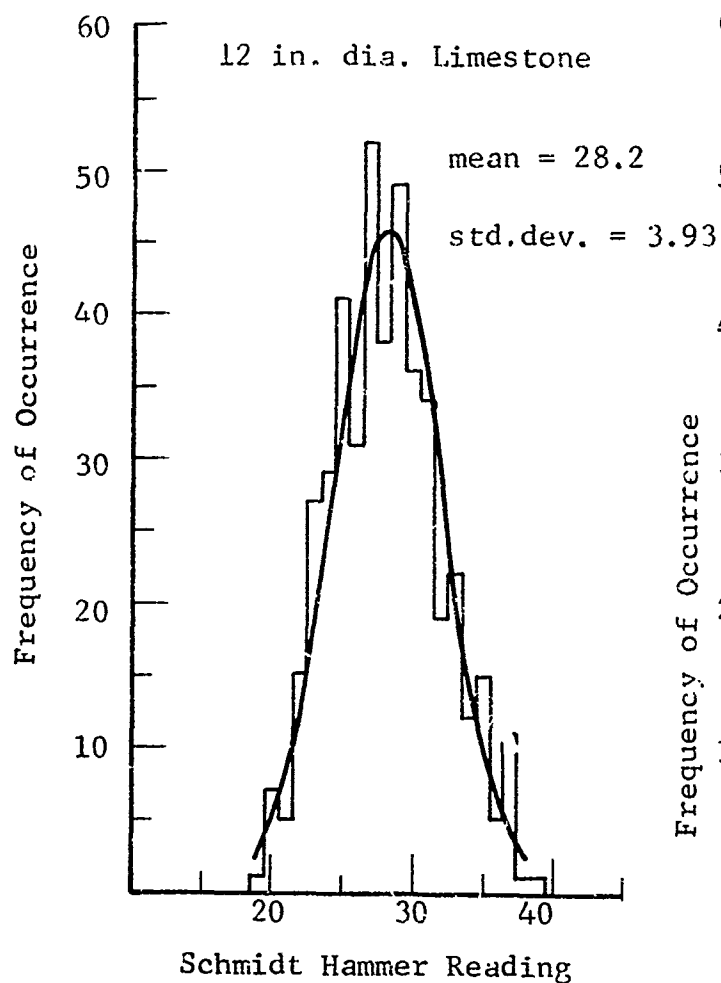
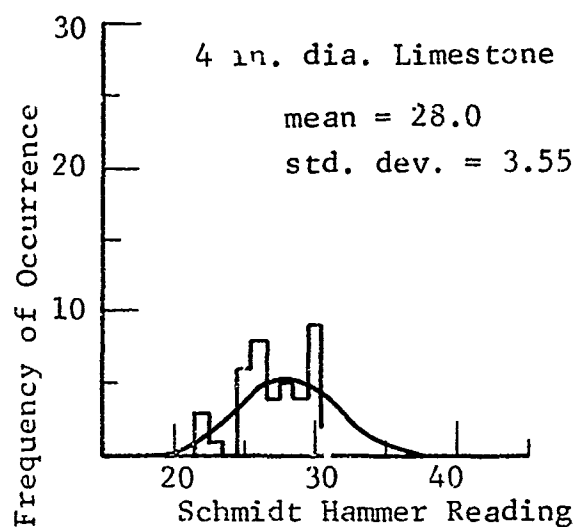
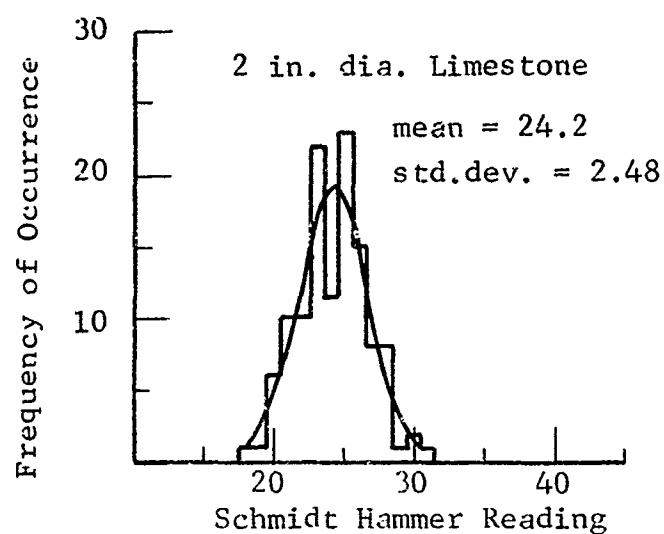


Fig. 12 FREQUENCY OF OCCURRENCE OF SCHMIDT HAMMER READINGS  
FOR INDIANA LIMESTONE

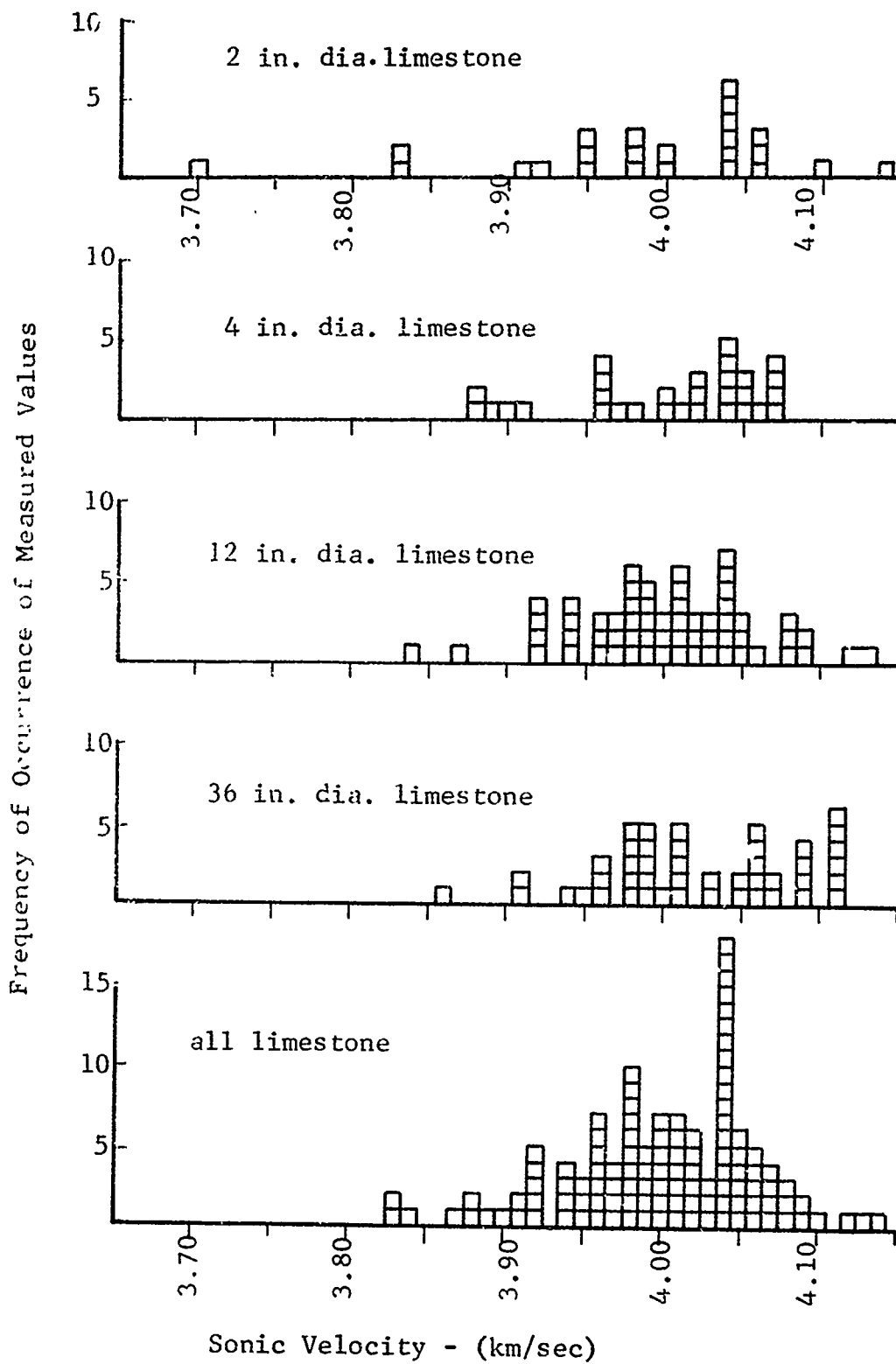


Fig.13 SONIC VELOCITIES FOR INDIANA LIMESTONE

value of 4.021 km/sec, with 95% confidence levels at  $\pm 0.017$  km/sec and a standard deviation of 0.058 km/sec. This value of 4.021  $\pm 0.017$  km/sec is taken as the acoustic velocity in Indiana limestone. These 45 readings may be separated into 3 groups of 15 readings, each group spaced at 60-deg intervals around the axis of the core, or as 5 groups of 9 readings, each group spaced at 10 in. intervals down the length of the core. In this fashion the variation in acoustic velocity can be considered as a function of direction in the horizontal plane, or as a function of the vertical depth in the bedding plane. This nonemclature, and the variation of acoustic velocities as a function of direction and depth are indicated in Figure 14. Note that in all cases, the 95% confidence levels for the individual subgroups include the mean value of 4.021 km/sec computed for the entire 45 reading group.

Looking at the variation of acoustic velocity, it appears that the maximum velocity would be measured along a diameter between 2-5 and 3-6, along a quarry bearing of N-80°-W, and the lowest velocity would lie along a bearing of N-10°-E. The maximum variation is on the order of 1-1/2 percent of the mean value. Considering the variation of acoustic velocity with depth, there may exist a trend of increasing velocity with depth. The slight reversal of this trend at row no. 5 may be a real effect caused by the presence of the bedding plane in the formation. In any case, the variation is on the order of 1% or less. The acoustic velocities for all subgroups lie near or within the 95% confidence levels for the entire group of measurements.

The results of all nondestructive tests on both rock types are summarized in Table 3.

#### 4.2 Classification Tests

In addition to the nondestructive tests to evaluate the specimen-to-specimen variability, petrographic analysis,

Specimen Orientation  
and Array of Measurement  
Locations

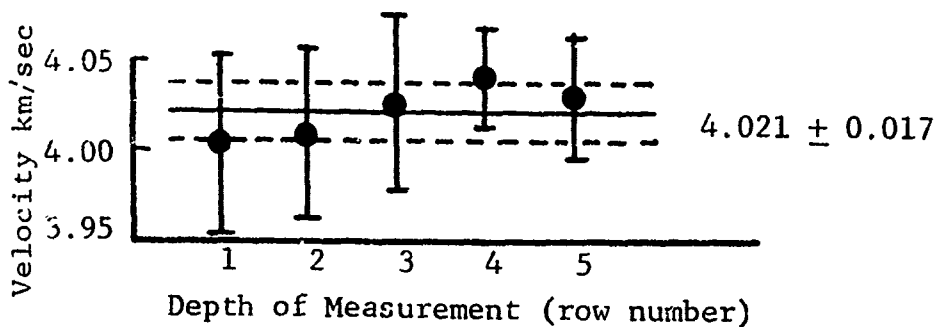
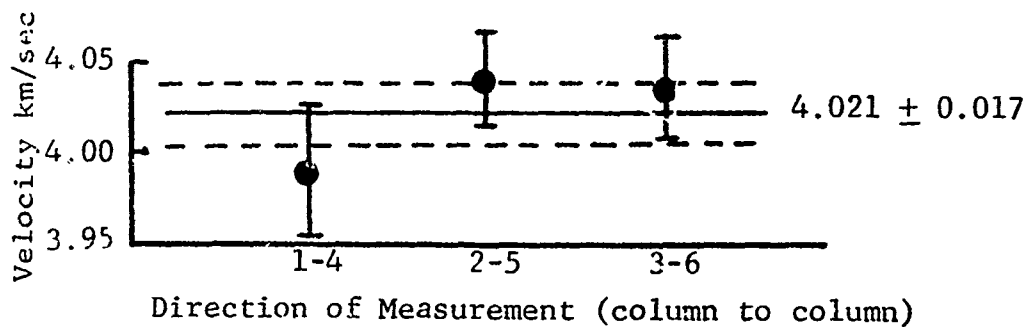
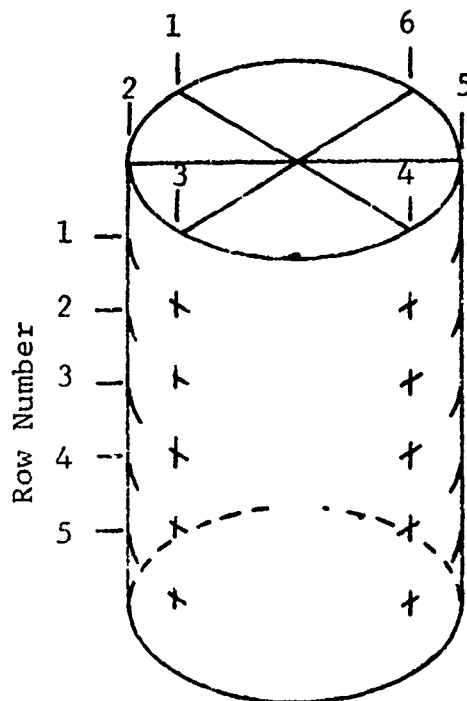


Fig. 14 ACOUSTIC VELOCITIES IN 36-IN. DIA INDIANA LIMESTONE

TABLE 3

SUMMARY OF NONDESTRUCTIVE TEST RESULTS  
SHOWING MEANS AND STANDARD DEVIATIONS

	Shore sclerescope		Schmidt Hammer		Sonic Velocity (km/sec)	
	mean	$\sigma$	mean	$\sigma$	mean	$\sigma$
2 in. dia granite	63.8	-	34.9	4.14	4.68	0.24
4 in. dia granite	83.1	-	47.0	3.77	4.61	0.24
12 in. dia granite	75.4	-	54.6	2.65	5.41	0.11
32 in. dia granite	74.7	-	49.5	2.34	4.70	0.23
2 in. dia limestone	12.7	3.48	24.2	2.48	3.99	0.10
4 in. dia limestone	14.6	4.53	28.0	3.55	4.00	0.06
12 in. dia limestone	14.4	4.40	28.2	3.93	4.00	0.06
36 in. dia limestone	14.4	4.99	29.8	4.10	4.02	0.06

tensile and unconfined compression tests were conducted to define the rock types.

#### 4.2.1 Petrographic Analyses

Petrographic analyses for the two rock types were conducted under the direction of Dr. A. Howland of Northwestern University in Evanston, Illinois. These reports are reproduced below.

##### Charcoal Black Granite

###### Macroscopic

Gray medium-grained, equigranular; grain size generally 1-3 mm; light gray feldspar, black hornblende, and dark brown to black biotite recognizable.

###### Microscopic

Texture: porphyritic: rectangular crystals of plagioclase 2.5-3.5 mm. long in a subhedral to anhedral interlocking aggregate of plagioclase, alkali feldspar, biotite, hornblende, and quartz with grain size largely in the 0.3 - 1.0 mm. range.

###### Mineralogy

###### Plagioclase ca. 50%

Euhedral to subhedral crystals in two distinct size ranges, giving a porphyritic texture. Fine polysynthetic twinning and strong oscillatory zoning ranging from about An<sub>25</sub> in the cores to An<sub>14</sub> in the outer zones; thin untwinned albitic rims. Many inclusions of biotite, hornblende, and magnetite. Slightly clouded with fine sericitic alteration.

###### Alkali feldspar ca. 15%

Subhedral to anhedral grains, fine perthitic intergrowths, grid microcline twinning visible in some grains.

###### Biotite ca. 15%

Euhedral to subhedral plates, brown, many dark haloes around zircon inclusion.

###### Quartz ca. 10%

Strong tendency to interstitial occurrence,

IIT RESEARCH INSTITUTE

filling in between rectangular feldspar grains.

Hornblende ca. 7%

Pale green to yellow green pleochroism, complexly twinned and intergrown with magnetite, some contain cores of relict pyroxene (included in hornblende percentage).

Magnetite ca. 3%

Separate grains and intergrowths in hornblende.

Apatite

Many needles and stout prisms included in other minerals.

Zircon

Inclusions in biotite.

This rock would classify as a granodiorite.

### Indiana Limestone

#### Macroscopic

Fine-grained porous light gray limestone; abundant oolites and fossil fragments visible with the hand lens.

#### Microscopic

Clastic limestone composed of oolites 0.1 - 0.15 mm. in diameter, fossil fragments ranging up to 1.5 mm. in length and about 0.1 mm. thick generally aligned parallel to the bedding, angular to subangular polycrystalline calcite fragments, and calcite cement.

Oolites show both concentric and radiating structures, the former much more abundant. Some have overgrowths of calcite. They form about 35% of the rock.

Fossil fragments with either fibrous or granular internal structure are about 30% by volume. Grains of polycrystalline calcite and clear single plates of calcite cement are about 20% by volume.

Pore space is estimated as about 15% of the thin section, but some interstitial material may have been lost in the grinding of the section.

#### 4.2.2 Tensile and Compressive Tests

Tensile and unconfined compression tests were conducted on 2-in. dia specimens in accordance with ASTM specifications. The unconfined compression test specimens were instrumentated, and the data included in the body of the analysis as triaxial tests having  $\sigma_3=0$ .

rock type	tensile strength (psi)	compressive strength (psi)
granite	1340	18700
limestone	290	3970

#### 4.3 Description of Constitutive Equations

In order to conveniently describe and analyze the rather large amount of data generated during this program, the data for the individual tests were fit to descriptive models. The variation in the model parameters is then analyzed for the range of specimen sizes and confining pressures employed in the study. The models that were chosen are described in greater detail in a previous report, as well as the underlying theory. Briefly, the constitutive equations for an isotropic linear elastic material are written in terms of the volumetric response and the distortional response through the use of the deviatoric stress and strain tensors, defined by:

$$\epsilon'_{ij} = \epsilon_{ij} - \frac{1}{3} \epsilon_{kk} \delta_{ij} \quad \text{deviator strain} \quad (1)$$

$$\sigma'_{ij} = \sigma_{ij} - \frac{1}{3} \sigma_{kk} \delta_{ij} \quad \text{deviator stress} \quad (2)$$

in which

$$\sigma_{ij} = \text{stress tensor}$$

$$\epsilon_{ij} = \text{strain tensor}$$

$$\delta_{ij} = \text{Kronecker delta}$$

IIT RESEARCH INSTITUTE



The linear elastic isotropic constitutive equation given by:

$$\sigma_{ij} = \lambda \delta_{ij} \epsilon_{kk} + 2 \mu \epsilon_{ij} \quad (3)$$

in which  $\lambda$  and  $\mu$  are Lamé's constants, are thereby transformed into

$$\sigma_{ij} = k \delta_{ij} \epsilon_{kk} + 2G \epsilon'_{ij} \quad (4)$$

in which  $G$  and  $k$  are respectively the shear and bulk moduli, given by:

$$k = \frac{\sigma_{kk}}{3\epsilon_{kk}} \quad (5)$$

$$G = \frac{\sigma'_{ij}}{2\epsilon'_{ij}} \quad (6)$$

Nonlinear behavior is incorporated by using incremental constitutive equations and defining  $G$  and  $k$  as functions of one or more of the stress invariants. Inelastic behavior may be incorporated by defining separate load and unloading moduli.

A nonlinear hysteretic model used by Seaman and Whitman<sup>32</sup> to study the behavior of sand appears to be suitable for representing the hydrostatic behavior of rock. The stress-strain curve for this model is shown in Figure 15.

For virgin loading

$$\sigma_m = A_1 \epsilon_v^n \quad (7)$$

and for unloading and reloading

$$\sigma_m = A_2 (\epsilon_v - \epsilon_{v\ell})^n \quad (8)$$

in which

$\sigma_m$  is mean stress

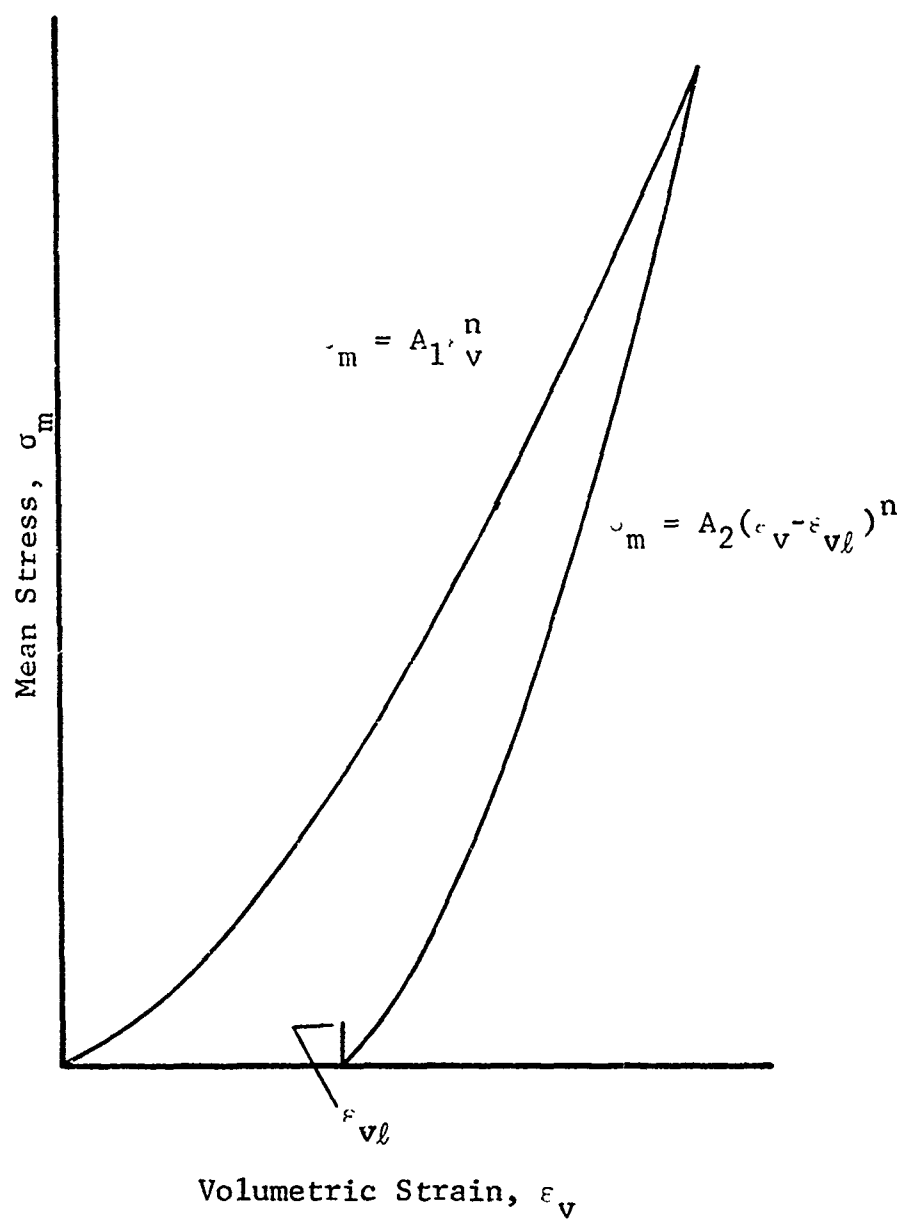


FIG. 15 IDEALIZED HYDROSTATIC BEHAVIOR OF GRANULAR MATERIALS  
(after Seaman and Whitman<sup>10</sup>)

$\epsilon_v$  is volumetric strain

$\epsilon_{v0}$  is residual volumetric strain

$A_1$ ,  $A_2$  and  $n$  are material properties

This model represents both the nonlinear and the inelastic behavior of the rock observed under hydrostatic loading.

Application of the mathematical model in a computer code would perhaps be most convenient in an incremental form using tangent values of bulk modulus,  $k_t$ . This modulus is a function of mean stress and for a given stress represents the slope of the curve at that stress level.

For loading

$$k_t = \frac{d\sigma_m}{d\epsilon_v} = n A_1^{1/n} \sigma_m^{(n-1)/n} \quad (9)$$

and, for unloading and reloading

$$k_t = \frac{d\sigma_m}{d\epsilon_v} = n A_2^{1/n} \sigma_m^{(n-1)/n} \quad (10)$$

Note that in this model the modulus for unload-reload is larger than the modulus for virgin loading at any given stress level. Only loading models were generated in this work.

#### 4.4 Triaxial Compression

A triaxial compression test normally consists of two phases. First, a hydrostatic confining stress,  $\sigma_c$ , is applied to the specimen so that the principal stresses are all equal to  $\sigma_c$ . Then, two principal stresses,  $\sigma_2$  and  $\sigma_3$ , are kept constant at  $\sigma_c$  while the third principal stress,  $\sigma_1$ , is increased. For these conditions one of the components of the deviator stress is

$$\sigma'_{11} = \sigma_1 - 1/3 (\sigma_1 + 2\sigma_3) = 2/3 (\sigma_1 - \sigma_3) \quad (11)$$

If the material is isotropic two principal strains,  $\epsilon_2$  and  $\epsilon_3$ , are also equal, meaning that the corresponding component of deviator strain is

$$\epsilon'_{11} = \epsilon_1 - 1/3 (\epsilon_1 + 2\epsilon_3) = 2/3 (\epsilon_1 - \epsilon_3) \quad (12)$$

Thus, for triaxial conditions the shear modulus may be determined from

$$\frac{\sigma'_{11}}{2\epsilon'_{11}} = \frac{\sigma_1 - \sigma_3}{2(\epsilon_1 - \epsilon_3)} \quad (13)$$

At low stress levels shear modulus increases relatively rapidly with mean stress; however, at higher stresses it remains relatively constant. Torsional wave velocities were measured in cylinders of different granites exposed to hydrostatic pressure between 1 kg/cm<sup>2</sup> and 4,000 kg/cm<sup>2</sup> by Birch and Bancroft.<sup>33</sup> From the wave velocities the modulus of rigidity, which is identical to the shear modulus, was determined and is shown as a function of mean stress in Figure 16. Also shown in Figure 16 are values of shear moduli for specimens of Charcoal Black granite determined from triaxial tests performed during this study and a previous study. The moduli determined by Birch and Bancroft and those for the Charcoal Black granite are in good agreement and increase approximately with the 1/10 power of the mean stress.

Values of shear modulus shown in Figure 16 are tangent values,  $G_t$ , which refer to the slope of the deviator stress value. For nonlinear behavior the tangent shear modulus is taken as a function of mean stress and may be calculated from

$$G_t = 1/2 \frac{d(\sigma_1 - \sigma_3)}{d(\epsilon_1 - \epsilon_3)} \quad (14)$$

The functional relationship with mean stress may be written as

$$G_t = c \sigma_m^{0.1} \quad (15)$$

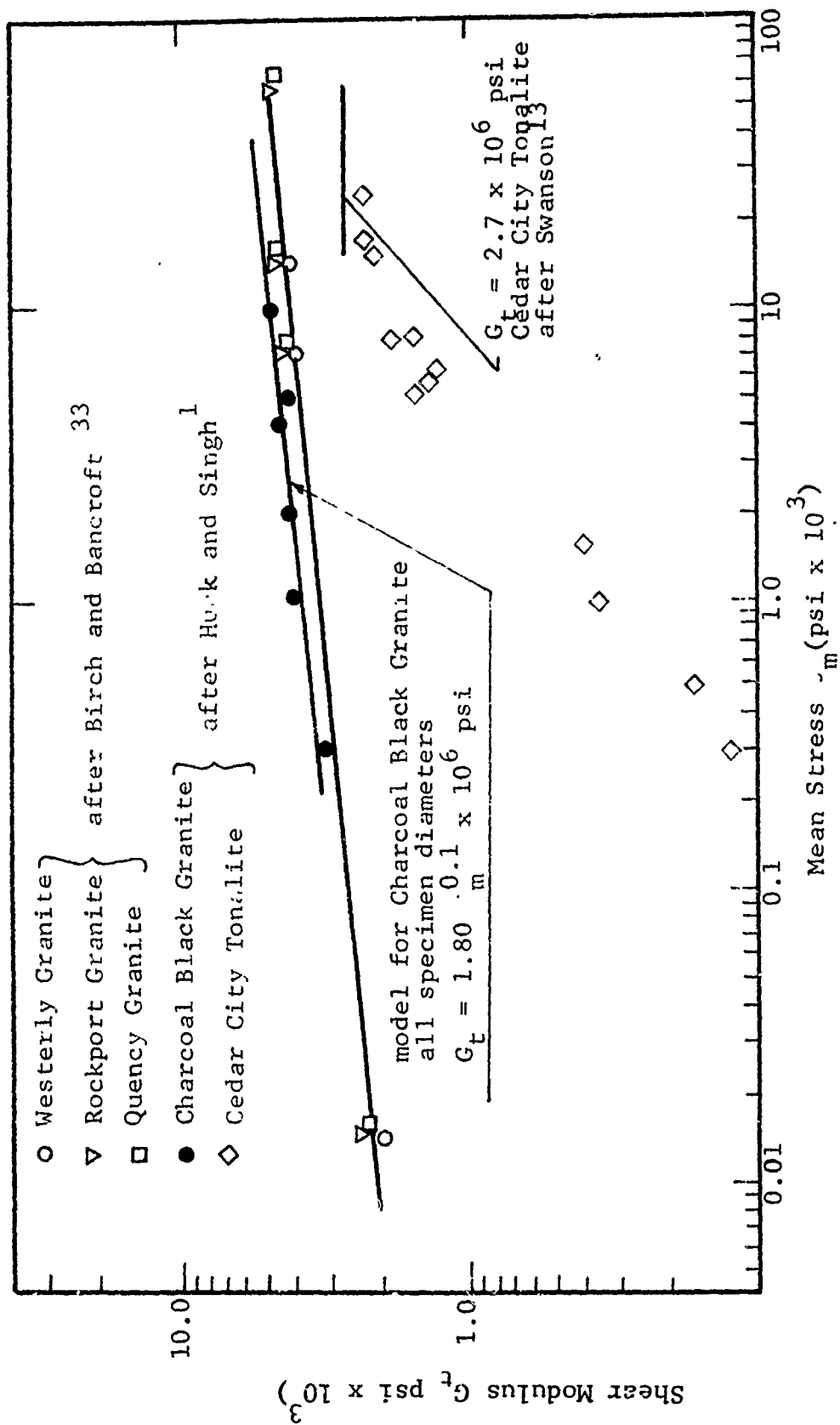


Fig. 16 VARIATION OF SHEAR MODULUS WITH MEAN STRESS

in which  $c$  is a constant.

#### 4.5 Poisson's Ratio and Young's Modulus

Two constants are necessary to describe the stress-strain behavior of an isotropic elastic material. One set of constants,  $k$  and  $G$ , which separate volumetric and deviatoric behavior have been described previously. Another pair of constants which are commonly used are Poisson's ratio,  $\nu$ , and Young's modulus,  $E$ . The constants  $E$  and  $\nu$  are derived directly from a triaxial test in which the lateral stresses,  $\sigma_2$  and  $\sigma_3$ , are equal to zero. For this special test condition.

$$E = \frac{\sigma_1}{\epsilon_1}, \text{ and} \quad (16)$$

$$\nu = - \frac{\epsilon_3}{\epsilon_1} \quad (17)$$

For more general test conditions

$$E = \frac{9kG}{3k + G}, \text{ and} \quad (18)$$

$$\nu = \frac{3k - 2G}{2(3k + G)}. \quad (19)$$

The use of tangent values of bulk and shear moduli,  $k_t$  and  $G_t$ , in equations (18) and (19) will result in tangent values for Poisson's ratio,  $\nu_t$ , and Young's modulus,  $E_t$ .

For hydrostatic loading the deviatoric stresses and strains are zero and  $G$  is undetermined. Therefore,  $E$  and  $\nu$  are also indeterminate from a hydrostat. For a triaxial test with  $\sigma_3$  equal to zero,  $E$  and  $\nu$  may be computed from (16) and (17). For a triaxial test with  $\sigma_3$  unequal to zero but constant, tangent values of  $E$  and  $\nu$  may be computed from

$$E_t = \frac{d\sigma_1}{d\epsilon_1}, \text{ and} \quad (32)$$

$$\nu_t = \frac{d\epsilon_3}{d\epsilon_1}. \quad (33)$$

## 4.6 Charcoal Black Granite

### 4.6.1 Hydrostatic Behavior

The hydrostatic stress-strain data for the Charcoal Black granite was fit to the nonlinear hysteretic model described by Seaman and Whitman.<sup>32</sup> The model parameters were determined by plotting log mean stress as a function of log volumetric strain. Recall that this model is given by

$$\sigma_m = A \varepsilon_v^n$$

The parameters A and n were computed for each size specimen, grouping the five tests at each size together. The values for A and n were used to compute the bulk modulus by using the transform

$$k_t = \frac{\partial \sigma_m}{\partial \varepsilon_v} = n A^{\frac{1}{n}} \sigma_m^{(n-1)/n}$$

where  $k_t$  is the tangent bulk modulus and the other quantities are as given above. The hydrostatic stress-strain behavior for the four specimen sizes is shown in Figs. 17 to 20, together with the models fit to each specimen size. The data from the 2-in. dia specimens fit the model closely at stress above about 2 ksi. This deviation is expected because the model predicts zero stiffness at zero pressure. The data from the 4-in. dia specimens appeared to be slightly stiffer than the 2-in. specimens, but the same model parameters provided a reasonable fit to the data. The 12-in. dia specimens were considerably stiffer than the smaller cores, and displayed less strain-hardening. The 32-in. dia specimens were similar in response to the 2- and 4-in. dia cores. The model for the two smaller sizes is also indicated with the model for the 32-in. dia cores in Figure 20 for comparison. The difference in the two models is not large, and reference to Figure 18 will show that the 4-in. dia data would fit either model equally well. The

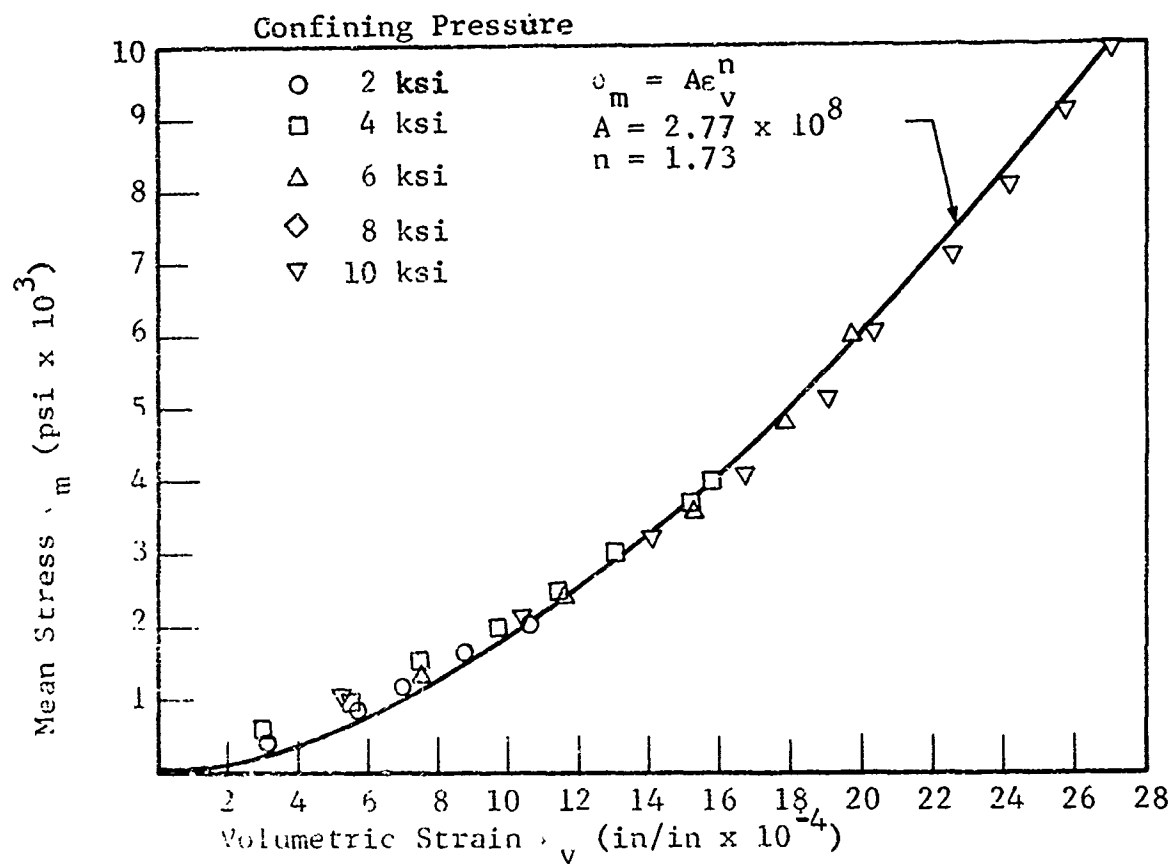


Fig. 17 MEAN STRESS vs. VOLUMETRIC STRAIN (2" GRANITE)

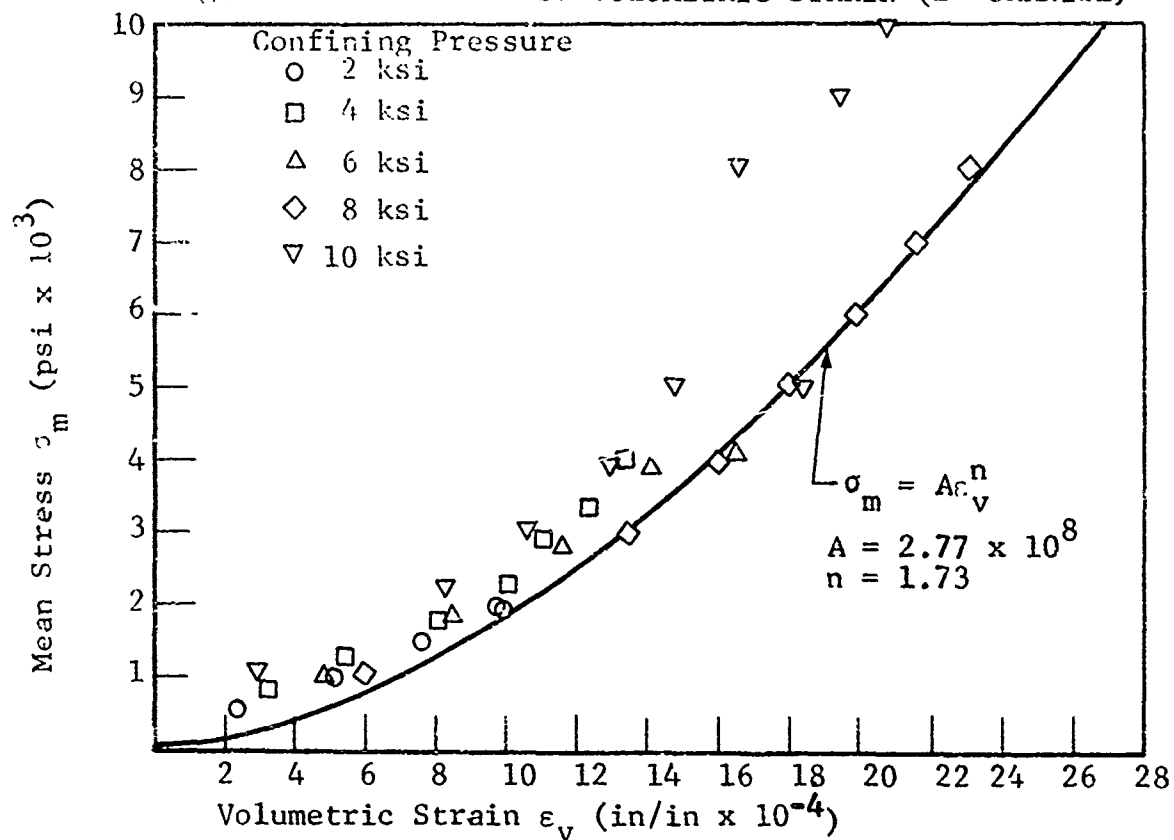


Fig. 18 MEAN STRESS vs. VOLUMETRIC STRAIN (4" GRANITE)



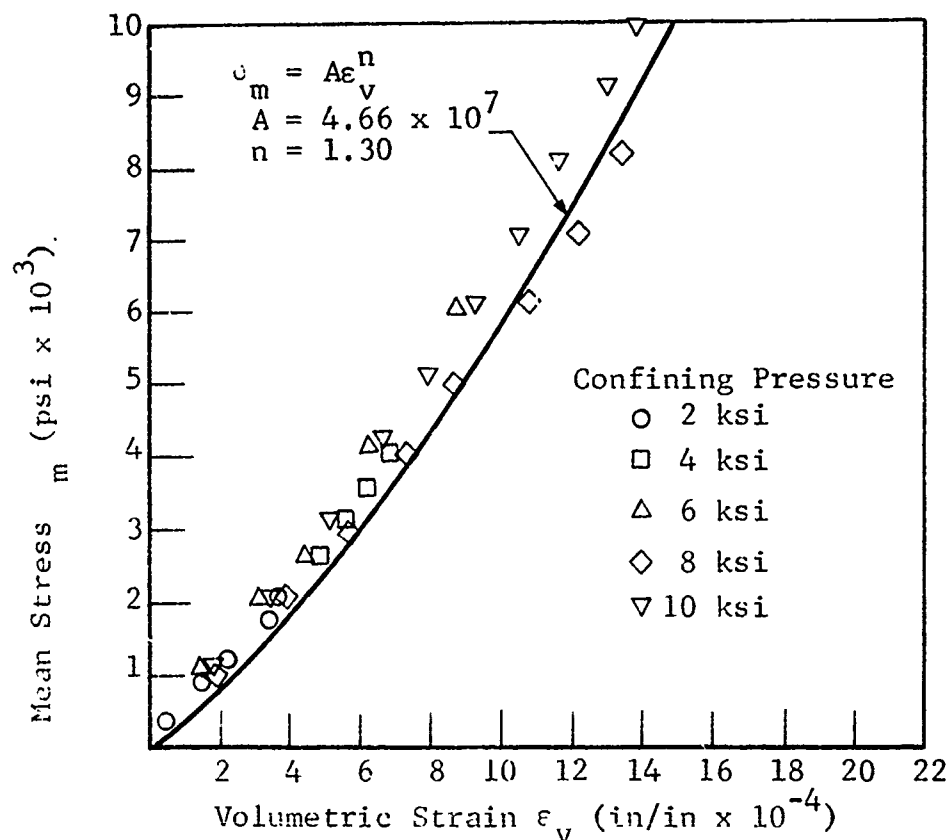


Fig. 19 MEAN STRESS vs. VOLUMETRIC STRAIN  
(12" GRANITE)

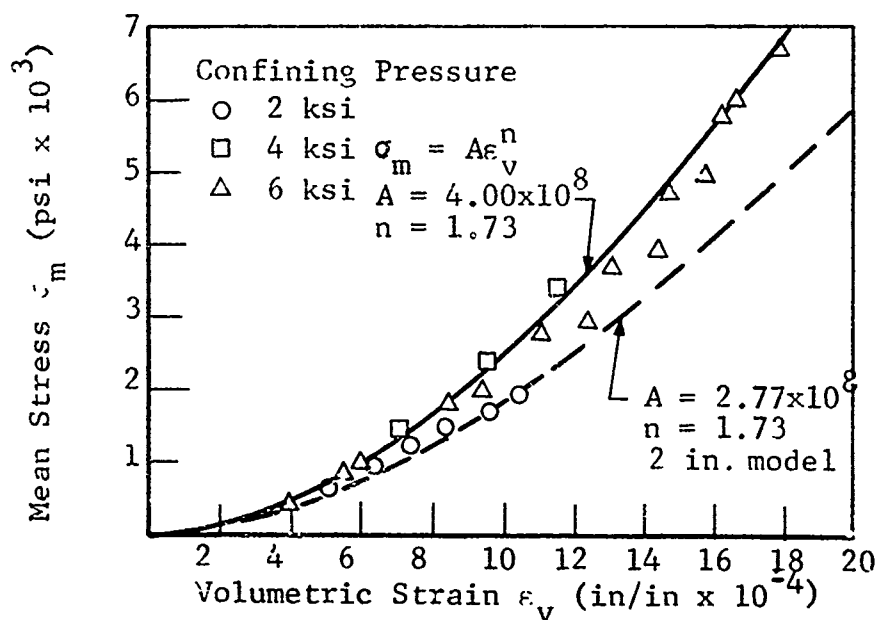


Fig. 20 MEAN STRESS vs. VOLUMETRIC STRAIN  
(32" GRANITE)

deviation of the 12-in. cores from the other three sizes may be explained by the fact that the 2- and 4- in. dia specimens were cored from a waste piece of 32-in. dia core. The 12-in. dia specimens were probably obtained from a different part of the quarry, and were found to display slightly different properties in the non-destructive tests. The fact of greater stiffness and less strain-hardening may indicate a relative lack of macroflaws in these specimens.

The tangent bulk modulus as predicted by the models and the observed values are shown in Figures 21 to 24. The model predictions fit the data well except at low stress levels. There is somewhat more scatter in this form of data presentation, as may be expected from the fact that the values represent differentiation of experimental data over short intervals. Finally, the derived models are compared in Figures 25 and 26. It appears that there is little effect of specimen size on the hydrostatic behavior of Charcoal Black granite. The greater stiffness of the 12-in. dia cores is probably caused by slightly different properties in the rock. This is confirmed by the non-destructive tests, which would not be expected to be influenced by specimen size.

#### 4.6.2 Triaxial Behavior

The triaxial behavior of the charcoal black granite is represented by a model used by Birch and Bancroft<sup>33</sup>.

$$G_t = c\sigma_m^{0.1}$$

in which

$G_t$  = tangent shear modulus

$\sigma_m$  = mean stress

$c$  = model parameter

The triaxial behavior for all sizes of the granite was represented by a single model, the data being shown in Figures 27 to 30. By following the data for an individual

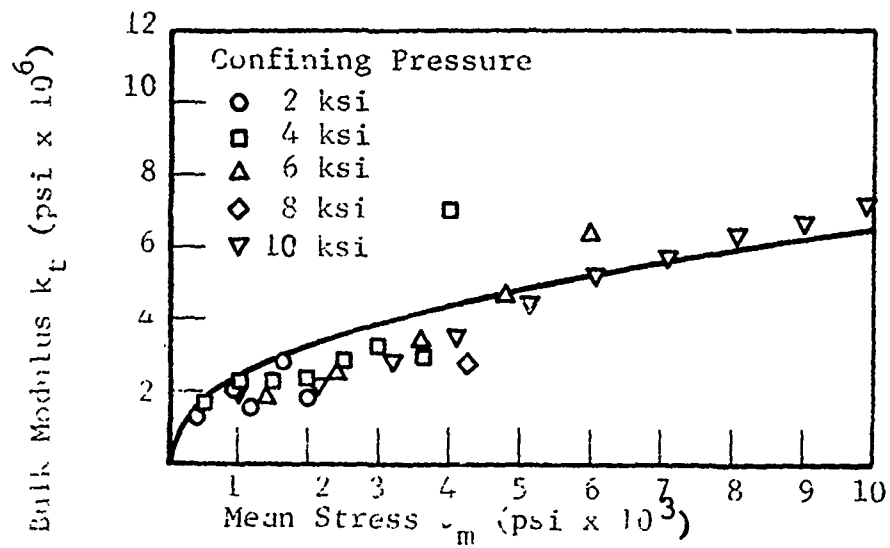


Fig. 21 BULK MODULUS FOR 2" GRANITE

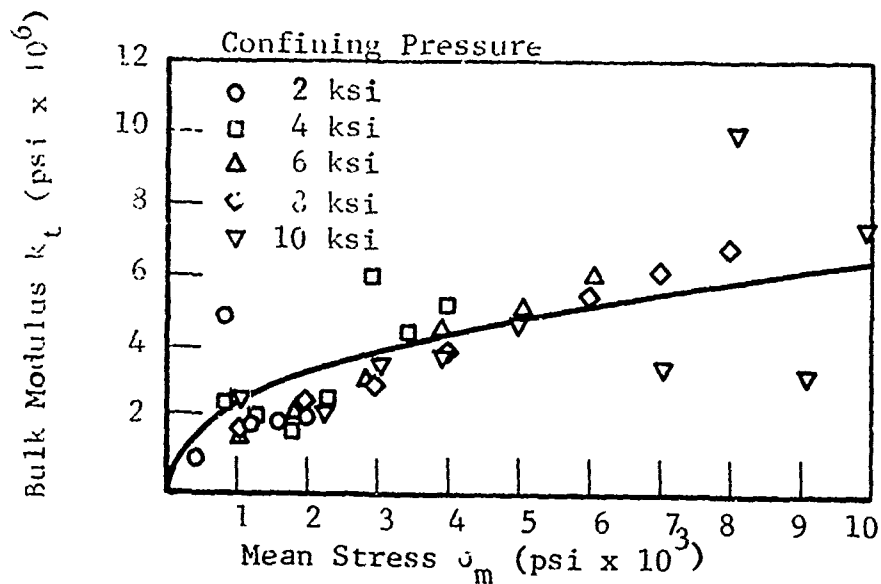


Fig. 22 BULK MODULUS FOR 4" GRANITE

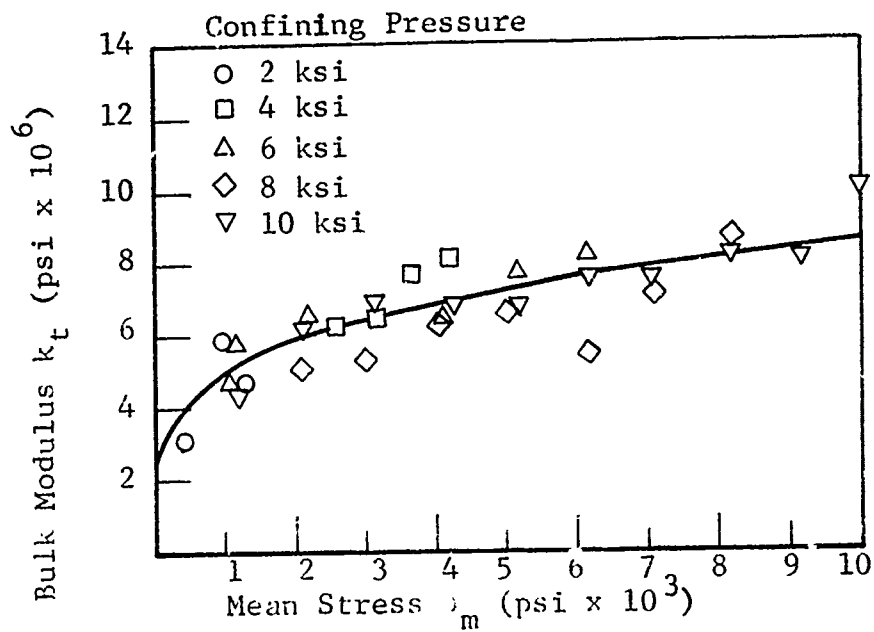


Fig. 23 BULK MODULUS FOR 12" GRANITE

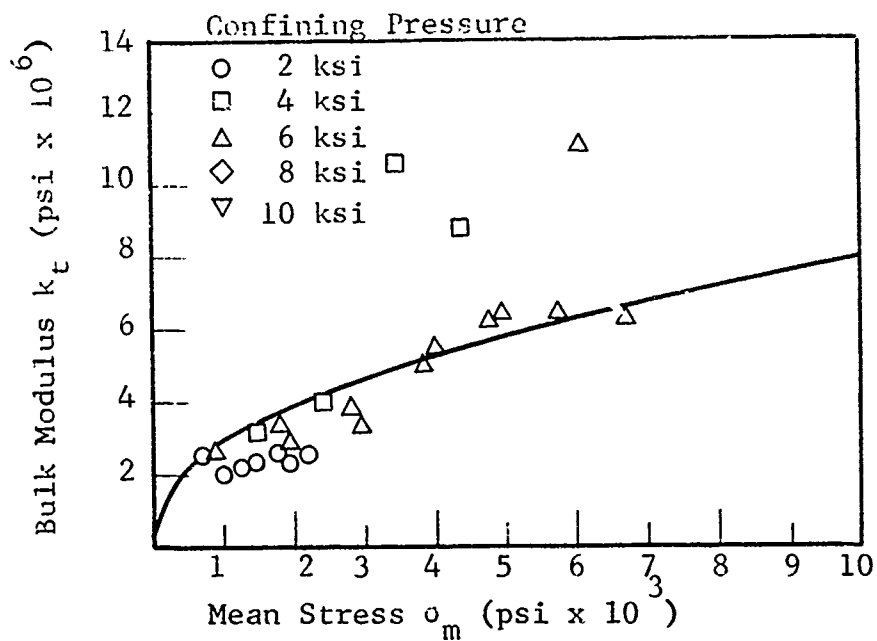


Fig. 24 BULK MODULUS FOR 32" GRANITE

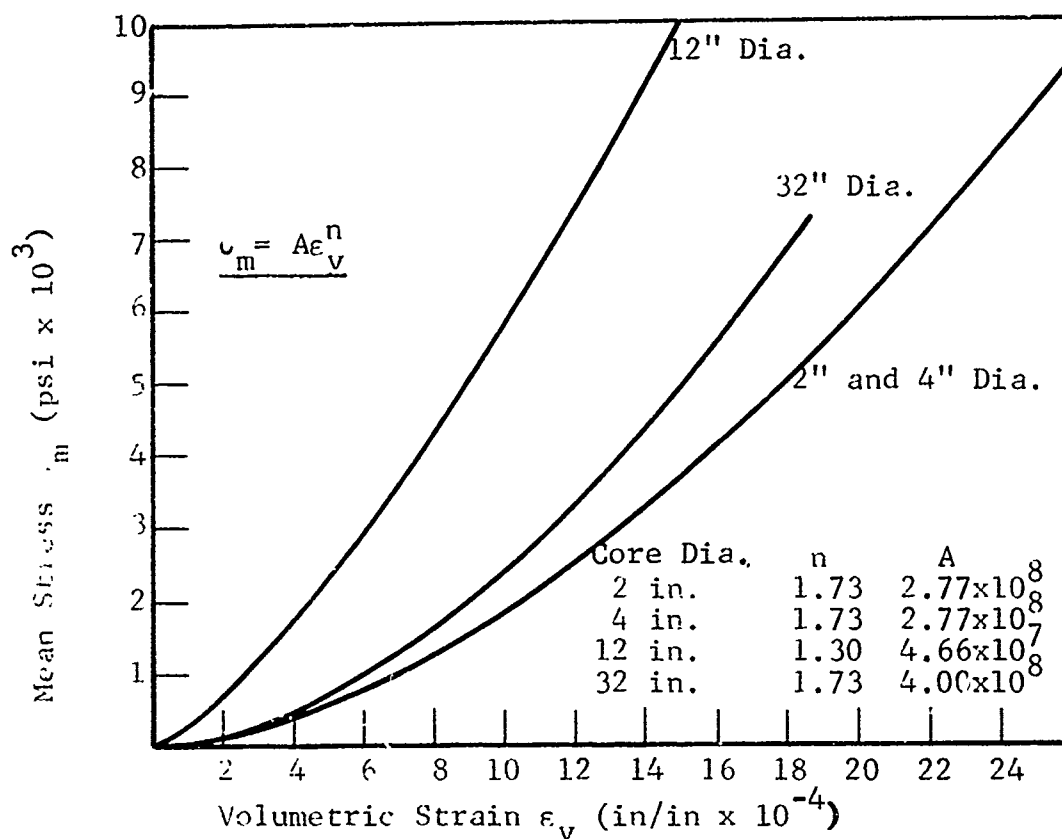


Fig. 25 MEAN STRESS vs. VOLUMETRIC STRAIN - GRANITE MODELS

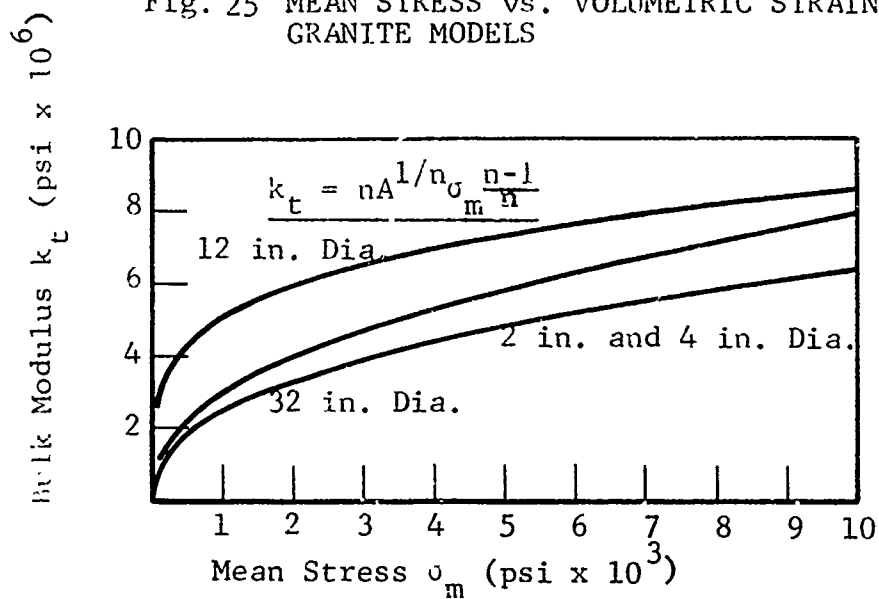


Fig. 26 BULK MODULUS vs. MEAN STRESS - GRANITE MODELS

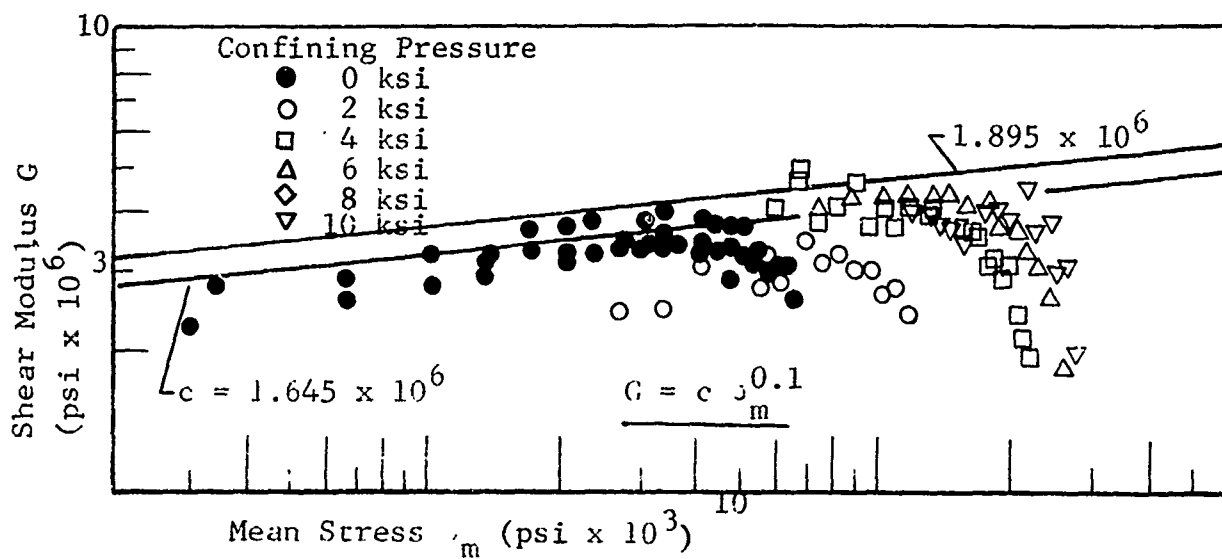


Fig. 27 SHEAR MODULUS vs. MEAN STRESS - 2 in. GRANITE

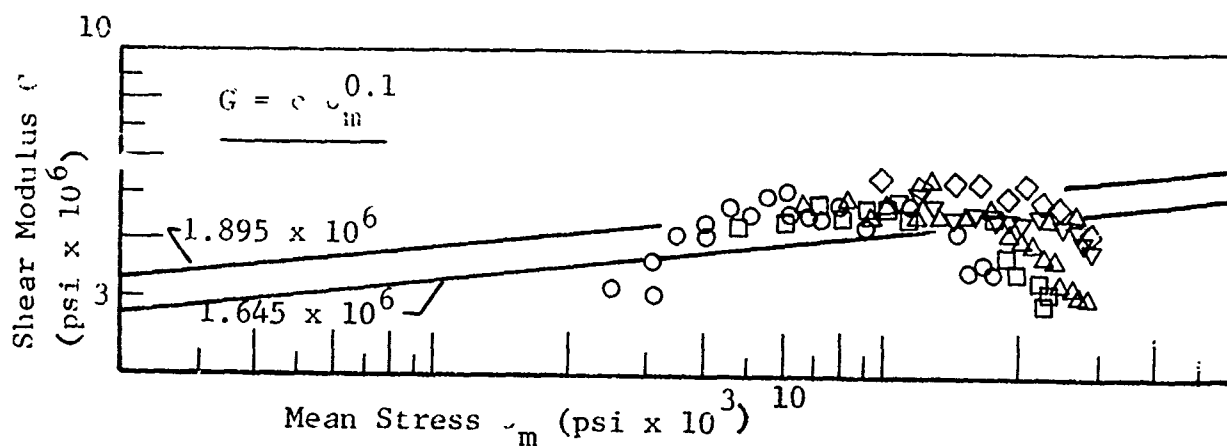


Fig. 28 SHEAR MODULUS vs. MEAN STRESS - 4 in. GRANITE

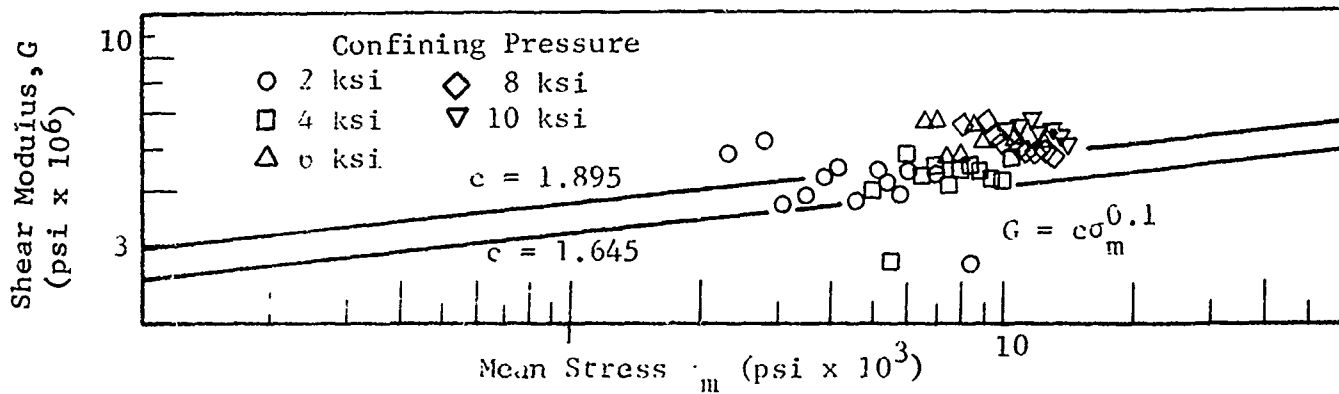


Fig. 29 SHEAR MODULUS VS. MEAN STRESS -12 IN. GRANITE

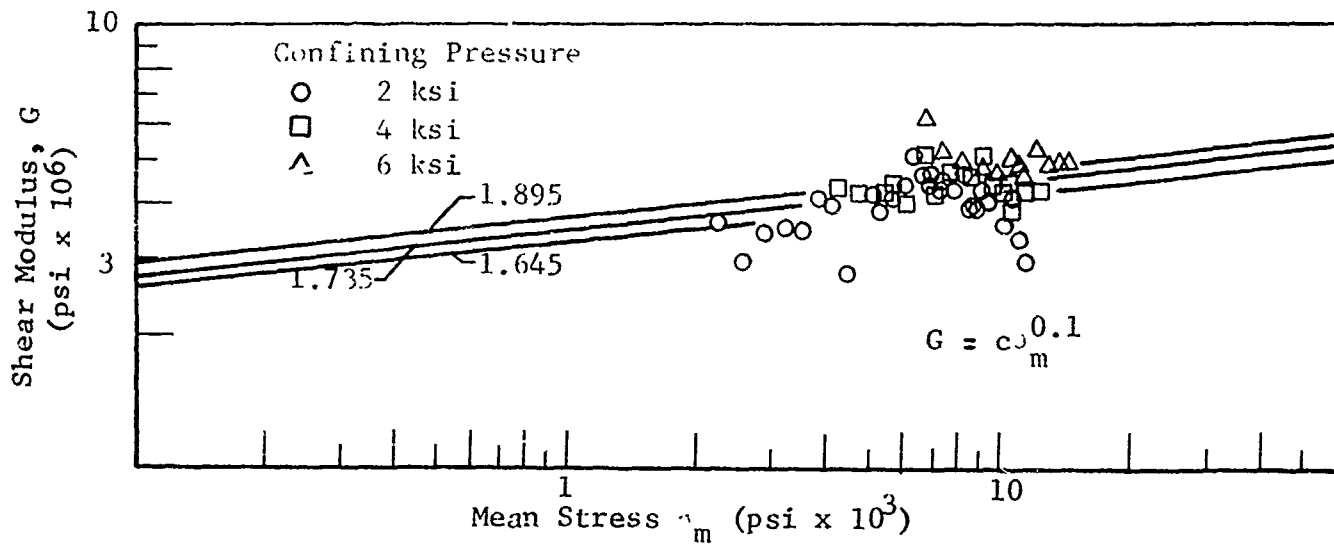


Fig. 30 SHEAR MODULUS VS. MEAN STRESS -32 IN. GRANITE

test, it can be seen that the shear modulus does increase with mean stress at intermediate stress levels. As yielding begins, the shear modulus decreases rapidly, deviating from the model. Inspection of Figure 27, in which the effect shows most clearly, reveals that the point at which yielding occurs is higher for the tests at higher confining stress, exactly as would be expected.

#### 4.6.3 Young's Modulus and Poisson's Ratio

The values of shear and bulk moduli derived from their respective models may be employed to predict values for other elastic moduli. This was done for Poisson's ratio and the elastic modulus, using the relationships given in Eq. (18) and (19) on page 43.

$$E = \frac{kG}{3k+G} \quad \text{and} \quad \nu = \frac{3k-2G}{2(3k+G)}$$

in which  $E$  = Young's modulus

$\nu$  = Poisson's ratio

$k$  = bulk modulus

$G$  = shear modulus

The predicted values for the elastic modulus are shown in Figures 31 to 34, together with the observed values. The agreement is good at low and intermediate stress levels. At higher stresses, yielding begins, reducing the observed stiffness.

Predicted and observed values for Poisson's ratio are displayed in Figures 35 to 38. Inspection reveals that the trends predicted by the model are present, but the values predicted are lower in some cases than the observed values. The model is fallacious at low stress levels, where the low predicted bulk moduli act significantly. As yielding occurs, Poisson's ratio increases due to dilational effects, resulting in values greater than 0.5. Yielding occurs at higher stress levels on the tests at higher confining pressures. The



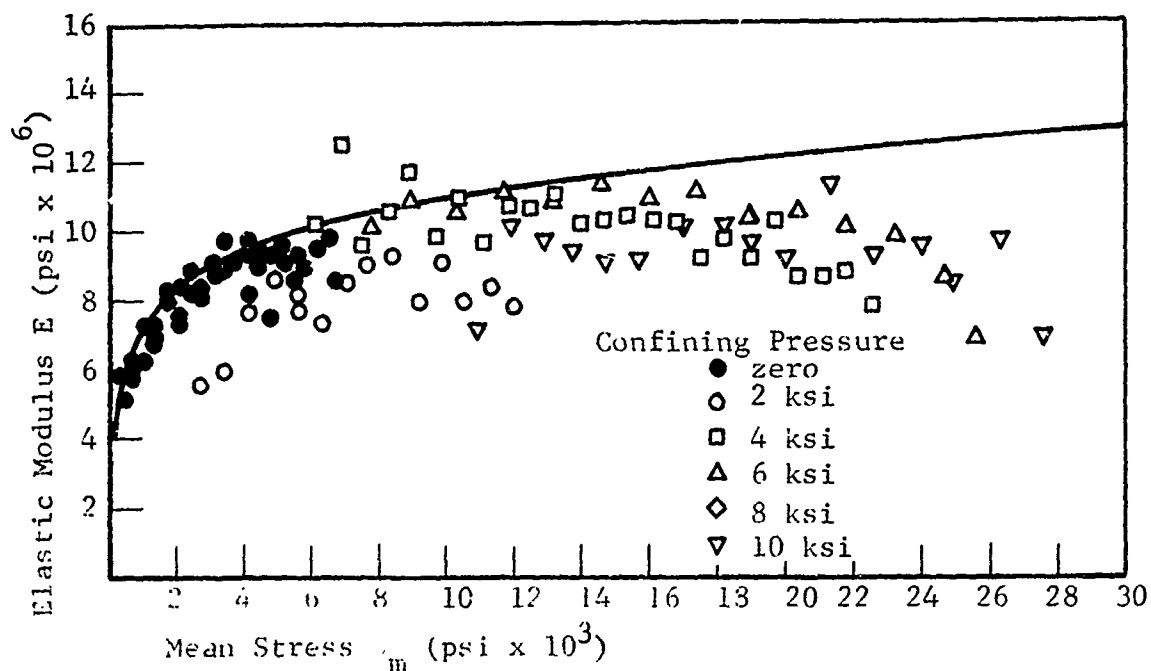


Fig. 31 ELASTIC MODULUS FOR 2" GRANITE

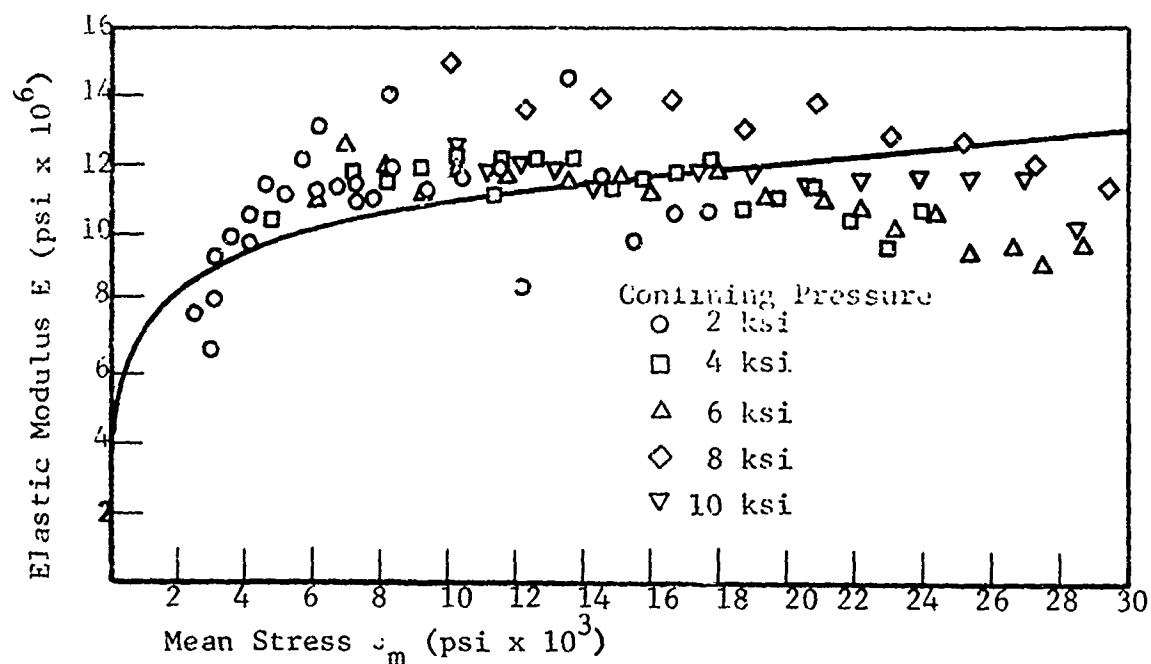


Fig. 32 ELASTIC MODULUS FOR 4" GRANITE

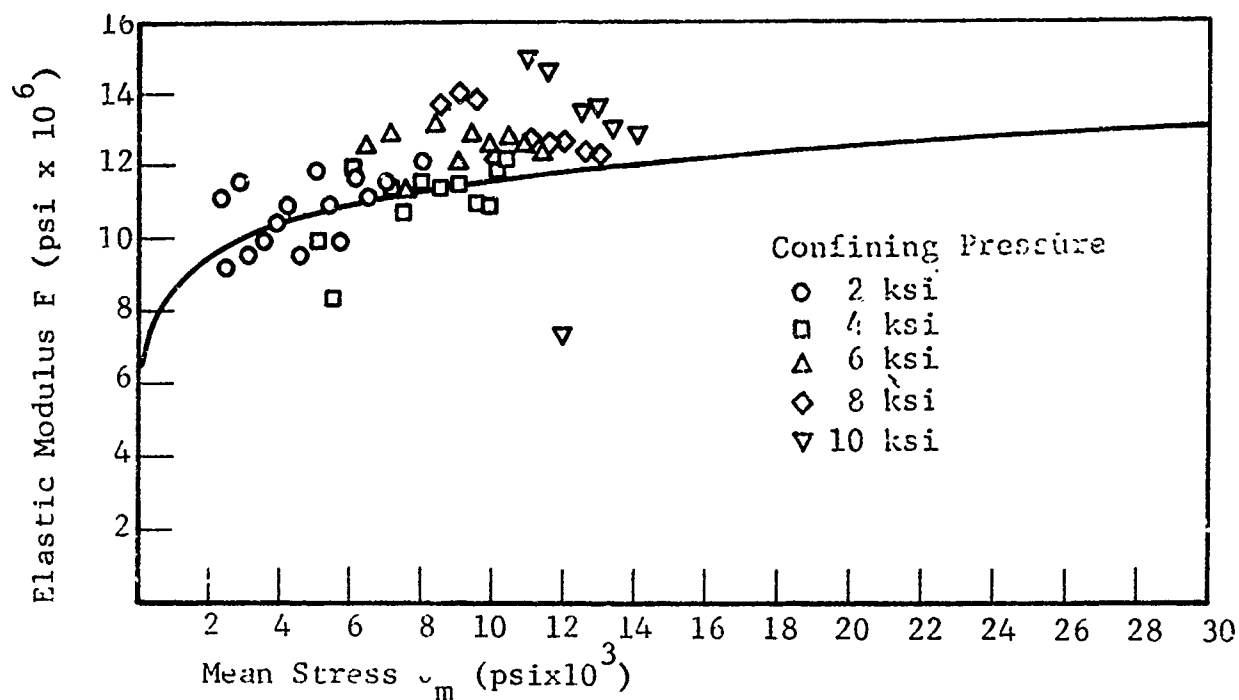


Fig. 33 ELASTIC MODULUS vs. MEAN STRESS - 12" GRANITE

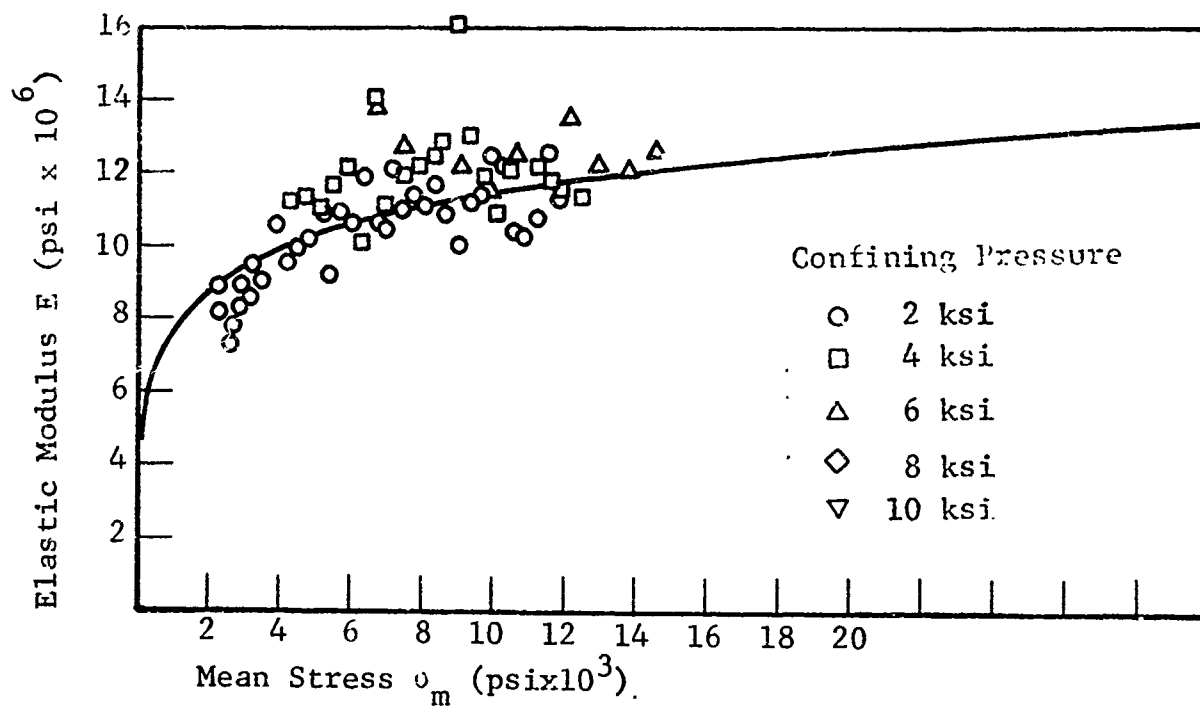


Fig. 3' ELASTIC MODULUS vs. MEAN STRESS - 32" GRANITE

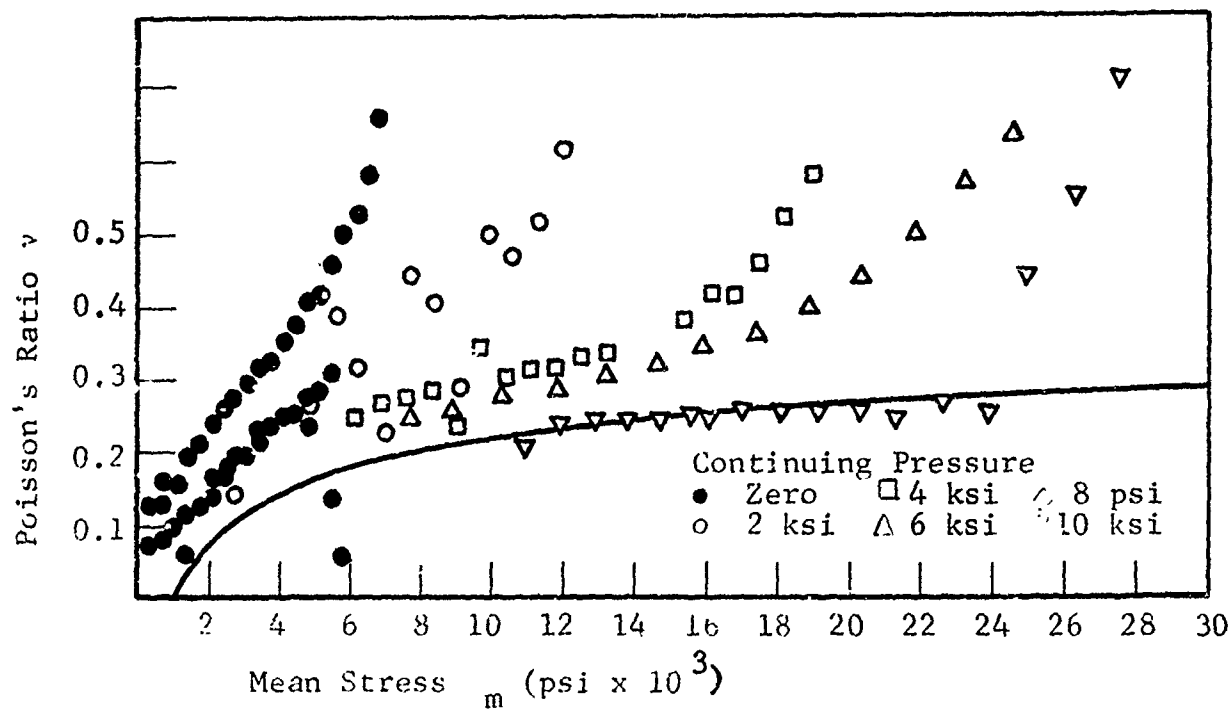


Fig. 35 POISSON'S RATIO FOR 2 in. GRANITE

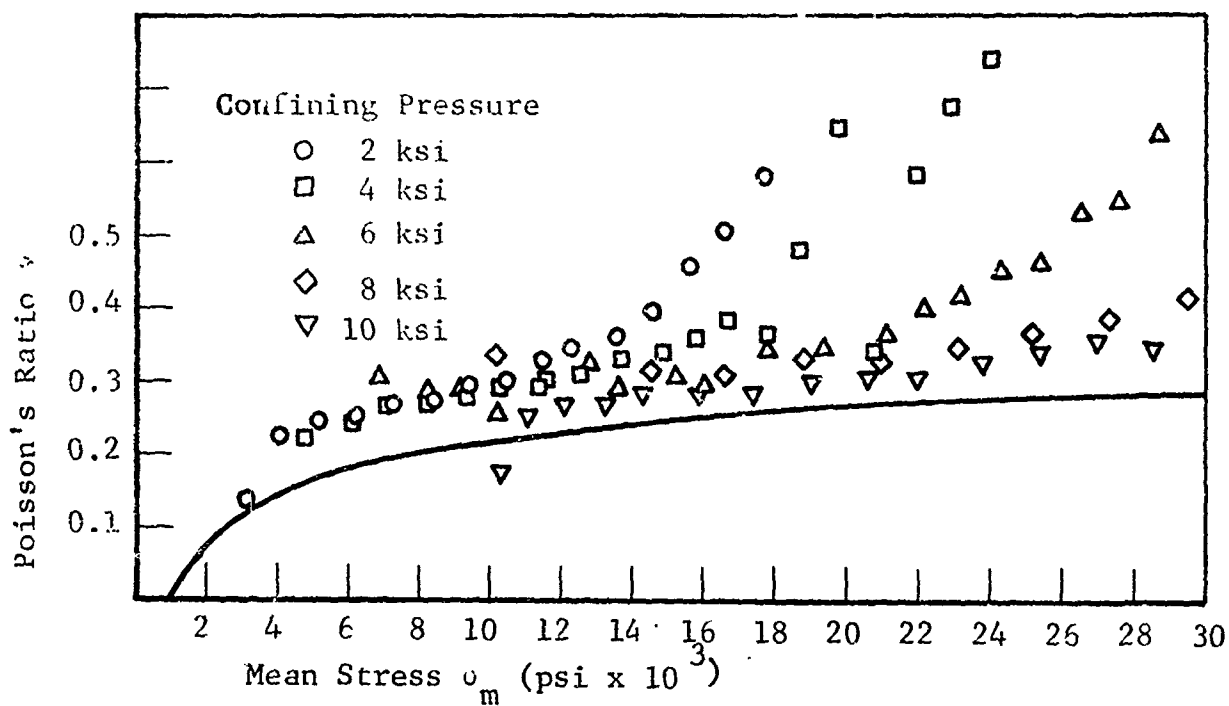


Fig. 36 POISSON'S RATIO FOR 4 in. GRANITE

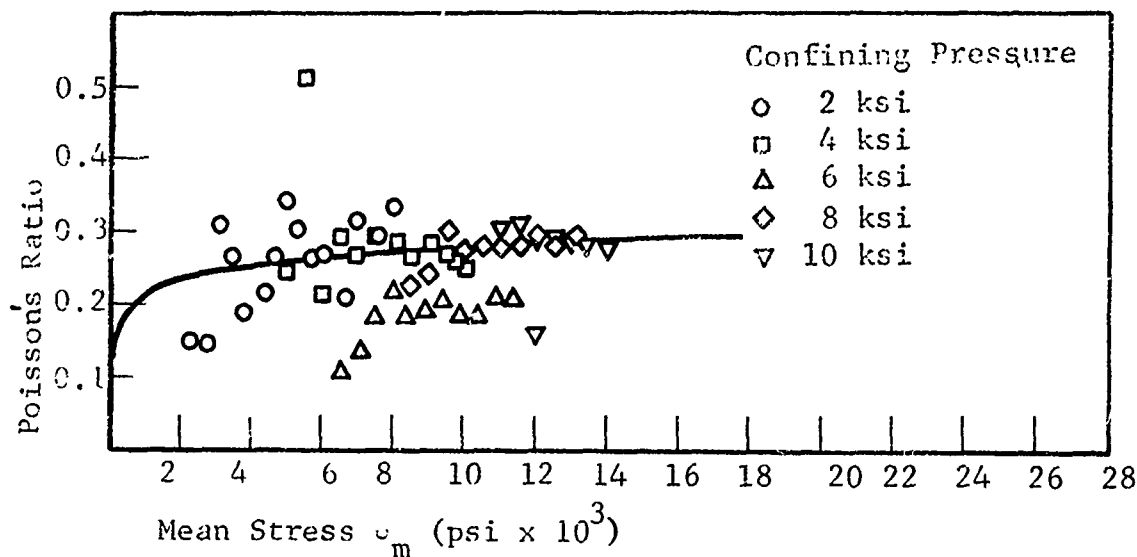


Fig. 37 POISSON'S RATIO FOR 12"  $\emptyset$  GRANITE

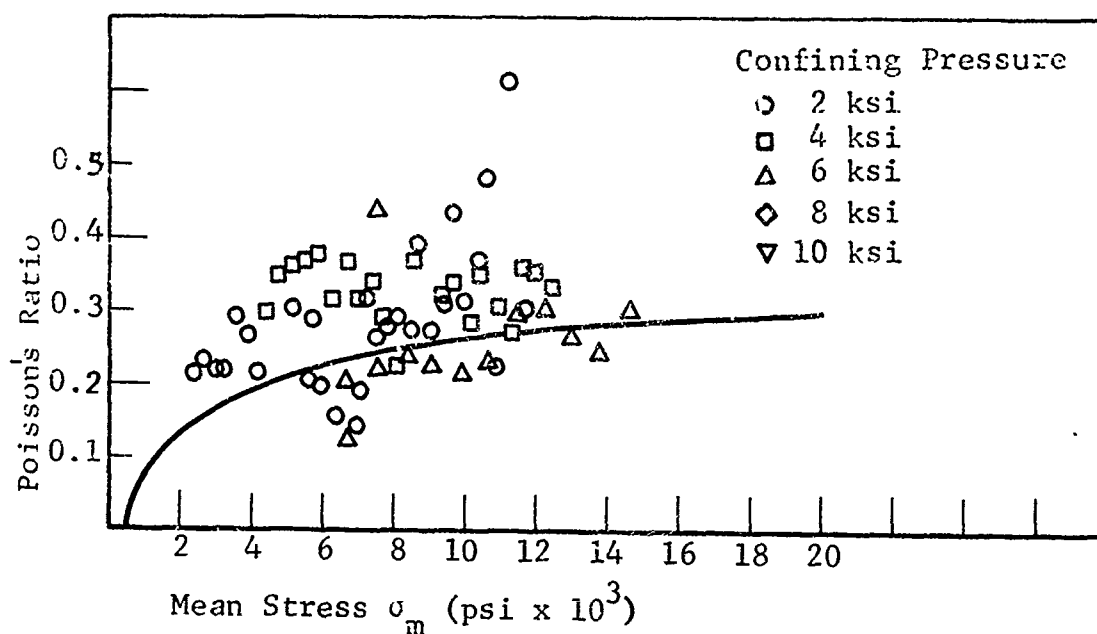


Fig. 38 POISSON'S RATIO FOR 32"  $\emptyset$  GRANITE

unconfined tests shown in Fig. 35 begin yielding at a mean stress of 2 or 3 ksi (axial stress of 6 or 9 ksi), while the test at  $\sigma_3 = 10$  ksi did not yield until it reached a mean stress of 23 ksi ( $\sigma_1 = 49$  ksi). The larger specimens behaved in a more or less similar manner, with little influence of specimen size.

#### 4.7 Indiana Limestone

##### 4.7.1 Hydrostatic Behavior

The limestone typically displayed a strain-softening behavior under hydrostatic loading. The mean stress vs. volumetric strain data were fit to the nonlinear hysteretic model with no significant variations attributable to specimen size. The data from most tests scatter about the curve given by the parameters below.

$$\sigma_m = A \varepsilon_v^n$$

$$A = 0.490 \times 10^6$$

$$n = 0.75$$

Note that for  $n$  less than one, the model is concave toward the strain axis. The data for all tests are shown in Figure 39. The model for bulk modulus derived for these parameters is shown in Figure 40, together with the observed data. The bulk modulus is given by

$$k_t = n A^{n-1} \sigma_m^{(n-1)/n}$$

in which  $A$  and  $n$  have the values given above. This model predicts a very high modulus at low stress levels, which is not the case in the real material. The actual data appear to have slight maxima in the area of 2 ksi, and then decay along the curve given by the model.

##### 4.7.2 Triaxial Behavior

The behavior of the Indiana limestone did not correspond to the one-tenth mean stress model. The triaxial data for all

IIT RESEARCH INSTITUTE

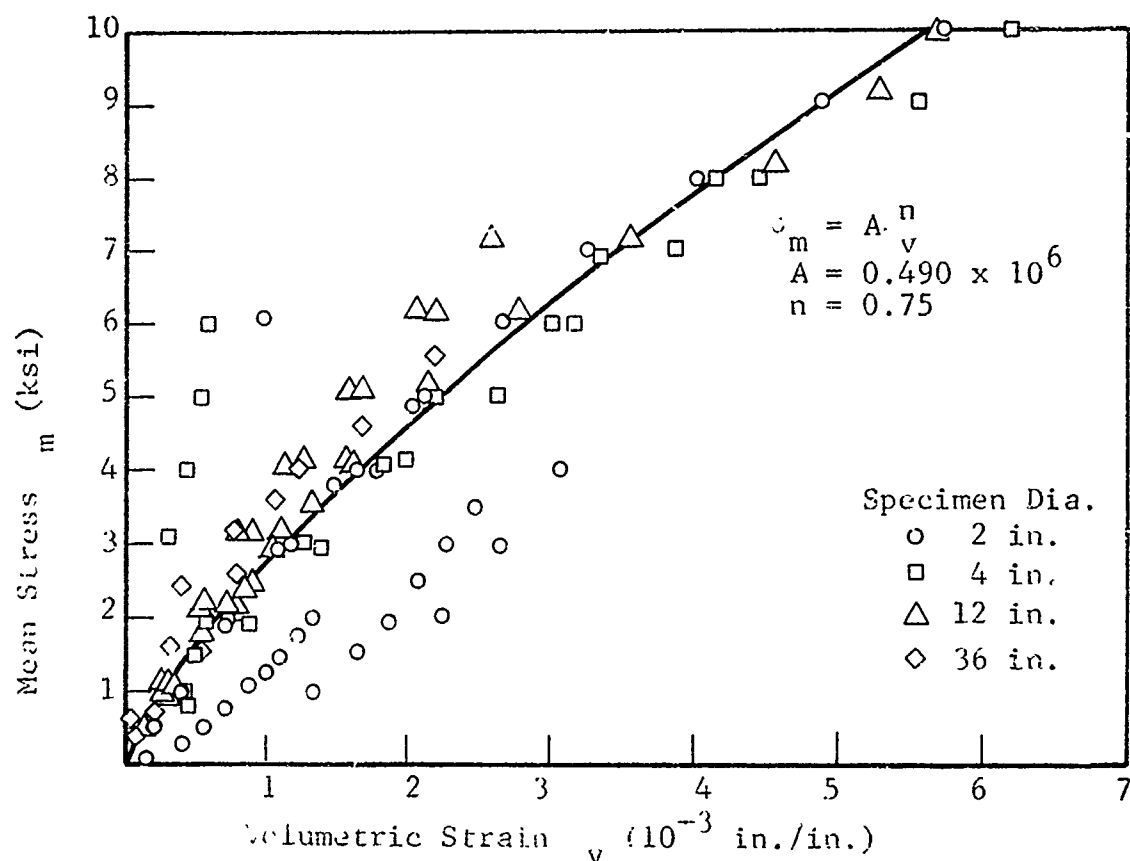


Fig. 39 MEAN STRESS vs. VOLUMETRIC STRAIN FOR ALL LIMESTONE

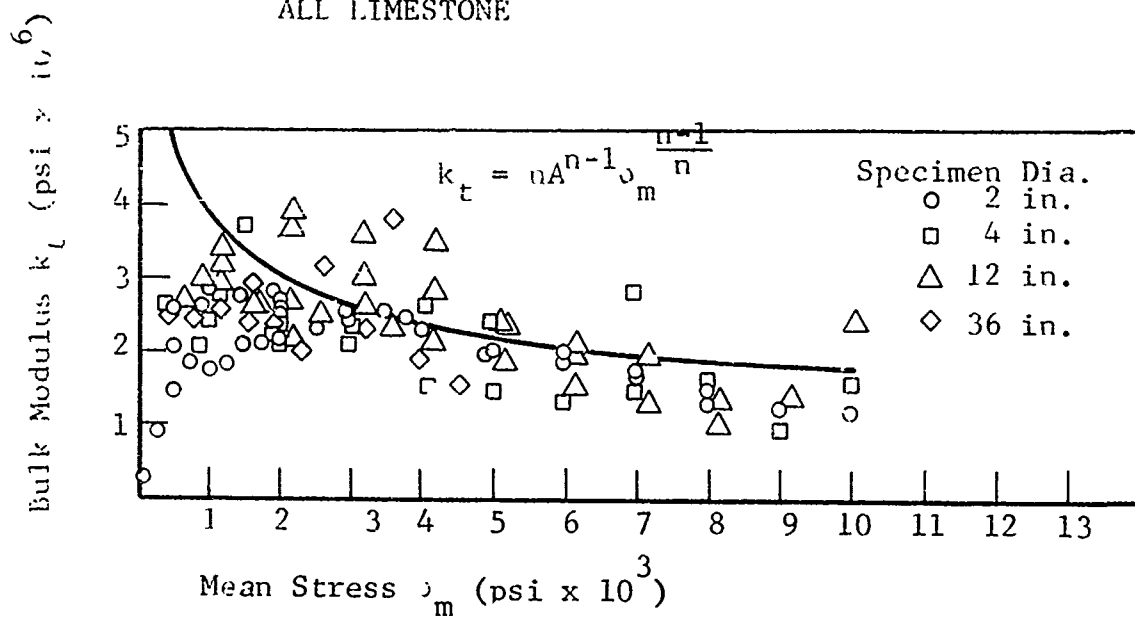


Fig. 40 BULK MODULUS FOR ALL LIMESTONE

Indiana limestone tests were plotted in the form:

$$\Delta\sigma = f(\Delta\epsilon)$$

$$\Delta\sigma = \text{deviator stress } \sigma_1 - \sigma_3$$

$$\Delta\epsilon = \text{shear strain } \epsilon_1 - \epsilon_3$$

This is shown in Figure 41, and it can be seen that the data are bounded by the line  $\Delta\sigma = 3.55 \times 10^6 (\Delta\epsilon)^{0.3}$ . At very low and very high stress levels the measured strains are larger than would be predicted from the model. The shear modulus,  $G_t$ , for all tests is shown in Figure 42 as a function of shear strain. The actual moduli are nearly constant at shear strains less than 500 microstrains. As the shear strain increases, the shear modulus drop uniformly until yielding occurs. Above the yield point the modulus drops rapidly. This behavior is indicated by the solid symbols on Figure 42, which are the trajectory followed by test 38, a 12-in. dia specimen at 6000 psi confining stress. The model generated by Figure 41 can be transformed to yield the tangent shear modulus. This is indicated on Figure 42. It can be seen that the model represents the shear modulus behavior of intermediate strain levels.

The model  $\Delta\sigma = B (\Delta\epsilon)^r$  can also be transformed to express shear modulus as a function of deviator stress. This transform, together with the measured data are shown in Figure 43. The data follow the model at intermediate stresses, but roll off at low stress levels and above yield.

#### 4.7.3 Young's Modulus and Poisson's Ratio

In order to consider the elastic modulus and Poisson's ratio, the models for shear modulus and bulk modulus are combined to produce  $E$  and  $\nu$  values for comparison with the observed quantities. In the case of the shear modulus model, the deviation from the model is extreme at low deviator stresses. The shear moduli represented by the curved line in Figure 43 would better account for this roll-off. The models produced

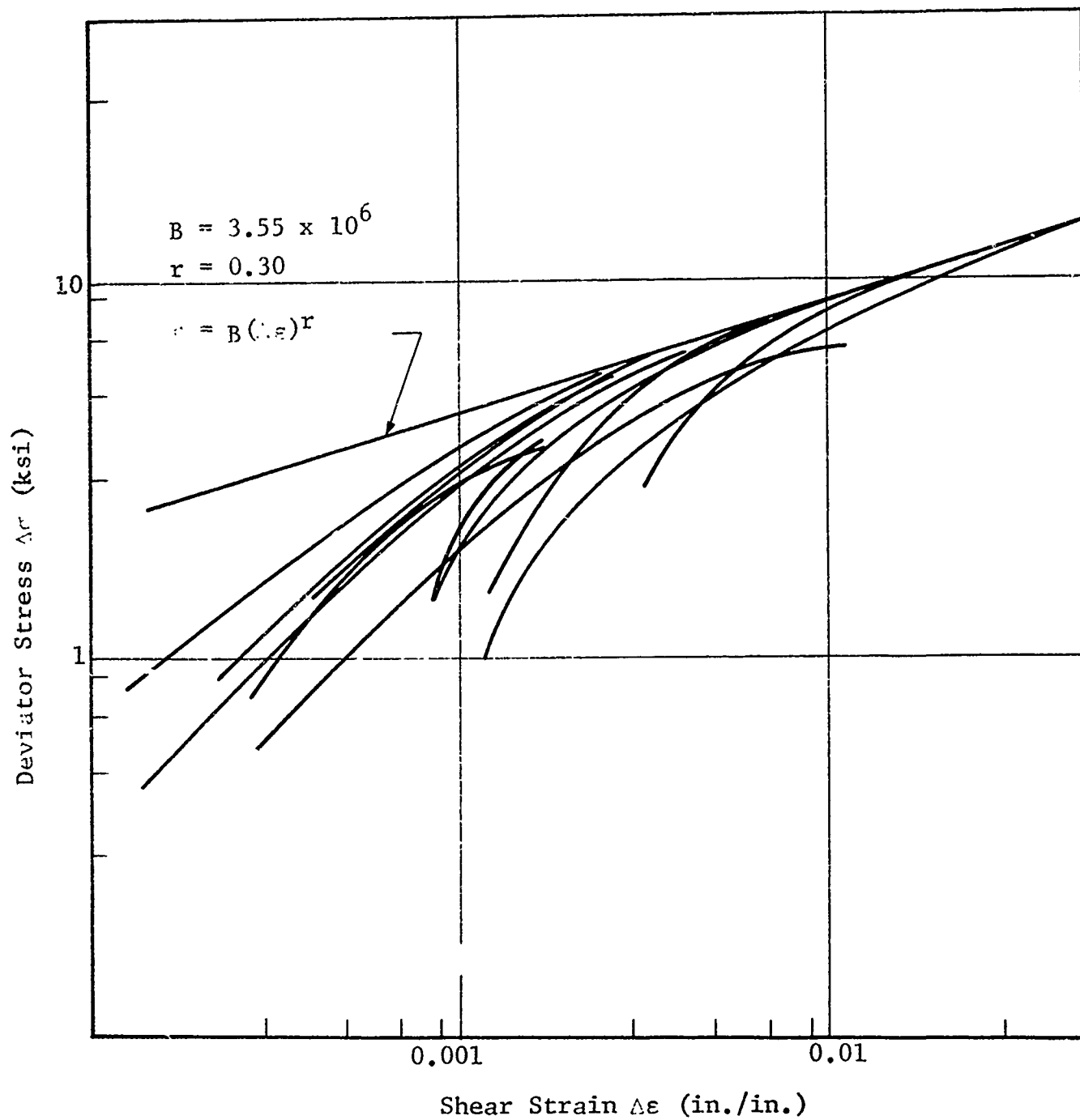


Fig. 41 SHEAR STRESS VS. SHEAR STRAIN FOR LIMESTONE



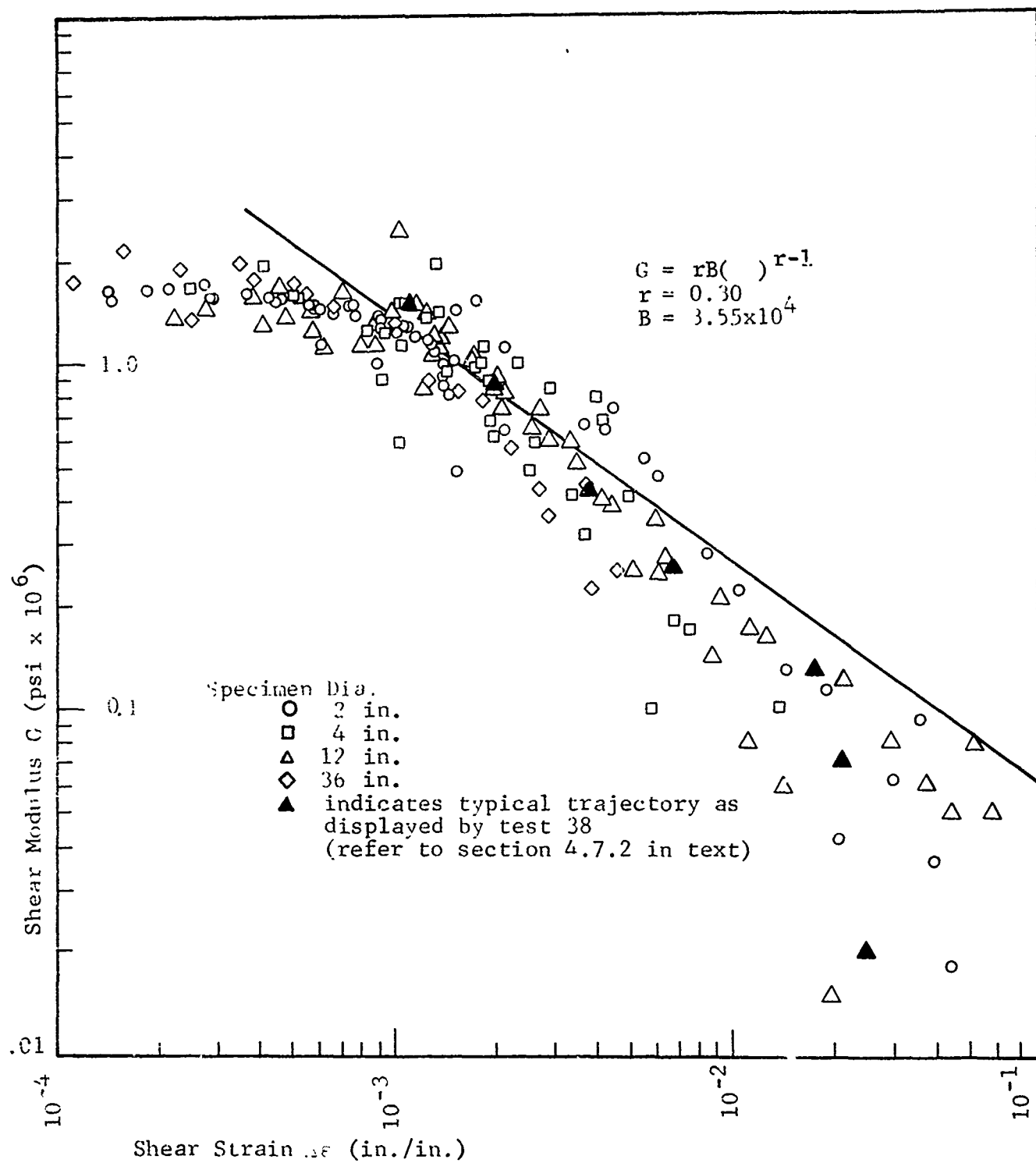


Fig. 42 SHEAR MODULUS vs. SHEAR STRAIN FOR ALL LIMESTONE

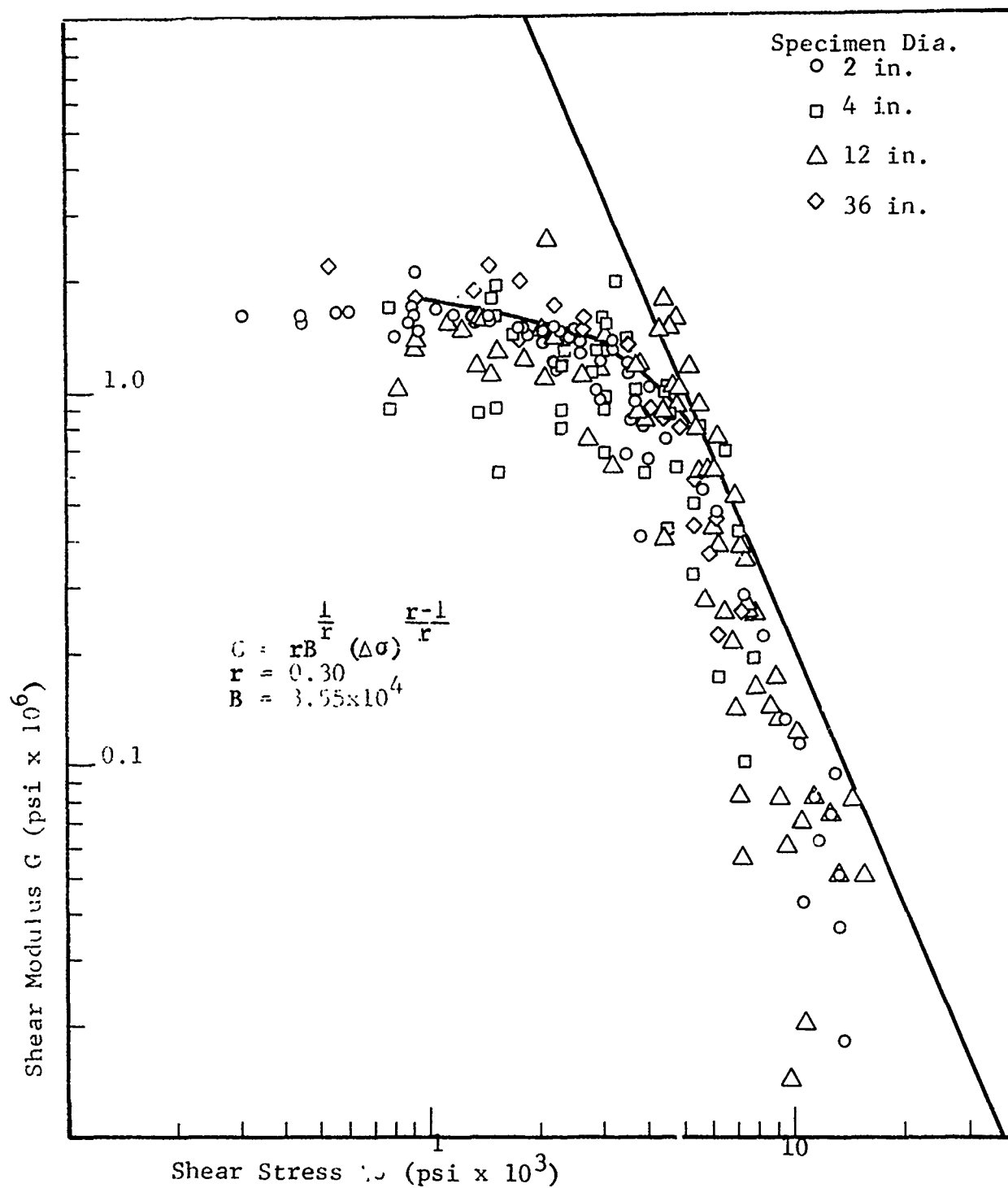


Fig. 43 SHEAR MODULUS vs. SHEAR STRESS FOR ALL LIMESTONE

for elastic moduli are shown in Figure 44 as a function of mean stress. The dashed lines indicate the change in the models that result from the use of the curved line in Figure 43 . The data for each level of confining stress are compared with these models in Figures 44 through 49 . As in the case of the shear model, which established an upper limit for the shear moduli, the observed elastic moduli are also bounded by the model. The material is reasonably well represented at intermediate stress levels, but is softer than indicated by the model at both low and high stresses.

In like fashion, Poisson's ratio models are shown in Figure 50 and the data at each confining stress in Figures 51 through 55 . These data are less consistent, and about all that can be said is that both the models and the data increase with mean stress.

In discussing the elastic modulus and Poisson's ratio, it should be remembered that the models for these properties were derived using the bulk modulus model, which was fit to the hydrostatic data only. The models for  $G$ ,  $E$ , and  $\nu$  can be applied uniquely only to the triaxial data.

#### 4.8 Strength Properties

The strength of a rock is typically displayed by plotting the locus of failure points as a function of the loading conditions. The failure data for Charcoal Black granite and Indiana limestone are shown on Figures 56 A and 56 B as functions of mean stress and  $J_2$ .

##### 4.8.1 Charcoal Black Granite

Sufficient data now exists to produce a failure curve for the small granite specimens. The 2-in. and 4-in. dia cores scatter about the curve indicated in Figure 56A , with no indication of any influence due to size in this range. These cores all failed catastrophically, with no indication of slippage along joints or weakness planes prior to failure.

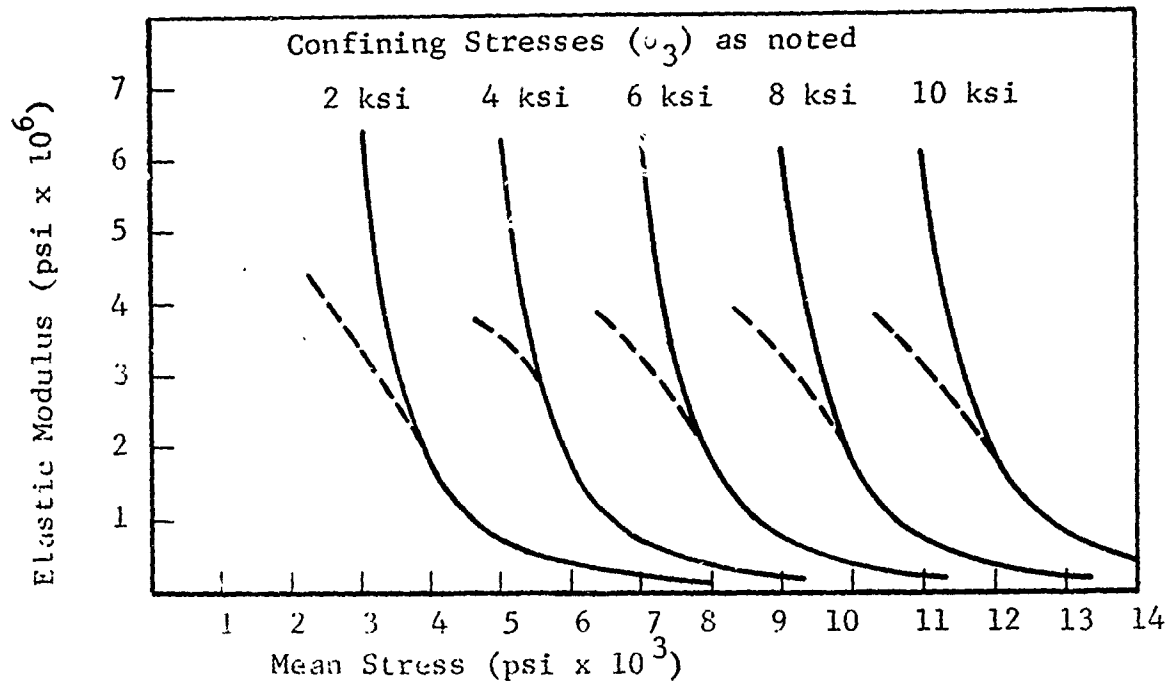


Fig. 44 ELASTIC MODULUS MODELS FOR INDIANA LIMESTONE

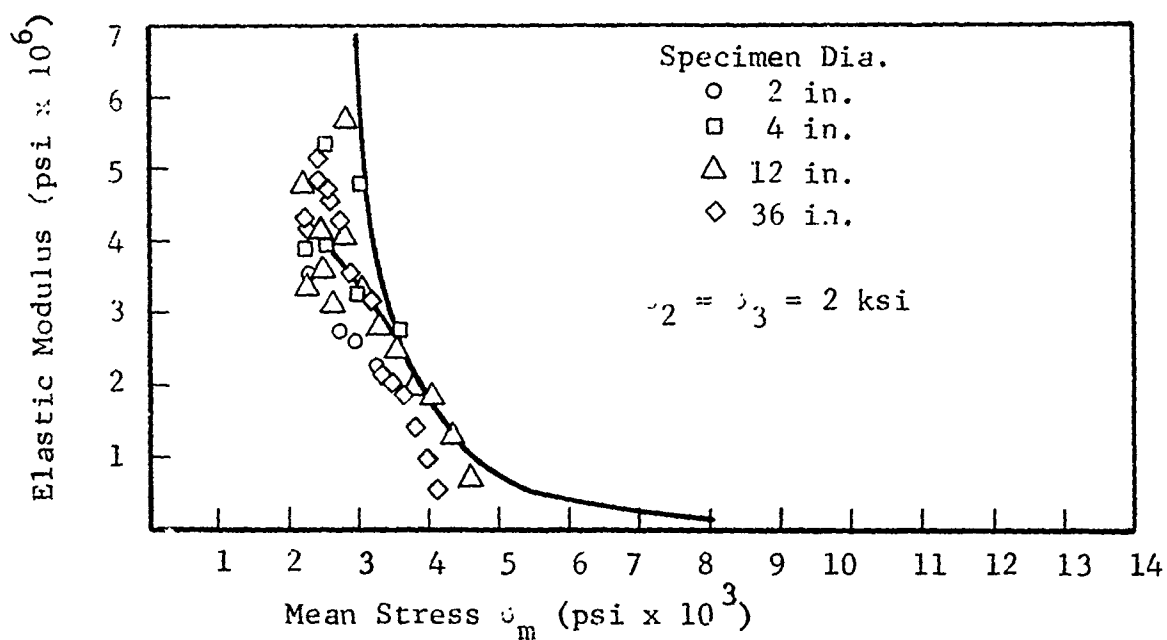


Fig. 45 ELASTIC MODULUS FOR INDIANA LIMESTONE ( $\sigma_3=2 \text{ ksi}$ )

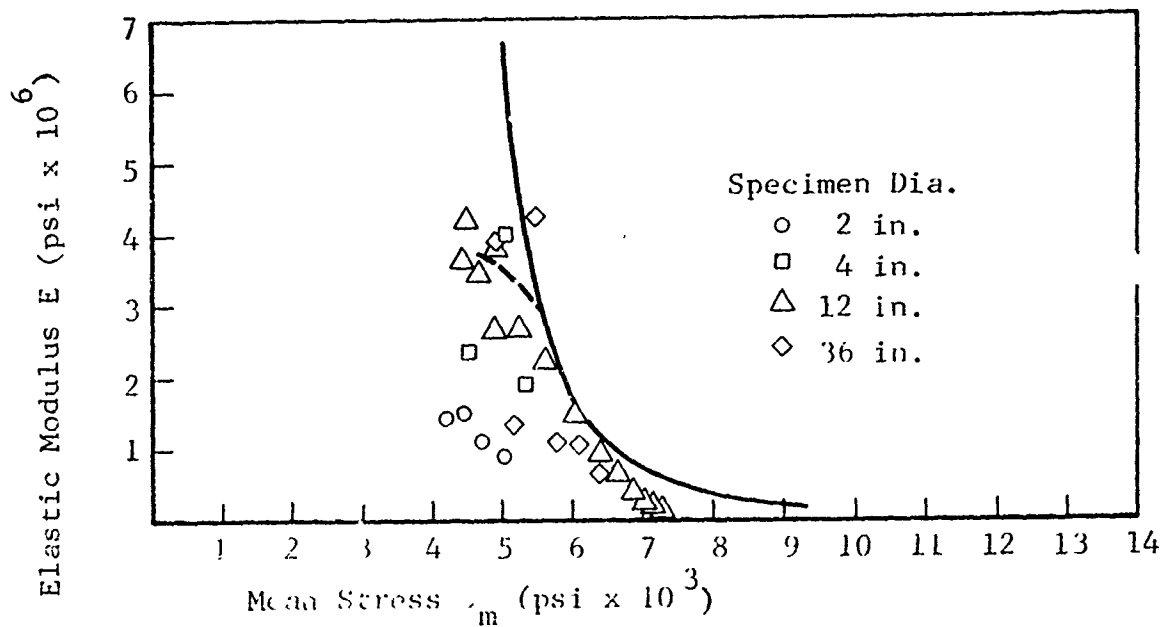


Fig. 46 ELASTIC MODULUS FOR INDIANA LIMESTONE ( $\sigma_3 = 4$  ksi)

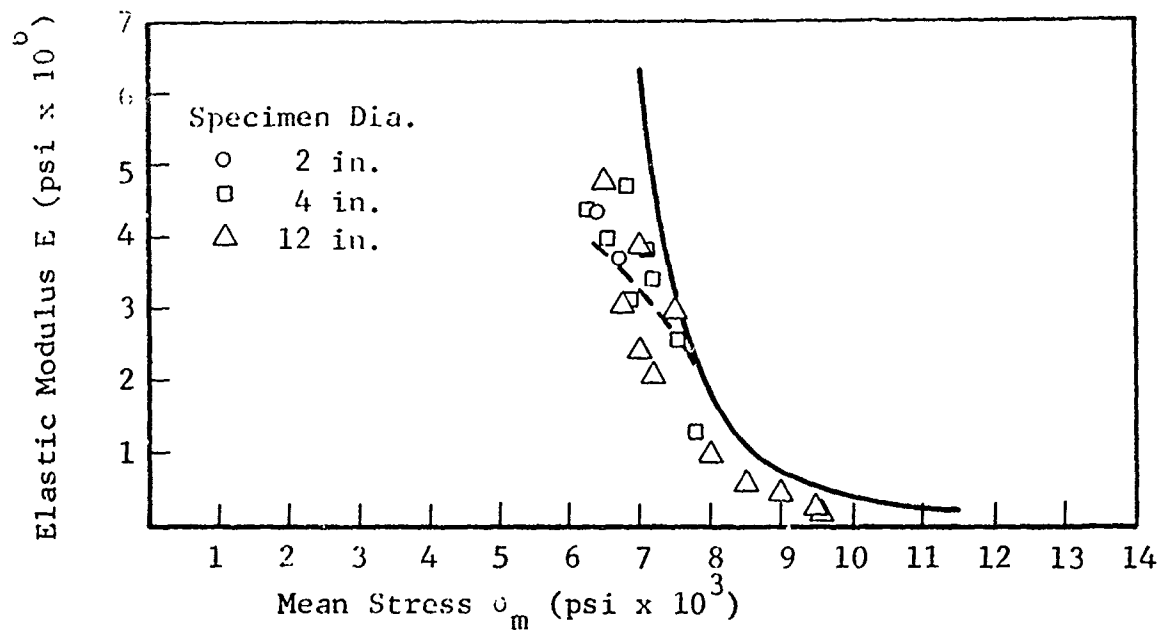


Fig. 47 ELASTIC MODULUS FOR INDIANA LIMESTONE ( $\sigma_3 = 6$  ksi)

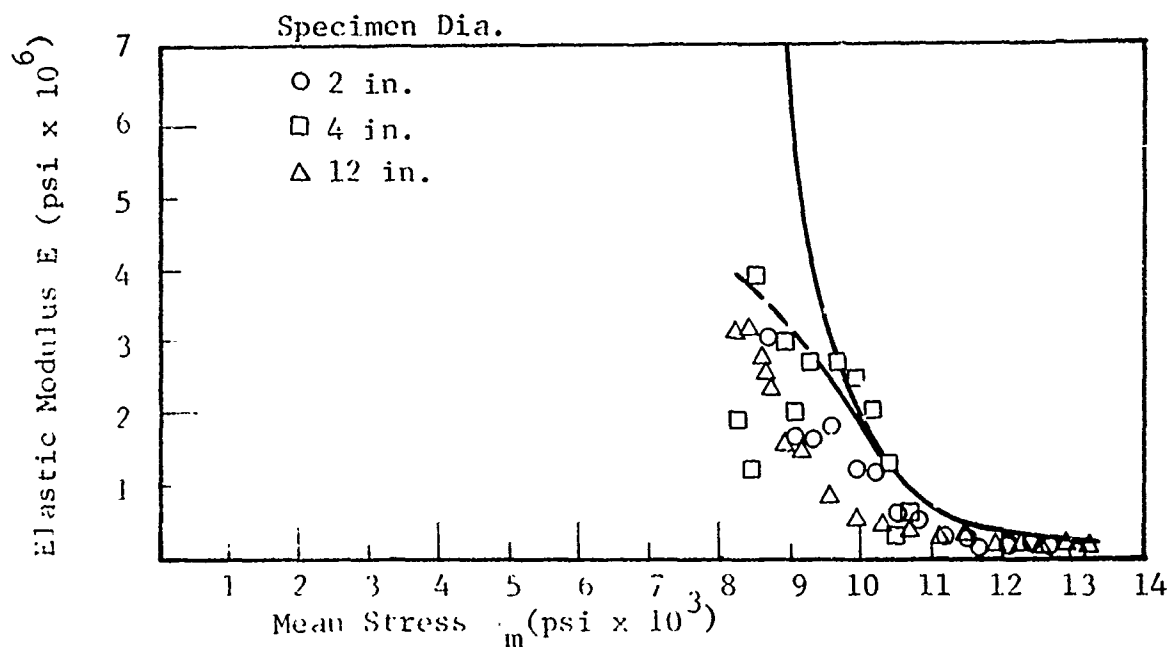


Fig. 48 ELASTIC MODULUS FOR LIMESTONE ( $\sigma_3 = 8$  ksi)

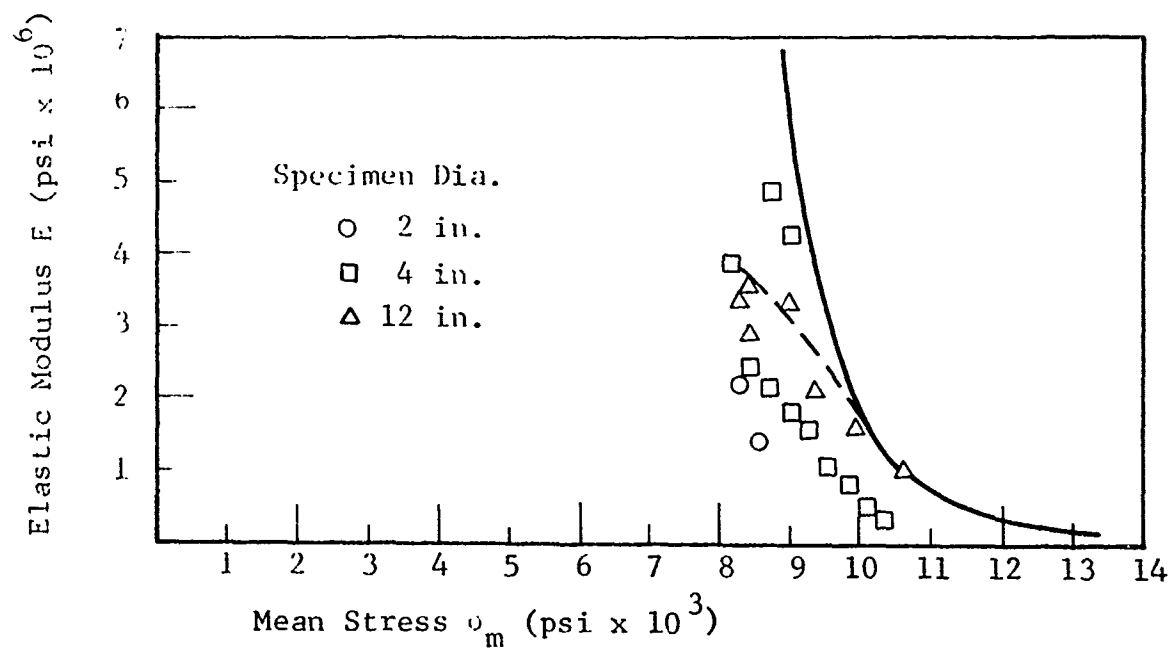


Fig. 49 ELASTIC MODULUS FOR LIMESTONE ( $\sigma_3 = 10$  ksi)

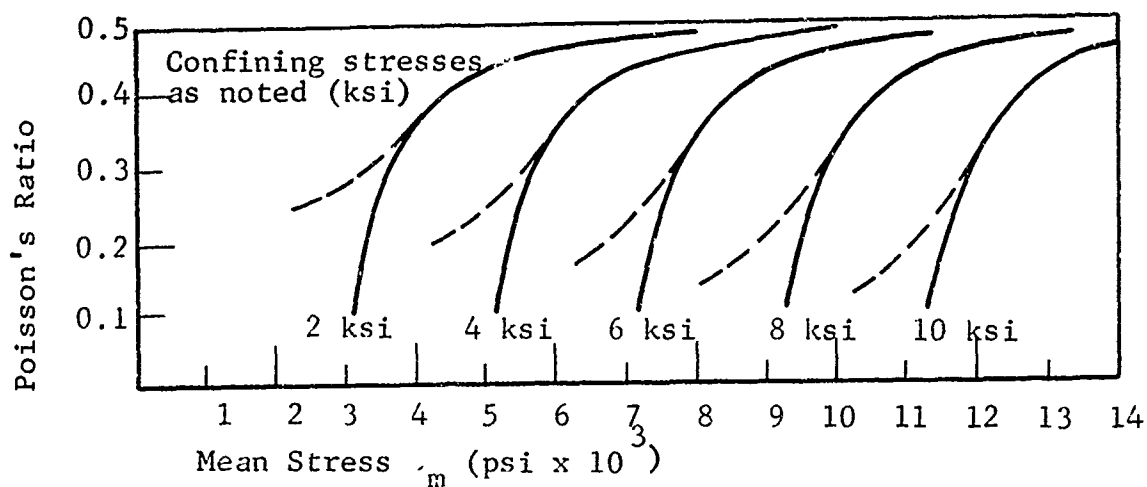


Fig. 50 POISSON'S RATIO MODELS FOR INDIANA LIMESTONE

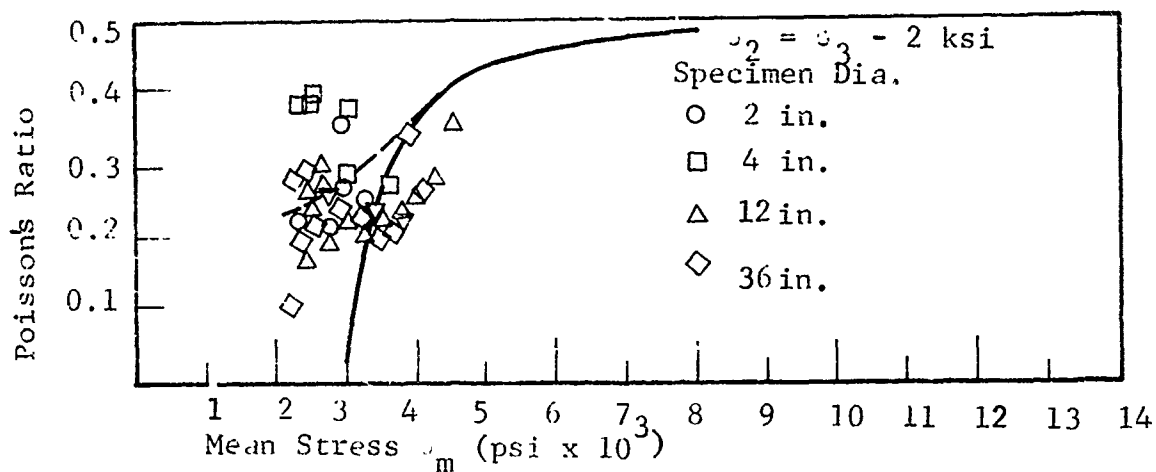


Fig. 51 POISSON'S RATIO FOR INDIANA LIMESTONE ( $\sigma_3 = 2$  ksi)

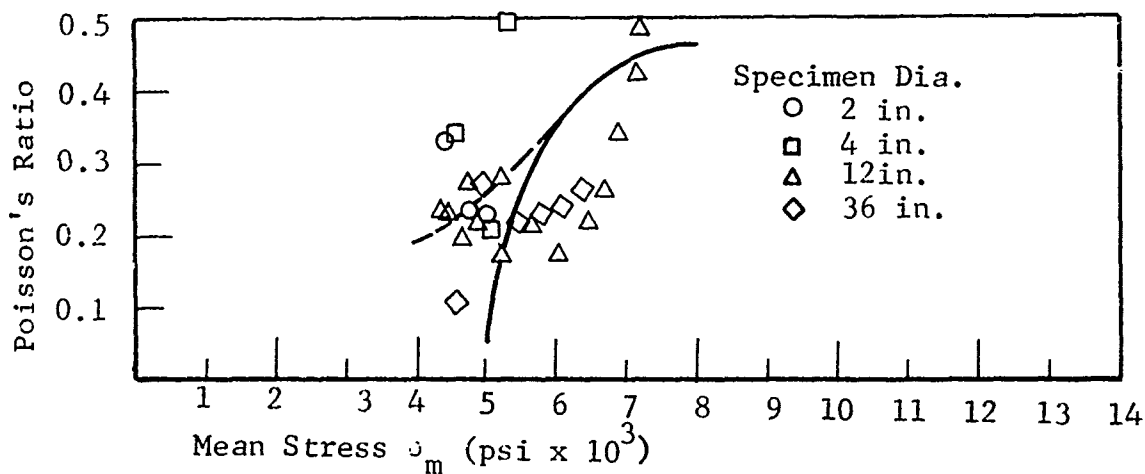


Fig. 52 POISSON'S RATIO FOR INDIANA LIMESTONE ( $\sigma_3 = 4$  ksi)

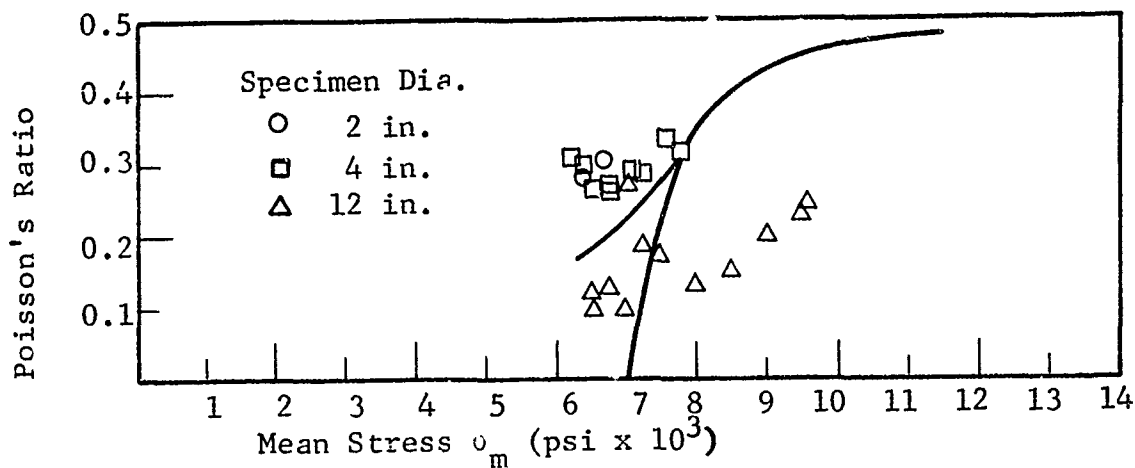


Fig. 53 POISSON'S RATIO FOR INDIANA LIMESTONE ( $\sigma_3 = 6$  ksi)

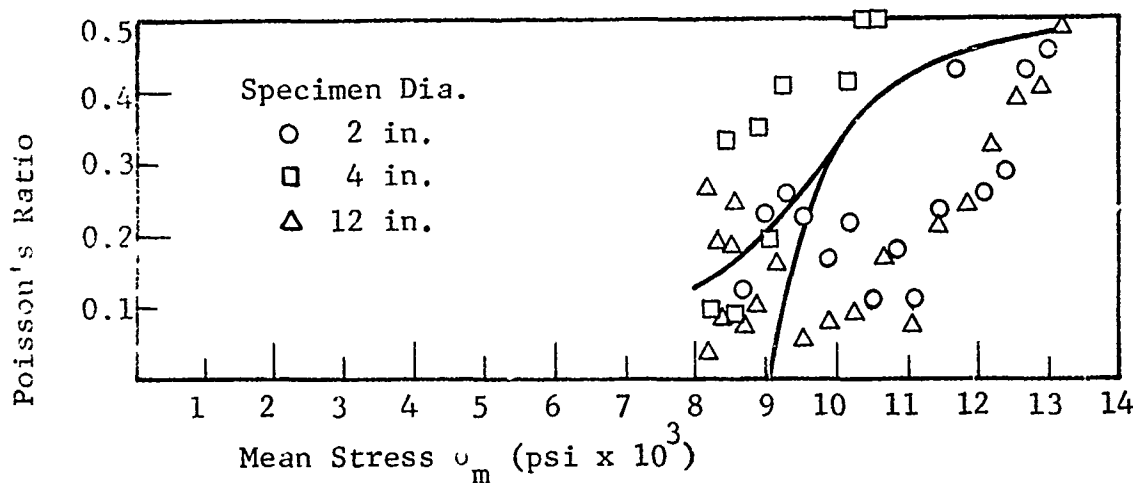


Fig.54 POISSON'S RATIO FOR INDIANA LIMESTONE ( $\sigma_3 = 8$  ksi)

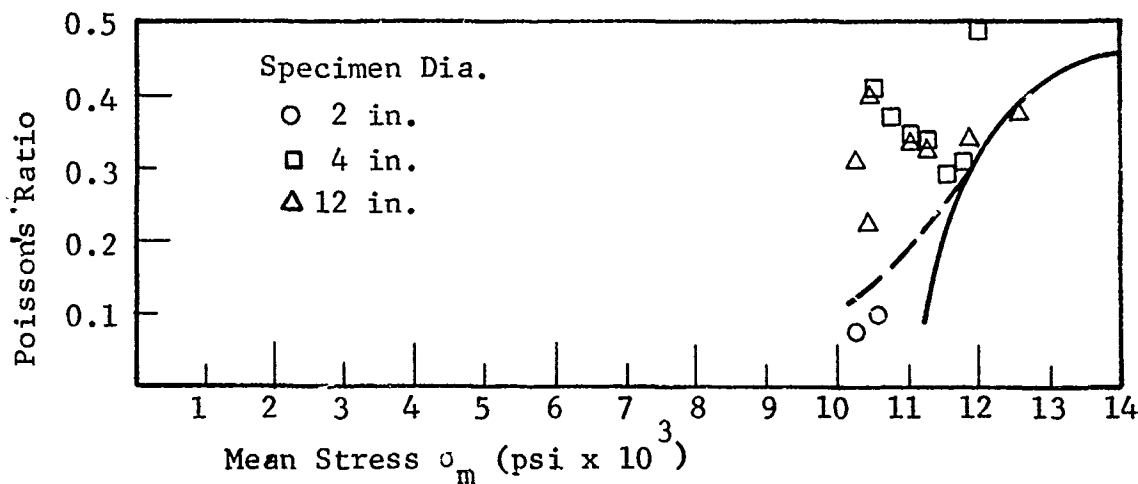


Fig.55 POISSON'S RATIO FOR INDIANA LIMESTONE ( $\sigma_3 = 10$  ksi)



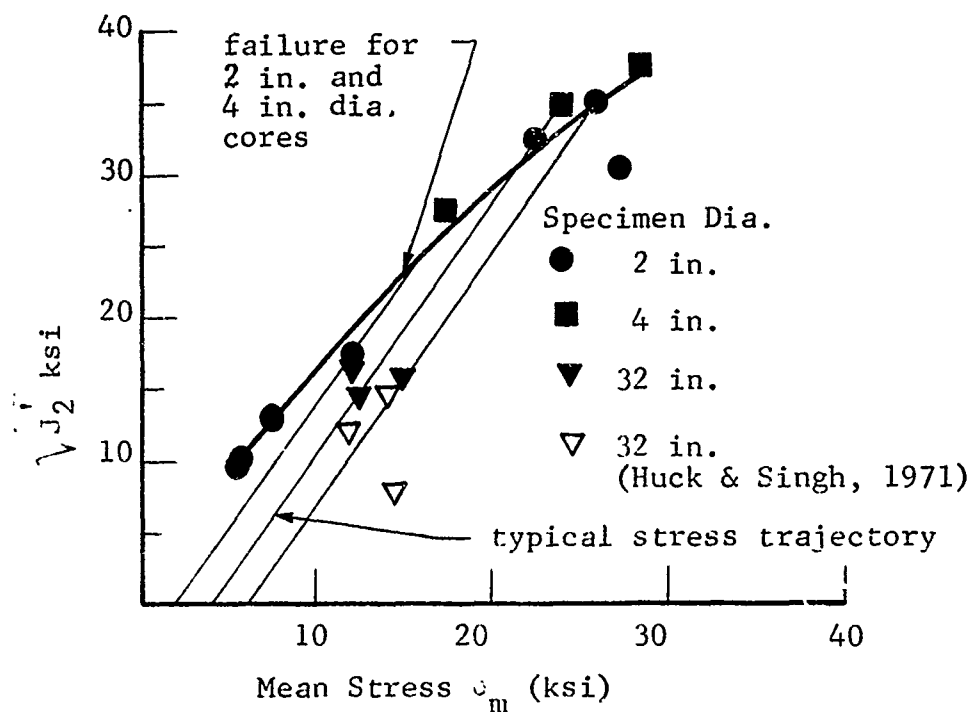


Fig. 56A FAILURE STRESSES FOR CHARCOAL BLACK GRANITE

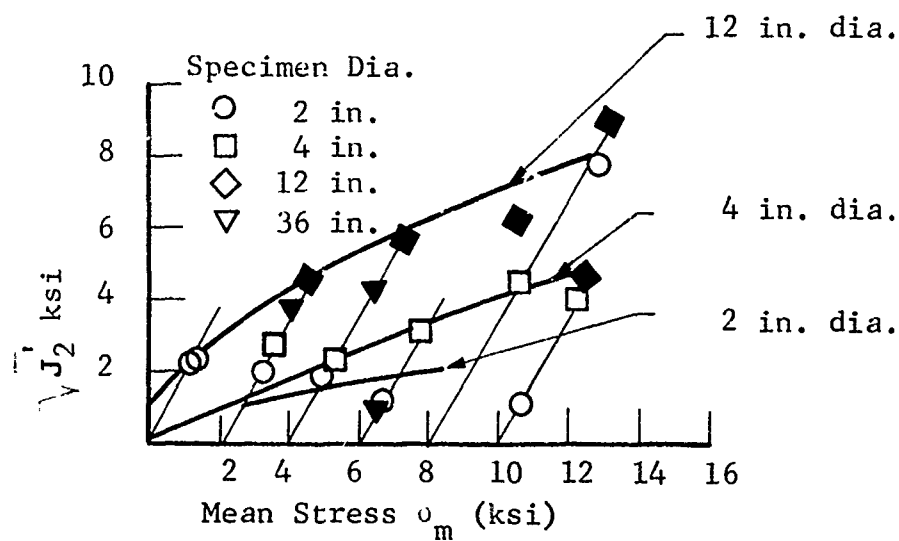


Fig. 56B FAILURE STRESS FOR INDIANA LIMESTONE

No failure curve is defined for the 32-in. dia granite as yet. These cores fail by a series of slippages, displaying ability to carry increased load long after failure begins. In several cases, the 32-in. dia cores survived two complete load-unload cycles, and were found to be fractured only upon removal from the test cell. The highest stress state reached by these cores is shown on Figure 56A, but failure is initiated at some point lower on the stress trajectories. An evaluation of the scale effect can be made by comparing the maximum axial stress attained in the 32-in. dia cores with the axial stress obtained by the intersection of the stress trajectories with the failure curve for small specimens. The following table shows these results.

Table 4 SCALE EFFECT ON FAILURE OF GRANITE

$\sigma_3$	Failure data for 32-in. dia (stress in ksi)		Failure curve small cores (stress in ksi)		Ratio 32-in. $\div$ small cores	
	$\sigma_m$	$\sigma_1$	$\sigma_m$	$\sigma_1$	$\sigma_m$	$\sigma_1$
2	11.9	31.6	15	41	0.79	0.77
4	12.5	29.4	21.5	56.5	0.58	0.52
6	15.0	33.0	26	60	0.57	0.55

It can be seen that the 32-in. dia specimens failed at one-half to three-quarters of the strength attained by the 2-in. and 4-in. dia cores. The stress trajectory for the 2 ksi confining pressure test is nearly parallel to the failure curve, and one of the weaker 2-in. dia specimens failed at nearly the same point as the 32-in. dia core. Tests were conducted on 32 in. dia Charcoal Black granite specimens on a previous program yielding somewhat lower strengths. These data are indicated by open symbols of Figure 56A, and show the amount of scatter observed in the large specimens. None of the 12-in. dia granite cores failed at stress levels possible in that test cell.

#### 4.8.2 Indiana Limestone

The strength of the small Indiana limestone cores ran counter to the expected trend of reduced strength with increased size. Inspection of Figure 56B reveals an apparent loss of cohesive strength in the 2 in. and 4 in. dia cores, as compared with both the 12 in. dia triaxial tests and the 2 in. dia unconfined compression test. This may be caused by distress (disturbance) in the limestone matrix during the hydrostatic loading phase of the triaxial tests. Such an effect would be greater for tests run at higher confining stresses, and smaller for tests run on larger cores, the latter due to arching action in the distressed limestone. That is, particles in the outer layers of the core move into point-to-point contact, so that the distressed region displays no change in frictional strength, only slight volume change and greatly reduced cohesion. In this configuration, a portion of the hydrostatic stress may be carried around the interior of a large core by frictional arching in the outer distressed region, resulting in somewhat reduced stresses and less cohesion loss in the interior. Whether this hypothesis is correct is not known at this time. An alternative cause for this behavior would be the intrusion of liquid and pressure into the pore volume. This is not felt to be the cause, because the trend became noticeable early in the test series, and extreme precautions against liquid intrusion were taken. All cores were given two coats of latex paint by dipping before any triaxial tests were conducted. After the first two triaxial tests on the small rocks were conducted, the remaining eight 2 in. and 4 in. dia cores were given additional coats of latex, so that a heavy layer of water-proof paint was built up on the cores. Secondly, had pressure intruded into the rock, the state of stress would have been radically changed, together with the apparent mechanical response of the rock. However, all sizes of limestone displayed the same moduli and were modeled by the same laws. Hence it

seems that the only influence was an actual loss of cohesive strength, probably due to distress in the limestone matrix near the surface of the specimens.

The 36 in. dia limestone cores failed at stress levels ranging from 85 to 21 percent of the 12 in. dia core strengths, the greater strength reduction occurring at higher stress levels, as was also the case for the charcoal black granite.

## 5.0 CONCLUSIONS

A total of 36 triaxial tests were conducted on Charcoal Black granite and Indiana limestone specimens ranging from 2 in. dia to 36 in. dia. Because of the bulk of data collected, the stress-strain data are presented in terms of descriptive models.

### 5.1 Hydrostatic Behavior

The hydrostatic model for both rock types is the following, previously used by Seaman and Whitman.<sup>32</sup>

$$\sigma_m = A \epsilon_v^n$$

from which

$$k_t = nA^{n-1} \sigma_m^{(n-1)/n}$$

in which

$\sigma_m$  = mean stress

$\epsilon_v$  = volumetric strain

$k_t$  = tangent bulk modulus

A and n model parameters

### 5.2 1. -axial Behavior

The granite was fit to a shear model used by Birch and Bancroft.<sup>33</sup>

$$G_t = c \sigma_m^{0.1}$$

in which

$G_t$  = shear modulus

c = a model parameter

## 5.0 CONCLUSIONS

A total of 36 triaxial tests were conducted on Charcoal Black granite and Indiana limestone specimens ranging from 2 in. dia to 36 in. dia. Because of the bulk of data collected, the stress-strain data are presented in terms of descriptive models.

### 5.1 Hydrostatic Behavior

The hydrostatic model for both rock types is the following, previously used by Seaman and Whitman.<sup>32</sup>

$$\sigma_m = A \epsilon_v^n$$

from which

$$k_t = nA^{n-1} \sigma_m^{(n-1)/n}$$

in which

$\sigma_m$  = mean stress

$\epsilon_v$  = volumetric strain

$k_t$  = tangent bulk modulus

A and n model parameters

### 5.2 Triaxial Behavior

The granite was fit to a shear model used by Birch and Bancroft.<sup>33</sup>

$$G_t = c \sigma_m^{0.1}$$

in which

$G_t$  = shear modulus

c = a model parameter

The limestone behavior was found to be bounded by the following model:

$$G_t = r B^{1/r} (\Delta\sigma)^{(r-1)/r}$$

in which

$G_t$  = shear modulus

$\Delta\sigma$  = deviator stress

B and r model parameters

The parameters for all models are listed in Table 5.

The models were used to compute values for elastic modulus and Poisson's ratio. The agreement with the observed data was good for elastic modulus at stress states below yielding, and only fair for Poisson's ratio.

The only major influence of specimen size on the stress-strain behavior of either rock type occurred in the 12-in. dia granite cores. These cores also displayed significantly higher sonic velocity and Schmidt hammer readings, and the difference in model parameters is considered to be the result of slightly different rock properties rather than the influence of scale.

### 5.3 Effect of Specimen Size on Strength

Sufficient data is not yet available to precisely describe the scale effect on strength, or to evaluate the statistical hypotheses describing scale effect. The 2-in. and 4-in. dia Charcoal Black granite cores appear to share a common failure criteria, while the 32-in. dia granite specimens failed at stress levels only 1/2 to 3/4 of the strengths achieved by the small cores.

The 36-in. dia Indiana limestone cores failed at stress levels of approximately 3/4 those attained by the 12-in. limestone.

TABLE 5

HYDROSTATIC MODEL PARAMETERS

	A	n	model
2 in. and 4 in. dia granite	$2.77 \times 10^8$	1.73	$\sigma_m = A \epsilon_v^n$ $k_t = n A^{n-1} \sigma_m^{(n-1)/n}$
12 in. dia granite	$4.66 \times 10^7$	1.30	
32 in. dia granite	$4.00 \times 10^8$	1.73	
all sizes limestone	$0.490 \times 10^6$	0.75	

## TRIAXIAL MODEL PARAMETERS

	Parameters	Model
2 in. and 4 in. dia granite	$c = 1.89 \times 10^6$	$G_t = c \sigma^{0.1}$ for granite
12 in. dia granite	$c = 1.895 \times 10^6$	
32 in. dia granite	$c = 1.735 \times 10^6$	
all sizes limestone	$r = 0.30$ $B = 3.55 \times 10^4$	$G_t = r B^{r-1} (\Delta \sigma)^{(r-1)/r}$ for limestone



#### 5.4 Effect of Scale on Type of Failure

There was a drastic change in failure with increasing specimen size for both rock types. The 32-in. dia granite and 36-in. dia limestone specimens failed very gradually and displayed increasing load carrying ability long after slippage was initiated. The failure of the small cores was very rapid, with all strength lost immediately upon initiation of failure. If initiation of failure is considered rather than maximum stress attained, the influence of specimen size on strength would be even greater than that presented above.

#### 5.5 Recommendations

Additional data on these and similar rock types should be accumulated. The gradual failure and extended load carrying ability of the larger specimens appears to be similar to failures observed in rock masses. It seems likely that models for large specimens may be developed that will be more effective in predicting mass behavior.

The small scale effect with respect to elastic properties suggests that effort should be diverted from strain gage instrumentation to obtaining additional failure data. The strain gages should probably be replaced with deflection gages operating over the length and diameter of the specimens, at least in the larger sizes. This will give an indication of the gross rock behavior, including slippage.

The sonic velocity mapping was found to be effective in predicting variations in basic properties, the system used being both rapid and accurate. The use of this test should be increased in future programs. The amount of Shore scleroscope testing should probably be reduced sharply, and not used as an indicator of core to core variability.

## REFERENCES

1. Huck, P. J. and Singh, M. M., "Triaxial Tests on Large Rock Specimens" Final Report, contract DASA-01-69-C-0134 for Dept. of Defense, Advanced Research Projects Agency, July 1971.
2. Salamen, M. D. G., and Munro, A. H., "A Study of the Strength of Coal Pillars" J. of the S. Africa Inst. of Mining and Metallurgy, Sept. 1967.
3. Greenwald, H. P., Howath, H. C., and Hartman, I., "Experiments on the Strength of Small Pillars of Coal in the Pittsburgh Bed" U. S. Bureau of Mines Tech. Paper 605, 1939.
4. Steart, F. A., "Strength and Stability of Pillars in Coal Mines" J. Chem. Metall. Min. Soc. S. A. vol 54, 1954.
5. Weibull, W., "A Statistical Theory of Strength of Materials", Ingretensk Akad. Handl., n151, 1939 p. 5-45.
6. Protodyakonov, M. M., "Methods for Evaluating of Cracks and Strength of Rocks in Depth", Fourth Intl. Conf. Rock Mech. and Strata Control, Columbia U., New York, N. Y., 1964, Addendum.
7. Grobbelaar, C., "A Theory for the Strength of Pillars", Pillarco, Pretoria, S. Africa, June 1970, 103p.
8. Epstein, B., "Statistical Aspects of Fracture Problems", Jour. Appl. Phys. v 19, Feb. 1948.
9. Bieniawski, Z. T., "Mechanism of Brittle Fracture of Rock", D.Sc (Eng.) Thesis, U. of Pretoria, S. Africa, 1968.
10. Glucklich, J., Cohen, L. J., "Size as a Factor in the Brittle-Ductile Transition of Some Materials", Int. Jour. of Fract. Mech. Dec. 1967, p. 278-289.
11. Glucklich, J., Cohen, L. J., "Strain-Energy and Size Effects in a Brittle Material", ASTM Materials Research and Standards, v 8, n10, Oct. 1968, p. 17-22.
12. Baecher, G. B., "The Size Effect in Brittle Fracture", M. S. Thesis, Mass. Inst. Tech. June 1970, 190p.
13. Swanson, S. R., "Development of Constitutive Equations for Rocks", Ph.D. Thesis, Univ. of Utah, Dec. 1969, 140p.
14. Adams, F. D. and Nicholson, J. T., "An Experimental Investigation into the Flow of Marble", Phil. Trans. Roy. Soc. (London), Ser. A, v 196, 1901, p. 363-401.

### REFERENCES (Cont'd)

15. von Karman, T., "Festigkeitversuche unter Allseitigem Druck", Zeitschr. des Vereins deut. Ing., v 60, 1911, p. 1749-1757.
16. Griggs, D. T., "Deformation of Rocks Under High Confining Pressures", J. Geol., v. 44, 1936, p. 541-577.
17. Griggs, D. T., and Miller, W. B., "Deformation of Yule Marble: Part I--Compression and Extension Experiments on Dry Yule Marble at 10,000 Atmospheres Confining Pressure, Room Temperature", Geol. Soc. Am. Bul, v. 62, 1951, p. 853-862.
18. Handin, J. W. and Griggs, D., "Deformation of Yule Marble: Part II--Predicted Fabric Changes", Geol. Soc. Am., v. 62, 1951, p. 863-886.
19. Griggs, D. and Handin, J., "Rock Deformation", Geol. Soc. Am., Mem. 79, March 1, 1970, 382p.
20. Baidyuk, B. V., "Mechanical Properties of Rocks at High Temperatures and Pressures", Consultants Bureau, Plenum Pub. Corp. New York, 1967.
21. Morgenstern, N. R. and Tamuly Phukan, A. L., "Non-Linear Stress-Strain Relations for a Homogeneous Sandstone", Intl. Jour. Rock Mech. Mng. Sci., v. 6, 1969, p. 127-142.
22. LaMori, P. N., "Static Determination of the Equation of State of Cedar City Tonalite", DASA Rept. No. 01-69-C 0053, May 1970, 78p.
23. McClintock, F. A., Walsh, J. B., "Friction on Griffith Cracks in Rock under Pressure", Proc. 4th Nat. Cong. Appl. Mech., Berkeley, 1962, p. 1015-1022.
24. Brace, W. F., "Brittle Fracture of Rocks", Proc. Intl. Conf. on State of Stress in the Earth's Crust, American Elsevier Publ. Co., New York, 1964, p. 111-174.
25. Murrell, S. A. F., "The Effect of Triaxial Stress Systems on the Strength of Rocks at Atmospheric Temperatures", Geophys. Jour., v. 10, 1965, p. 231-282.
26. Pfefferle, W. and Smith, C. R., "Phase I Flatjack Tests", Air Force Rept. No. SAMS0-TR-70-381, Oct. 6, 1970, 42p.
27. Obert, L., Personal communication.
28. Hoek, E., "Brittle Failure of Rock", Chapter 4 in Rock Mechanics in Engineering Practice (ed. Stagg and Zienkiewicz), J. Wiley, London, 1968, p. 99-124.

#### REFERENCES (Cont'd)

29. Wawersik, W. R., "Detailed Analysis of Rock Failure in Laboratory Compression Tests", Ph.D. Thesis, University of Minnesota, 1968.
30. Cook, N. G. W., "The Failure of Rock", Int. Jour. Rock Mech. Mng. Sci., v. 2, 1965, p. 389-403.
31. Houpert, R., "La résistance à la rupture des granites", Revue de l'industrie minière, May 15, 1963, p. 21-23.
32. Seaman, L., and Whitman, R. V., "Stress Propagation in Soils", Final Report -Part IV, Stanford Research Institute, Menlo Park, California, for Defense Atomic Support Agency, DASA 1266-4, June 1964.
33. Birch, F., and Bancroft, D., "The Effect of Pressure on the Rigidity of Rocks-I", Jour. Geol. v. 46, Jan-Dec 1938.

## APPENDIX

### PLOTTED TEST DATA

This appendix presents the stress-strain data for the individual triaxial tests. The plots included are deviator stress as a function of shear strain and mean stress as a function of volumetric strain. The tests are arranged by rock type, core diameter and confining stress in that order. Pertinent test data is specified on each plot.

